Wesleyan University Physics Department

Particle-Turbulence Interactions

by

Bardia Hejazi

Faculty Advisor: Professor Greg A. Voth

A Dissertation submitted to the faculty of Wesleyan University
in partial fulfillment of the requirements for the
Degree of Doctor of Philosophy in Physics

Middletown, Connecticut January, 2021

Abstract

In this work we examine how particle dynamics and orientation patterns can reveal information about fluid structures, how particles can be used as a device to measure fluid statistics, and how in return, fluid structures interact and influence the dynamics of particles. We begin by studying the spatial field of orientations of slender fibers that are advected by a two-dimensional (2D) fluid flow. We introduce emergent scar lines as the dominant coherent structures in the orientation field of passive directors in chaotic flows. We use the standard map as a simple time-periodic two-dimensional flow that produces Lagrangian chaos. This class of flows produces persistent patterns in passive scalar advection, and we find that a different kind of persistent pattern develops in the passive director orientation field. We identify the mechanism by which emergent scar lines grow to dominate these patterns at long times in complex flows. Emergent scar lines form where the recent stretching of the fluid element is perpendicular to earlier stretching. Thus these scar lines can be labeled by their age, defined as the time since their stretching reached a maximum.

We next examine how the deformation of particles made of several slender arms in a 2D linear shear and a three-dimensional (3D) turbulent flow allow us to extract the velocity gradient tensor of the flow. Deformation measurements of a particle free to rotate about a fixed axis in a 2D simple shear flow are used to validate our model relating particle deformations to the fluid strain. We then examine deformable particles in a 3D turbulent flow created by a jet array in a vertical water tunnel. Particle positions and orientations are measured with high precision using four high speed cameras and have an uncertainty on the order of 10^{-4} radians in particle orientation measurements. Measured deformations in 3D turbulence are small and only slightly larger than our ori-

entation measurement uncertainty. Deformable particles offer a promising method for measuring the full local velocity gradient tensor from measurements of a single particle where traditionally a high concentration of tracer particles would be required.

With our capabilities in obtaining particle positions and orientations with high precision we expand upon existing work and study the angular dynamics of large isotropic and anisotropic shaped particles in turbulence and demonstrate capabilities in measuring the various quantities involved in particle dynamics. We examine the shape dependence of particle dynamics in turbulence by looking at large disk-like triads that are made of three slender arms separated by 120 degrees and large spherical tetrads that are made of four slender arms separated by the tetrahedral angle. We see that large particles in turbulence behave differently from the expected tracer spheroids in turbulence result. Furthermore, we take a detailed look into particle alignment with the angular velocity, angular acceleration, and translational acceleration under various conditions such as extreme rotational power events.

Contents

1 Introduction 1

1.1 Equations of motion and turbulence 3

1.2 Particle-turbulence interactions 6

1.2.1 Particle advection 6

1.2.2 Particle deformation 9

2 Emergent scar lines in chaotic advection of passive directors 12

2.1 Introduction 12

2.2 Phenomenology of passive director orientation in the standard map . . . 16

2.3 Topological singularities in passive director orientation fields 23

2.4 Scar lines in passive director orientation fields 27

2.4.1 Type 1 scar lines 28

2.4.2 Emergent scar lines 31

2.4.3 Age of emergent scar lines 33

2.5 Conclusions 35

2.6 Acknowledgments 37

2.7 Appendix 37

3 Using deformable particles for single particle measurements of velocity gradient tensors 41
3.1 Introduction 41
3.2 Theory 46
    3.2.1 Model of arm deformations due to viscous flow 46
    3.2.2 Extracting the strain rate from arm deformations 47
3.3 2D experiments 49
    3.3.1 2D experimental setup 49
    3.3.2 2D results 53
3.4 3D experiments 59
    3.4.1 3D experimental setup 59
    3.4.2 3D results 61
3.5 Conclusions 69
3.6 Appendix 69
3.7 Further experiments in 3D turbulence 70
    3.7.1 Taylor-Couette experiments 70
    3.7.2 Water tunnel experiments 76

4 Angular dynamics of large particles in turbulence 82
4.1 Introduction 82
4.2 Experimental setup 85
4.3 Results and discussion 88
    4.3.1 Particle velocities and accelerations 88
    4.3.2 Particle alignments 96
    4.3.3 Translational and rotational power 103
4.4 Conclusions 104

5 Appendix 107

5.1 Data documentation 107

5.2 Server system documentation 108

5.3 Data analysis 108

List of Figures

1.1 Mean square rotation rate of tracer particles 8

2.1 Poincaré section of the standard map 16
2.2 Orientation field of advected directors and eigenvectors of the Cauchy-Green strain tensor 17
2.3 Gradient of the angle of the fiber orientation field 20
2.4 Types of singularities 22
2.5 Evolution of the orientation and stretching fields with time 23
2.6 Number of singularities as a function of time 27
2.7 Orientation fields at the long-time limit 28
2.8 Locations of type 1 scar lines 29
2.9 Sensitivity of the advected directors and type 1 scar lines to initial orientation 30
2.10 Locations of emergent scar lines 32
2.11 Simple schematic flow that generates singularities and emergent scar lines 39
2.12 Quantifying the age of emergent scar lines 40

3.1 Schematic of an arm deformation 48
3.2 The deformable triads used in our experiments 50
3.3 Experimental apparatus for the 2D simple shear flow experiments . . . 51
3.4 Image of a triad in the 2D simple shear flow 52
3.5 The rotation rate and deformation of a triad particle in 2D simple shear flow as a function of fluid strain rate 54
3.6 Angle between every two neighboring arms as a function of time 55
3.7 The measured angle between a given arm and the arm immediately trailing it as a function of the trailing arms location 56
3.8 Angle between arms 2 and 1 as a function of time, model and experiments 58
3.9 Magnitude of the fluid strain and the orientation of the extensional eigenvector of the fluid strain 60
3.10 The Euler angles giving the particle orientation as a function of time . . 62
3.11 Image of a particle in a single frame and the modeled particle fitted to the image at the same instance of time 64
3.12 Measured deformations for the three arms of a triad as a function of time 66
3.13 Measured deformations for the three arms of a simulated triad in turbulent flow 68
3.14 Schematic of the conical Taylor-Couette apparatus 71
3.15 Deformable tetrad used in our experiments 73
3.16 Velocity profile of the Taylor-Couette flow 73
3.17 Tracer particle trajectory in Taylor-Couette flow 74
3.18 Camera view of the Taylor-Couette apparatus 75
3.19 Energy dissipation calculation from second and third order structure functions 77
3.20 Second order longitudinal structure function compared to the theoretical value for the inertial subrange 78

3.21 Fitting tetrad model to camera images 79
3.22 Measured deformations for a deformable tetrad 81

4.1 Particles used in the experiments 87
4.2 Mean square particle rotation rates as a function of fit-time 89
4.3 Mean square particle accelerations as a function of fit-time 90
4.4 Particle tumbling and rotation rate ratios 92
4.5 Auto-correlations of the various quantities involved in particle dynamics 95
4.6 Filters on the particle orientation fit quality used to obtain the solid-body rotation rate of a triad 97
4.7 Filters on the particle translational fit quality used to obtain the translational velocity and acceleration of a triad 98
4.8 PDF of the cosine of the angle between the vectors involved in particle dynamics 99
4.9 Cosine of the angle between **p** and $\boldsymbol{\Omega}$, **p** and $\boldsymbol{\alpha}$ for a triad 100
4.10 Cosine of the angle between **a** and $\boldsymbol{\Omega}$ for a triad and tetrad 102
4.11 PDFs of the translational and rotational power of triads and tetrads in the turbulent water tunnel 103
4.12 PDF of the translational power of tracers in the turbulent water tunnel . 105

Chapter 1

Introduction

The dynamics and deformations of complex shaped particles in fluid flows are of importance in many different aspects of life and scientific research. The dynamics and orientation of fibers and rod-shaped particles are relevant to environmental flows such as cloud physics (Pinsky and Khain, 1998; Saunders, 1994; Saunders et al., 2001; Sherwood et al., 2006) and industrial flows from paper manufacturing (Lundell et al., 2011; Olson and Kerekes, 1998) to drag reduction using fiber suspensions (Dimitropoulos et al., 2005; Paschkewitz et al., 2005). In addition to advection and particle orientation, particle deformations are also an important factor in real-life particle-flow interactions and play a key role in many different flow environments (Ezzeldin et al., 2015; Guo et al., 2017; Marchioli and Vincent, 2019; Stockie and Green, 1998). Recent advances in experimental techniques and computational capabilities have allowed us to study the advection (Voth and Soldati, 2017) and deformation (Allende et al., 2018; Dotto and Marchioli, 2019; Gay et al., 2018; Rosti et al., 2018) of particles in fluid flows which have led to a deeper understanding of particle-turbulence interactions.

We expand upon existing work in the field of particle-turbulence interactions and study the alignment and deformation dynamics of complex shaped particles in different flows. We first begin by examining the orientation field of passive directors (fibers) as they are advected in a 2D chaotic flow. We see that the orientation field of the advected directors approaches a persistent pattern similar to those observed in passive scalar advection (Pierrehumbert, 1994; Rothstein et al., 1999). Another similarity is that lines of large gradient in the orientation form each period and are stretched until they become extremely thin, similar to striations that form in the passive scalar field. We identify the key structures in the fiber orientation field in 2D chaotic flows and the mechanism by which they form and how they develop in time.

We also study particle deformation in different turbulent flows as a new measurement technique to obtain the full velocity gradient tensor of the flow by imaging a single particle trajectory. The advantage of using deformable particles is the ability to use a single particle to obtain the same information that traditionally would require a high number of tracer particles. We demonstrate the feasibility of such measurements and the state of the art in precision particle tracking. With our capabilities of performing highly precise measurements of particle positions and orientations we next study the translational and angular dynamics of different shaped particles as they are advected in turbulent flow. We study the alignment of the translational and angular vectors involved in particle dynamics with respect to one-another and what those quantities can reveal of the spatial structure of the flow.

For the remainder of this chapter we will briefly introduce the equations of motion for fluids and how we can begin to study particle-turbulence interactions. We will discuss particle alignments and the tools that we can use to better understand such dynamics and what quantities of the flow are measurable using particle suspensions.

1.1 Equations of motion and turbulence

Fluids are treated as a continuous media where we can look at fluid elementas and not at the discrete fluid molecules and obtain continuous fields, such as the density field $\rho(\mathbf{x}, t)$ and the velocity field $\mathbf{U}(\mathbf{x}, t)$. Using the mass conservation or continuity equation and conservation of momentum we can arrive at the equations of motion for a fluid element. This equation is know as the Navier-Stokes equation,

$$\frac{\partial \mathbf{U}}{\partial t} + (\mathbf{U} \cdot \nabla)\mathbf{U} = -\frac{1}{\rho}\nabla P + \frac{\mu}{\rho}\nabla^2\mathbf{U} + \mathbf{g}, \tag{1.1}$$

where we also assume constant-density flows which leads to the condition that the velcity field be divergence free, $\nabla \cdot \mathbf{U} = 0$. Here ρ is the density of the fluid, P is the pressure field, μ the dynamic viscosity of the fluid, and $\mathbf{g}$ the external body forces acting on the fluid due to gravity.

The characteristic length scale L determined by the largest scales of the flow and the characteristic velocity scale U dependent on the initial and boundary conditions are used to define the non-dimensional independent variables

$$\hat{\mathbf{x}} = \frac{\mathbf{x}}{L}, \quad \hat{t} = t\frac{U}{L}, \tag{1.2}$$

and dependent variables

$$\hat{\mathbf{U}}(\hat{\mathbf{x}}, \hat{t}) = \frac{\mathbf{U}(\mathbf{x}, t)}{U}, \quad \hat{p}(\hat{\mathbf{x}}, t) = \frac{p(\mathbf{x}, t)}{\rho U^2}. \tag{1.3}$$

Applying these transformations to the Navier-Stokes equations lead to a non-dimensionalized equation

$$\frac{\partial \hat{U}_j}{\partial \hat{t}} + \hat{U}_i \frac{\partial \hat{U}_j}{\partial \hat{x}_i} = \frac{1}{Re} \frac{\partial^2 \hat{U}_j}{\partial \hat{x}_i \partial \hat{x}_i} - \frac{\partial \hat{p}}{\partial \hat{x}_j}, \tag{1.4}$$

where we have switched to tensor notation and summation is implied. The Reynolds number is defined as

$$Re \equiv \frac{UL}{\nu}, \tag{1.5}$$

with $\nu = \mu/\rho$ being the kinematic viscosity of the fluid. The Reynolds number is the only parameter appearing in these equations and its value can be seen as the ratio of the inertial forces of the fluid to the viscous forces, where low *Re* corresponds to a flow in which the viscous forces are the dominant forces and high values of *Re* correspond to turbulent flows with large inertial forces where viscous effects become negligible.

For a fully turbulent flow at high Reynolds number, turbulence is composed of many eddies with different length scales. The large scale eddies are unstable and as a result break up and transfer their energy to the smaller scale eddies. The transfer of energy continues until the energy is dissipated to the molecular viscosity. This phenomena is known as the energy cascade where the dissipation rate ε is the rate of which energy is transferred from the large scales to the small scales. According to Kolmogorov's first similarity hypothesis, in every turbulent flow at large Reynolds numbers, the statistics of the small-scales have a universal form that are uniquely determined by ε and ν. The Kolmogorov scales characterize the smallest, dissipative eddies and are

$$\eta \equiv (\nu^3/\varepsilon)^{1/4} \tag{1.6}$$

$$u_\eta \equiv (\varepsilon\nu)^{1/4} \tag{1.7}$$

$$\tau_\eta \equiv (\nu/\varepsilon)^{1/2} \tag{1.8}$$

Kolmogorov's second similarity hypothesis states that in every turbulent flow at sufficiently large Reynolds numbers, in the inertial subrange $\eta \ll r \ll L$, where L is the energy containing range and η is the Kolmogorov length defining the dissipative range, the statistics of the of the motions of scale r have a universal form that is uniquely determined by ε, independent of ν. In the inertial subrange, we can experimentally measure ε using the moments of the velocity structure function $D_n(r)$ which only depends on ε and r

$$D_n(r) = C_n(\varepsilon r)^{n/3}, \tag{1.9}$$

where C_n are constants. In our experiments we use the second and third moments of the velocity structure function to measure ε. The constant for the second moment is found empirically to be $C_2 = 2.0$, and the constant for the third moment is derived analytically from the Navier-Stokes equations and leads to the Kolmogorov 4/5 law where $C_3 = -4/5$. At higher moments the measured exponents of Eq. 1.9 start to deviate from the Kolmogorov predictions. In our work we also use ε to determine $\mathbf{S}$, the strain component of the velocity gradient tensor, from $\varepsilon = 2\nu\left\langle S_{ij}S_{ij}\right\rangle$. The velocity gradient tensor is comprised of a symmetric part, the rate-of-strain tensor $S_{ij} \equiv 1/2(\partial U_i/\partial x_j + \partial U_j/\partial x_i)$, and antisymmentric part, the rate-of-rotation tensor $W_{ij} \equiv 1/2(\partial U_i/\partial x_j - \partial U_j/\partial x_i)$.

1.2 Particle-turbulence interactions

Particle dynamics and transport in fluid flows has a long history of study with important implications in many different areas. When particles are neutrally buoyant and small enough that they are comparable to the smallest length scales of the flow then they can behave like Lagrangian tracer particles and are advected by the local fluid velocities. Such particles can provide us with information and insight to the structures of the flow itself and how the flow develops with time. However, when particles are larger than the Kolmogorov length scale they mostly experience flow structures and velocity gradients that are on the same scale as the particle size. These larger particles are still of great interest in many different flows such as applications in the paper manufacturing and textile industries (Guo et al., 2017; Lundell et al., 2011; Olson and Kerekes, 1998). Studying flexible particles in fluid flows can further develop our understanding of particle-turbulence interactions and be used in new ways to probe turbulent flows and measure fluid velocity gradients.

1.2.1 Particle advection

The advection of passive scalars in turbulence has proven to be a rich area for scientific study (Aref et al., 2017; Ottino, 1990; Warhaft, 2000). Early work on passive scalars considered primarily integrable flows and statistical work on turbulent flows (Monin and Yaglom, 1975). Then it was identified that flows with chaotic particle trajectories formed an intermediate case (Aref, 1984). A wide variety of mathematical tools have been developed for analyzing passive scalar advection (Aref et al., 2017) and insights from dynamical systems allowed the identification of the coherent structures that are key to understanding the spatial fields of passive scalars in chaotic 2D flows (Ottino, 1990). Eventually methods were developed for identifying similar structures in turbulent cases (Haller, 2015).

In addition to particle transport we would also like to examine particle orientations and alignment. The orientational degree of freedom introduces physics that is not present in the passive scalar problem. For example, a flow produces non-trivial patterns in the orientation field of fibers even for homogenous initial conditions leading to an entirely different class of problems (Szeri et al., 1991). The dynamics of fibers in fluid flows has been the focus of extensive study (Guazzelli and Hinch, 2011; Voth and Soldati, 2017), often motivated by complex cases in applications of dense fiber suspensions. For example, fiber suspensions are used for drag reduction, and the fiber stress is determined by the spatial structure of the preferential fiber orientation (Paschkewitz et al., 2005). Another example comes from instabilities of the fiber orientation field that are responsible for the different sedimentation properties of fiber suspensions compared with suspensions of spheres (Herzhaft et al., 1996; Koch and Shaqfeh, 1989). But despite progress on these complex problems, we still do not have a clear phenomenology of the fiber orientation field in chaotic and turbulent flows.

Research on more complex shaped and anisotropic particles has a long history (Voth and Soldati, 2017). Jeffery (1922) studied the dynamics of small axisymmetric ellipsoidal particles in a simple viscous fluid flow and determined that the rotation rate of these particles is determined by the fluid velocity gradients.

$$\dot{p}_i = W_{ij}p_j + \frac{\lambda^2 - 1}{\lambda^2 + 1}\left(S_{ij}p_j - p_i p_k S_{kl} p_l\right), \tag{1.10}$$

where $\mathbf{p}$ is the unit vector along the symmetry axis of the particle and $\lambda = l/d$ is the aspect ratio of the particle, defined as the ratio of the length along the symmetry axis of the ellipsoid to its diameter. Further studies have examined axisymmetric particles and measured their solid-body rotation rate $\mathbf{\Omega}$ in different types of flows. The solid-body rotation rate can can be split into a tumbling rate, $\dot{\mathbf{p}} = \mathbf{\Omega} \times \mathbf{p}$, and spinning rate, $\Omega_p = \mathbf{\Omega} \cdot \mathbf{p}$. For axisymmetric tracer particles, the tumbling rate is given by eq. 1.10 and the spinning rate is equal to half the vorticity component along the particle symmetry axis. Fig. 1.1 in Voth and Soldati (2017) shows the mean square value of these quantities for tracer particles as a function of particle aspect ratio in homogeneous isotropic turbulence.

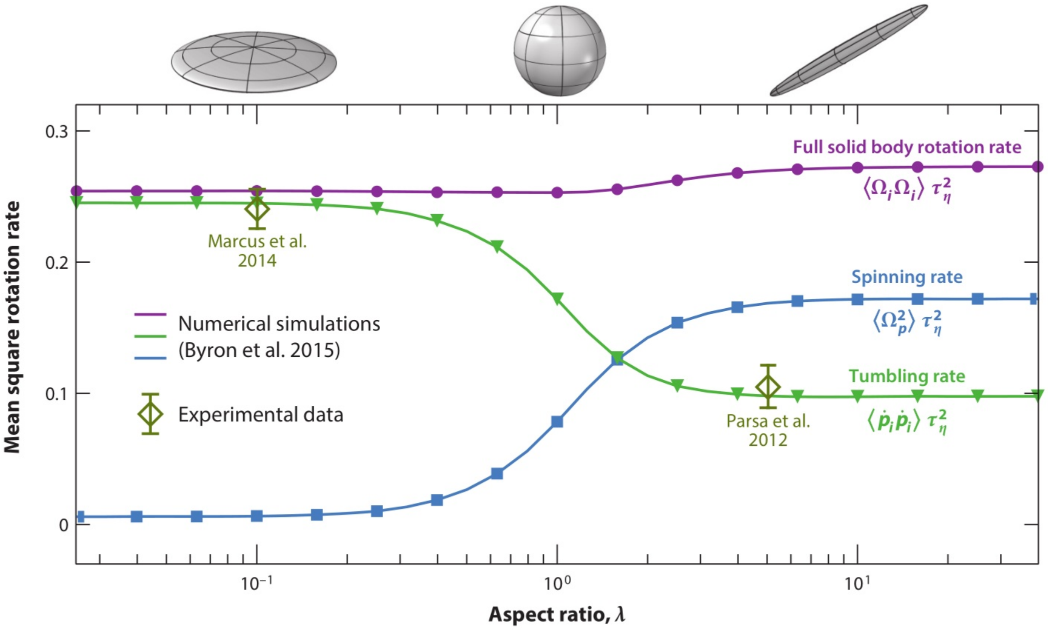

Figure 1.1: Mean square rotation rates of tracer particles as a function of aspect ration in homogeneous isotropic turbulence, figure is from Voth and Soldati (2017).

Since particle rotation rates are dependent on the components of the velocity gradient tensor then we can expect that the orientation and alignment of these particles are also dependent on the velocity gradient tensor. The Cauchy-Green strain tensors are a useful tool for examining particle orientations and their alignments with respect to the stretching a fluid element experiences. The Cauchy-Green strain tensors have previously been a useful way to study the Lagrangian coherent structures that develop in fluid flows (Haller, 2015; Voth et al., 2002a) and are related to the finite time Lyapunov exponents which quantify the stretching experienced by each infinitesimal fluid element. The Cauchy-Green strain tensors are calculated using the deformation gradient tensor defined as $F_{ij} = \partial X_i / \partial x_j$, where $\mathbf{x}$ is the position of a fluid element at time t_0 and $\mathbf{X}$ is the position of the fluid element at a later time t. The left and right Cauchy-Green strain tensors are then calculated as

$$\mathbf{C}^{(L)} = \mathbf{F}\mathbf{F}^T, \tag{1.11}$$

$$\mathbf{C}^{(R)} = \mathbf{F}^T\mathbf{F}. \tag{1.12}$$

The two tensors $\mathbf{C}^{(L)}$ and $\mathbf{C}^{(R)}$ have the same eigenvalues but different eigenvectors. The eigenvalues represent the stretching that a fluid element has experienced where the largest eigenvalue shows extension, the smallest eigenvalue compression and the intermediate eigenvalue can be either of the two. The eigenvectors of $\mathbf{C}^{(L)}$ indicate the final direction of a fluid element after stretching where for example, a fiber would tend to align with the eigenvector that corresponds to the maximum eigenvalue indicating that fibers preferentially align with the fluid stretching (Ni et al., 2014; Parsa et al., 2011). On the other hand, the eigenvectors of $\mathbf{C}^{(R)}$ correspond to the fluid element before being stretched and so material lines initially aligned with an eigenvector of $\mathbf{C}^{(R)}$ will align with the corresponding eigenvector of $\mathbf{C}^{(L)}$ after time t.

1.2.2 Particle deformation

In many different flow environments involving particle-turbulence interactions it is also important to study particle deformations due to fluid forces. Deformations of flexible structures by fluid flows play a central role in many environmental flows involving micro-organisms (Qian et al., 2008), biological systems such as studying hemolysis (Ezzeldin et al., 2015), and industrial situations like paper manufacturing and drag reduction (Alben et al., 2002; Guo et al., 2017; Stockie and Green, 1998). Recent technological developments have allowed us to measure and simulate the rotations (Voth and Soldati, 2017) and deformations (Allende et al., 2018; Dotto and Marchioli, 2019; Gay et al., 2018; Rosti et al., 2018) of small particles advected in turbulent flows and have provided us with new insights about particle-turbulence interactions and turbulence structure.

Research on deformable particles in turbulence have primarily focused on flexible fibers, since slender fibers are easily deformable and a simple shape which is easy to fabricate. There is a wide range of work done on the study of small fibers in viscous flows and their dynamics and buckling instabilities (Chakrabarti et al., 2020; du Roure et al., 2019). There is also recent work done on the dynamics of long fibers in turbulence both experimentally and computationally (Ali et al., 2016; Gay et al., 2018; Rosti et al., 2018). However, fiber deformations are a special case that are somewhat more complex than the deformation of other shaped particles. A flow with a uniform velocity gradient cannot easily bend short fibers and they deform if there is a compressive stress that exceeds the buckling threshold. Below this threshold, deformation of fibers is a result of curvature of the velocity field. Brouzet et al. (2014) experimentally measured deformations of long fibers in turbulence, since in practice it is quite difficult to obtain particles flexible enough and viscous stresses large enough to observe buckling of fibers in turbulence when the fiber length is small enough to experience uniform velocity gradients.

Although our understanding of flexible particle dynamics in fluid flows has increased, we still lack a clear quantification of what features of the flow can be measured from particle deformations. The study of the dynamics of flexible particles in fluid flows is an active field of research which has recently seen interest due to the advancement of measurement techniques capable of quantifying particle deformations. We attempt to fill this gap by showing that particles made of slender arms with weak links near the junction are promising tools for measuring the full velocity gradient tensor in incompressible flows. Furthermore, we have significantly improved upon existing experimental techniques allowing us to measure particle orientations and positions with a high level of precision. Even though our measurement precision has increased, we are still on the edge of being able to detect the extremely small deformations experienced by particles in turbulence.

These high precision measurements also allow us to measure particle translational and angular velocities and accelerations. We can study these vectors and their alignment with each other and various other quantities involved in particle-turbulence interactions as a way to better understand fluid spatial structures and how they affect particle dynamics. The majority of work done on particle dynamics in fluid flows concern the transport and rotations of small tracer particles. Recent studies have investigated large-particle dynamics such as the rotations of long fibers (Parsa and Voth, 2014) and show that the fiber rotation rate scales proportionally to the fiber length. Additionally, work on the dynamics of large inertial particles with aspect ratio close to 1 has shown that the rotation rate of these particles seem to scale with the equivalent diameter of an equal volume sphere (Bordoloi and Variano, 2017; Pujara et al., 2018). We expand upon this work by studying the dynamics of large disk-like and spherical particles in turbulence. We observe interesting dynamics and measure solid-body rotation rates that are different from what we would expect from similarly shaped tracer particles in turbulence, shown in Fig. 1.1 (Voth and Soldati, 2017).

Chapter 2

Emergent scar lines in chaotic advection of passive directors

The following chapter is a manuscript that has been published in *Physical Review Fluids* (Hejazi et al., 2017). In this chapter we examine the orientation field of passive directors in a 2D chaotic flow and show that the dominant features in the orientation fields are lines across which the orientation of the passive directors changes rapidly. We also show the process in which these structures are formed and how they are dependent on the flow history.

2.1 Introduction

When slender fibers are advected in a fluid flow, they become aligned by the flow (Guazzelli and Hinch, 2011; Ni et al., 2014; Parsa et al., 2011, 2012; Szeri et al., 1991; Voth and Soldati, 2017; Wilkinson et al., 2009) which produces dramatic effects including changes in material properties such as fluid rheology and scattering of electromagnetic waves. These effects of fiber alignment appear in many applications including design of fiber suspension flows for the paper industry (Lundell et al., 2011; Olson and Kerekes, 1998), prediction of the albedo of icy clouds (Pinsky and Khain, 1998; Saunders, 1994; Saunders et al., 2001; Sherwood et al., 2006), and controlling turbulent drag by adding fibers (Dimitropoulos et al., 2005; Paschkewitz et al., 2005). Other applications include liquid crystals (de Gennes and Prost, 1995) and active nematics (Giomi, 2015; Keber et al., 2014).

The motion and alignment of small, slender fibers in fluid flow has many similarities to the advection of passive scalars such as the concentration of a dye. This passive scalar problem has proven to be a rich area for scientific study (Aref et al., 2017; Ottino, 1990; Warhaft, 2000). For passive scalars, the case of time periodic two-dimensional flows has been a source of many insights since it is the simplest case that produces Lagrangian chaos (Aref, 1984). A wide variety of mathematical tools have been developed for analyzing passive scalar advection (Aref et al., 2017). Particularly relevant to fiber flows is analysis using finite time Lyapunov exponents (which quantify the stretching experienced by each infinitesimal fluid element) that has allowed insights from simple two-dimensional (2D) time-periodic flows to be extended to identification of Lagrangian coherent structures in complex flows (Haller, 2015).

The advection of small slender rigid fibers in fluid flow can be called the passive director problem. Symmetric fibers are described by directors rather than vectors because the two anti-parallel orientations of the particle are equivalent. The orientational degree of freedom of the director introduces physics that is not present in the passive scalar problem. For passive directors, a flow produces non-trivial patterns in the orientation field even for homogenous initial conditions leading to an entirely different class of problems (Szeri et al., 1991). However, the basic phenomenology of the orientation field for passive director advection in 2D chaotic flow matches the passive scalar problem quite closely.

Despite extensive study of the dynamics of fibers in fluid flows (Guazzelli and Hinch, 2011; Voth and Soldati, 2017), we still do not have a clear phenomenology of the fiber orientation field in chaotic and turbulent flows. Szeri *et al.* (Szeri, 1993; Szeri and Leal, 1993, 1994; Szeri et al., 1991, 1992) analyzed the orientation dynamics of microstructured fluids in a framework applicable to rigid fibers as well as deformable microstructure such as polymers. Their mathematical formalism describes cases where the fluid flow experienced by a particle is steady or periodic in time. In these simple cases, they already found a rich range of phenomenology including chaotic dynamics of particle orientations. Because these flows have integrable translational motion of particles, many interesting features of passive scalar advection do not yet occur. Two studies that explored the orientation field of passive directors in flows with chaotic fluid trajectories were performed by Wilkinson and co-workers (Bezuglyy et al., 2010; Wilkinson et al., 2009). They used a random flow in which they highlighted the existence of scar lines and topological singularities. Another study by the same team (Wilkinson et al., 2010) extended the work of Szeri *et al.* on flows with integrable translational trajectories. Parsa et al. (2011) performed an experimental study in which they measured the orientation of fibers in 2D chaotic and turbulent flows and identified how tools from continuum mechanics can be used to quantify fluid stretching and understand fiber orientations. They only considered single fibers and not the spatial field of fiber orientation.

Another line of research has explored the alignment and curvature of fluid elements in chaotic and turbulent flows. Fluid element orientation is closely related to passive director orientation, and so the curvature of fluid elements is related to the spatial gradient of the passive director orientation. Pope *et al.* used direct numerical simulations to analyze the curvature of material elements in turbulent flows (Pope, 1988; Pope et al., 1989). They found that the probability distribution of curvature approaches an asymptotic form while the mean square curvature diverges exponentially. In 2D chaotic flows, the field of stretching and curvature of fluid elements has been analyzed to understand mixing (Giona et al., 1999; Liu and Muzzio, 1996; Thiffeault, 2004). Among other things, these studies explore a correlation between curvature and low stretching which was first observed in a study of model turbulent flow (Drummond and Münch, 1991). One particularly relevant result is the existence of asymptotic directionality in 2D time-periodic flows which causes fluid element orientations to approach a persistent pattern (Giona et al., 1999) similar to the persistent patterns observed in passive scalar advection (Pierrehumbert, 1994; Rothstein et al., 1999).

There are several other problems where the spatial field of director orientations is studied. Work on nematic liquid crystals has developed many of the tools to study these fields (de Gennes and Prost, 1995). Active nematics such as films of microtubules and molecular motors add additional dynamics to the nematic liquid crystal problem (Giomi, 2015; Keber et al., 2014). Studies of pattern formation in Rayleigh Bénard convection also involve director fields formed by the orientation of convection rolls (Cross and Hohenberg, P. C., 1993; Egolf et al., 1998). Studies of the polarization orientation in optics also involve a similar director field (Dennis, 2008; Flossmann et al., 2008). Recent work has shown the importance of director fields in the dynamics of cells (Duclos et al., 2017; Kawaguchi et al., 2017; Saw et al., 2017). These director fields all necessarily produce similar topological singularities, primarily those with a $\pm 1/2$ Poincaré index, which are like the core and delta ridge patterns first identified in the study of fingerprints. We will see that the fluid passive director problem is an interesting case to contrast with the others. It is a limiting case where the lack of interactions between directors leads to patterns with many features in common with patterns in the passive scalar problem.

In this paper we identify the key coherent structures in fiber orientations in chaotic 2D flows and the mechanism by which they form. We find that the topological singularities that have received extensive attention are not central to understanding fiber orientation fields. Instead, it is scar lines (Wilkinson et al., 2009) that dominate the fiber orientation fields and we identify the mechanism that produces the emergent scar lines that dominate the field at long times.

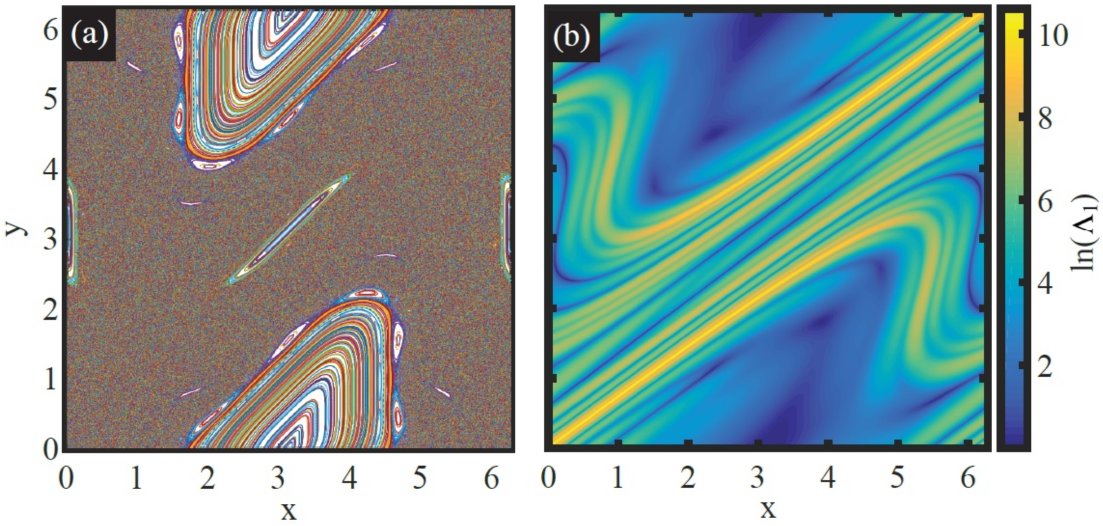

Figure 2.1: (a) Poincaré section of the standard map showing the regular regions and chaotic regions for $K = 2$. (b) Stretching experienced by the fluid over four periods at the same value of K, where Λ_1 is the eigenvalue of the Cauchy-Green strain tensor defined in the Appendix.

2.2 Phenomenology of passive director orientation in the standard map

We study passive directors advected in the standard map, which is a convenient model for a two-dimensional fluid flow that exhibits Lagrangian chaos. The standard map is area preserving and invertible; it is defined as (Lichtenberg and Lieberman, 1992)

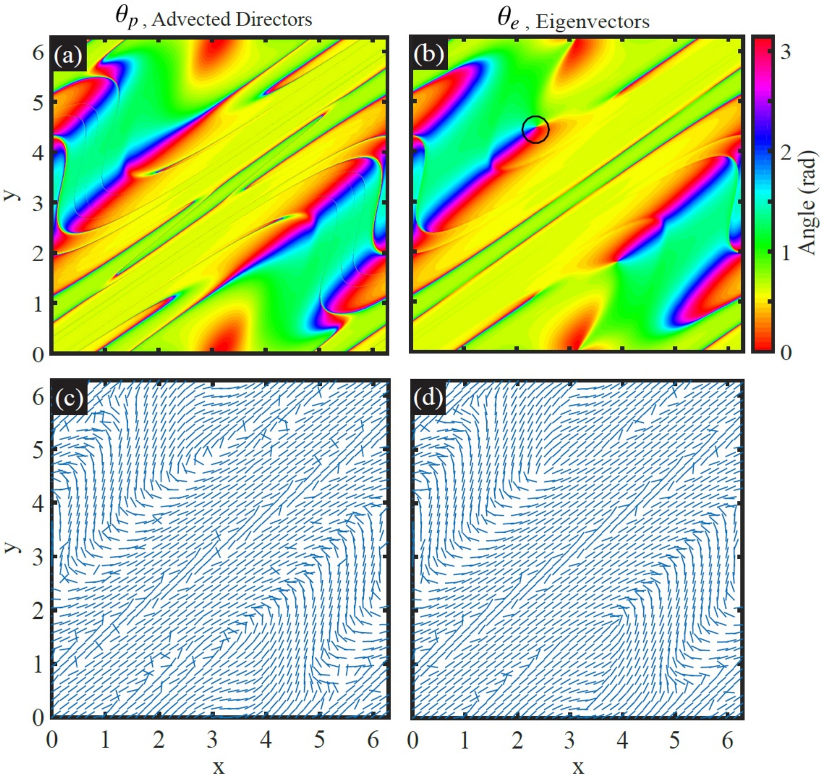

Figure 2.2: (a) Angle of the advected directors, θ_p, of initially horizontal fibers. (b) Angle of the eigenvectors of the left Cauchy-Green strain tensor, θ_e. (c) and (d) Director representations of (a) and (b), respectively. All angles are measured with respect to horizontal. Animations of all four of these figures are included as Supplemental Material (Supplemental). (Here $K = 2$ and $t = 4$.)

$$y_{t+1} = y_t + K \sin x_t \tag{2.1}$$

$$x_{t+1} = x_t + y_{t+1} \tag{2.2}$$

where spatial coordinates x and y are periodic over 2π, and t is an integer that specifies the time measured in periods that the flow has been iterated. This is often called the kicked rotor system and q and p are used instead of x and y for the phase space variables of the Hamiltonian dynamical system. The standard map can be produced by a continuous flow field with the velocity in the first half of each period given by $\dot{x} = 0$ and $\dot{y} = \frac{2K}{T} \sin x$ and in the second half of each period the velocity is given by $\dot{x} = \frac{2}{T} y$ and $\dot{y} = 0$. This flow alternates between a vertical Kolmogorov flow and a horizontal linear shear. A visualization of passive scalars in this flow is shown as an animation in the Supplemental Material (Supplemental).

Figure 2.1(a) shows the Poincaré section for the standard map for $K = 2$ with the regular and chaotic regions clearly visible (Ott, 2002). Figure 2.1(b) shows the field of fluid stretching often called the finite-time Lyapunov exponent field which is used to visualize Lagrangian coherent structures (Haller, 2015; Voth et al., 2002a).

The orientation of a fiber advected in the flow defined by the standard map is

$$\theta_{t+1} = \arctan\left(\frac{K \cos x_t + \tan\theta_t}{1 + K \cos x_t + \tan\theta_t}\right). \tag{2.3}$$

The orientation field of advected fibers can be defined in two different ways (Bezuglyy et al., 2010). Fibers with initial orientation field $\hat{p}_0(\mathbf{r})$ evolve over time t to a final orientation field $\hat{p}(\mathbf{r}, t)$. We will call this final orientation field the advected director field. In two dimensions, this field is most easily represented by an orientation angle field $\theta_p(\mathbf{r}, t)$. Alternatively, each point can have a distribution of initial orientations, $P_0(\hat{p}, \mathbf{r})$, which evolves under the flow to a distribution of final orientations, $P(\hat{p}, \mathbf{r}, t)$. The orientation field is then defined by the final preferred orientation of fibers at any point in space. In the simplest case with uniformly distributed initial orientations, the preferred orientation can be obtained as the eigenvector of the left Cauchy-Green strain tensor (CGST) that corresponds to the maximum eigenvalue, which we denote by $\hat{e}_{L1}$. We will call this the eigenvector field and represent it by the orientation angle field $\theta_e(\mathbf{r}, t)$. The left Cauchy-Green Strain tensor is $\mathbf{C}^{(L)} = \mathbf{F}\mathbf{F}^T$ where $F_{ij} = \frac{\partial x_i}{\partial X_j}$ is the fluid deformation gradient (Malvern, 1969; Ni et al., 2014; Parsa et al., 2011), also referred to as the monodromy matrix (Bezuglyy et al., 2010). An equivalent definition is to use an eigenvector of the tensor order parameter (de Gennes and Prost, 1995). The Appendix discusses the definitions and relationships between these quantities in more detail. An important distinction between the advected director orientation field, $\theta_p(\mathbf{r}, t)$ and the eigenvector orientation field, $\theta_e(\mathbf{r}, t)$, is that θ_p depends on a choice of initial orientation while θ_e does not.

The two orientation fields, θ_p and θ_e, are shown in Fig. 2.2 at time $t = 4$. Both the fiber fields [Figs. 2.2(c) and 2.2(d)] and higher resolution color maps of the orientation angles [Figs. 2.2(a) and 2.2(b)] are shown. The two different definitions of the fiber orientation field are quite similar, but there are some clear differences. For example, at $(x, y) = (2.37, 4.48)$ in Fig. 2.2(b) we see that there is a pinwheel where the eigenvector orientation is not defined, a topological singularity, while at this point, the advected director field in Fig. 2.2(a) is smooth. We show in Sec. 2.3 that these fields have very different topological structure and yet as observed by Wilkinson et al. (2009), they converge toward the same field at long times in chaotic regions of the flow.

An effective way to observe the dominant coherent structures in the orientation fields is to calculate the gradient of the fiber orientation, as shown in Fig. 2.3. In both the advected director field [2.3(a)] and the eigenvector field [2.3(b)], the dominant features are thin lines over which the orientation changes by π over a very short distance. These have been called scar lines by Wilkinson et al. (2009).

The basic mechanism for formation of a scar line is simple. When fluid is stretched by the flow, fibers rotate toward alignment with the stretching direction. However, some fibers that are initially perpendicular to the stretching direction will not align. The set of points with initial orientations that are exactly perpendicular to the stretching direction fall on lines. In chaotic regions of the flow where stretching increases exponentially in time, the width of the perpendicular region is shrinking exponentially in time, causing the orientation field to rotate by π across very short distances.

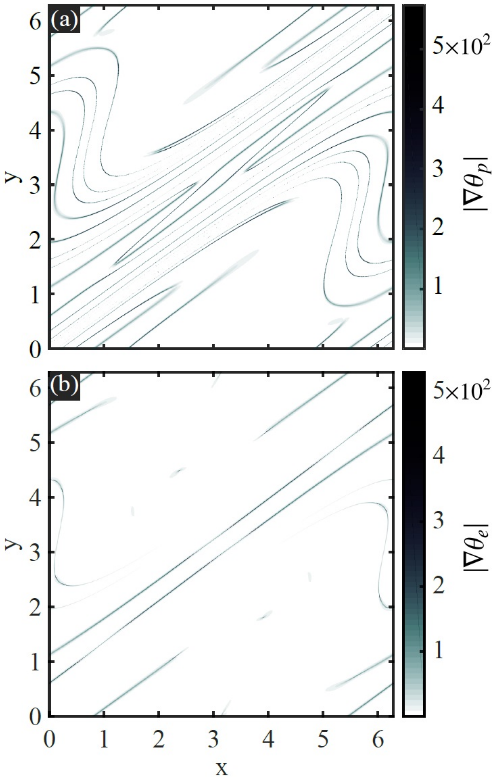

Figure 2.3: Gradient of the angle of the fiber orientation field after advection in the standard map for four periods. (a) Gradient of the advected director field starting with initially horizontal fibers. (b) Gradient of the eigenvector field. The large gradients lie on thin lines called scar lines (Wilkinson et al., 2009). (Here $K = 2$ and $t = 4$.)

It is not immediately obvious how the mechanism in the preceding paragraph creates scar lines in the eigenvector field. Wilkinson *et al.* briefly identify type 2 scar lines as lines that form where rotational regions with complex eigenvalues of the deformation gradient (or monodromy) matrix have repeatedly been stretched and folded so that they become very narrow. Complex eigenvalues appear where the trace of the monodromy matrix is between -2 and 2. We find that the scar lines in the eigenvector field appear in regions of low stretching that are often associated with these stretched rotational regions. However, the mechanism we observe for the formation of scar lines in the eigenvector field does not clearly match the definition of type 2 scar lines by Wilkinson *et al.*. In Sec. 2.4.2 we show how the scar lines in the eigenvector field emerge as the result of an initial stretching that creates a preferred orientation. When the later stretching experienced by that fluid element is perpendicular to the initial stretching, a scar line is created. We call these emergent scar lines and find that they dominate the orientation field of both advected directors and stretching eigenvectors at large times. The reversal of stretching results in scar lines being associated with regions of low stretching, connecting with earlier observations that curvature of fluid elements preferentially occur in regions of low stretching (Drummond and Münch, 1991; Liu and Muzzio, 1996; Thiffeault, 2004). The mechanism for creation of emergent scar lines is similar to the mechanism for creation of type 1 scar lines except that the stretching over an initial time interval replaces the initial fiber orientation. At large times, type 1 scar lines become unobservably thin so that emergent scar lines that have been formed in the recent past dominate the observed orientation fields. In Sec. 2.4.3 we show how these emergent scar lines can be labeled by the time since their creation.

A major focus in previous work on the evolution of director fields has been the development of topological singularities or topological defects (Bezuglyy et al., 2010; Cross and Hohenberg, P. C., 1993; de Gennes and Prost, 1995; Egolf et al., 1998; Giomi, 2015; Keber et al., 2014; Wilkinson et al., 2010). To conserve the total topological charge of the field, singularities must always form in pairs of opposite Poincaré indices. The two types of singularities that form in director fields are shown in Fig. 2.4. Figures 2.4 (a) and 2.4(c) show a singularity that has a Poincaré index of $+\frac{1}{2}$; and Fig. 2.4 (b) and (d) show a singularity which has a Poincaré index of $-\frac{1}{2}$. The Poincaré index is defined as the number of multiples of 2π in which the director orientation changes as we move around a closed loop. These singularities are given different names by different communities. The terminology from fingerprint analysis is core for $+\frac{1}{2}$ and delta for $-\frac{1}{2}$.

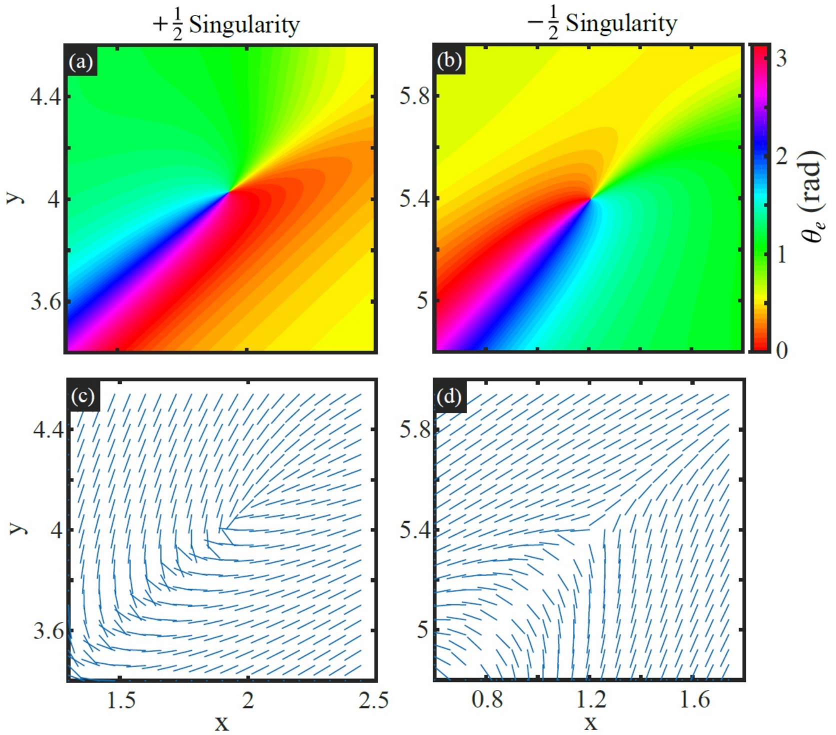

Figure 2.4: The two different types of singularities. (a) and (b) Angle of $\hat{e}_{L1}$ with respect to the horizontal. (c) and (d) Director representation of the eigenvector field. (a) and (c) show a singularity with a Poincaré index of $+\frac{1}{2}$ and (b) and (d) show a singularity with a Poincaré index of $-\frac{1}{2}$. To determine the Poincaré index, circle the singularity of (c) in the clockwise direction. Around the circle, the orientation of θ_e rotates by π in the clockwise direction, giving a Poincaré index of $+\frac{1}{2}$. (Here $K = 2$ and $t = 2$.)

They are also called wedge and trisector (Karrasch et al., 2014), and in the study of optical polarization fields there are similar singularities called star and lemon (Flossmann et al., 2008). Recent work on patterns in cell populations has used 'comet-like' for $+\frac{1}{2}$ singularities (Duclos et al., 2017; Kawaguchi et al., 2017; Saw et al., 2017).

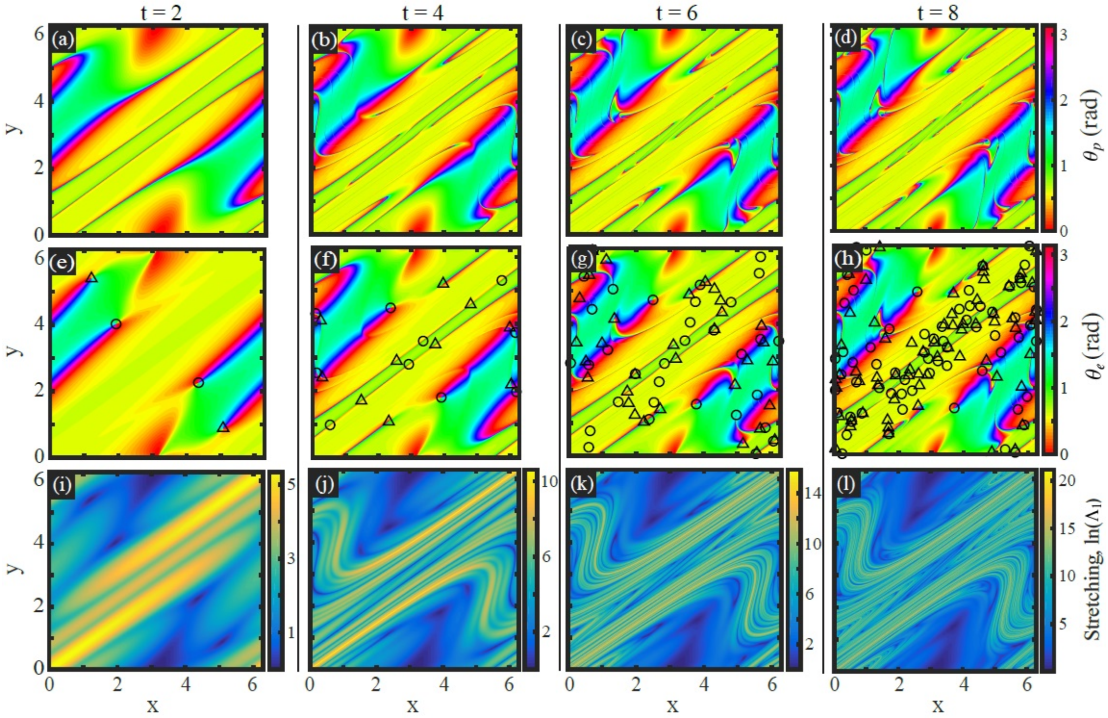

Figure 2.5: (a)-(d) Angle of advected directors, θ_p, measured from horizontal over the time interval $t = 2$, 4, 6, and 8. (e)-(h) Angle of stretching eigenvectors, θ_e, over the same time intervals with singularities marked: ○, $+\frac{1}{2}$ singularities; △, $-\frac{1}{2}$ singularities. (i)-(l) Stretching experienced by the fluid for the same time intervals. Animations of these three fields are provided as Supplemental Material (Supplemental). (Here $K = 2$.)

2.3 Topological singularities in passive director orientation fields

Figure 2.5 shows how the orientation fields and the stretching field develop from $\Delta t = 2$ to 8. As time progresses, the structure of the advected director field θ_p and the eigenvector field θ_e become more alike. However, certain regions are still different. The differences occur in regions of low stretching that are either in the elliptic islands of the flow (see Fig. 2.1) or within the thin lines where the stretching is small.

In Fig. 2.5(a)-2.5(h) the topological singularities are marked with circles and triangles. The eigenvector field continuously develops new topological singularities while the advected director field always remains free of them. This difference occurs because the directors start as a smooth field and are advected by a smooth flow, so it is not possible for topological singularities to form (Wilkinson et al., 2009). In contrast, the stretching eigenvector field nucleates pairs of singularities at points where the stretching is zero. An animation showing the generation of singularities in the field of θ_e is provided as Supplemental Material (Supplemental).

Figure 2.6 shows a plot of the number of singularities in the stretching eigenvector field at each period, N. After an initial transient, the number of singularities grows exponentially. A least squares fit to $t > 5$ gives $N = 7.5\, e^{0.36t}$. The exponential can be understood as the result of a process similar to a baker's map where the thin lines of low stretching are folded on themselves multiple times. New singularities are nucleated in these low stretching regions, so the number of new zeros in the stretching at each period is proportional to the current number of zeros.

The number of singularities were calculated computationally by performing a non-linear search for minima where the stretching field is near unity. At these points that have not been stretched, the eigenvector field has no preferred orientation, allowing a singularity in the field of θ_e. Serra and Haller (2017) have shown that care is required because integrating trajectories in noisy or intermittent velocity fields can create artificial singularities in the stretching eigenvector field. We have not observed any artificial singularities, likely because of the simple analytic expressions for the standard map. The number of singularities is increasing rapidly with time, while the spatial extent over which the stretching is near unity becomes very small. As a result, it becomes increasingly difficult to find all the singularities as time progresses. We will see that the shrinking of the size of the region affected by each singularity allows the exponentially increasing number of singularities to become less and less important to the orientation field as time progresses.

By comparing the number of singularities found in separate computations with a very large number of initial guesses, we confirmed that we were able to find all singularities up to $t = 10$, but by $t = 12$ it is clear that we were missing a significant number and so we only report data up to $t = 10$. To characterize the topological charge (Poincaré index) of the singularities we move around each singularity in a small loop (500 points around a circle of radius 10^{-5}) and calculate the change in orientation of fibers around that loop.

Since the flow is defined by a simple analytic map, we can calculate the positions at which singularities form over the first few periods. At a singularity, the stretching is zero and so the deformation gradient **F** represents a pure rotation. Here we analytically calculate the positions of singularities that appear over the time range $t = 1.5-2$. The position of a fluid element initially at (x_0, y_0) advected over time $t = \frac{3}{2} + \frac{\varepsilon}{2}$, where $0 \leq \varepsilon \leq 1$, is

$$\begin{pmatrix} x_{1+\varepsilon} \\ \\ y_2 \end{pmatrix} = \begin{pmatrix} x_0 + (1+\varepsilon)(y_0 + K\sin x_0) \\ +\varepsilon K \sin(x_0 + y_0 + K\sin x_0) \\ \\ y_0 + K\sin x_0 \\ +K\sin(x_0 + y_0 + K\sin x_0) \end{pmatrix} \tag{2.4}$$

Singularities can exist at points where the deformation gradient F calculated from from Eq. 2.4 is a pure rotation so it satisfies $F_{11} = F_{22}$ and $F_{12} = -F_{21}$.

The points that satisfy this condition are:

$$\begin{cases} x_0 = 2\pi m + \cos^{-1}\left(\frac{-1\pm\varepsilon}{K}\right) \\ \\ y_0 = 2\pi l \pm \cos^{-1}\left(\frac{(1+\varepsilon)\cos x_0}{1-\varepsilon-2\varepsilon\cos x_0}\right) - x_0 - 2\sin x_0 \end{cases} \tag{2.5}$$

and

$$\begin{cases} x_0 = 2\pi m - \cos^{-1}\left(\frac{-1\pm\varepsilon}{K}\right) \\ \\ y_0 = 2\pi l \pm \cos^{-1}\left(\frac{(1+\varepsilon)\cos x_0}{1-\varepsilon-2\varepsilon\cos x_0}\right) - x_0 + 2\sin x_0 \end{cases} \tag{2.6}$$

where l and m are integers. Note that these are initial coordinates (x_0, y_0). The position of singularities are the final coordinates, $(x_{1+\varepsilon}, y_2)$, which are obtained by inserting the values we find for (x_0, y_0) into Eq. (2.4). For $\varepsilon = 0$ and 1, the positions of the singularities are periodic over 2π. For $0 < \varepsilon < 1$, we choose m and l so that the final singularity positions lie within $[0, 2\pi]$.

These analytical calculations for the position of singularities agree exactly with the positions found computationally in Fig. 2.5(e). Figure 2.5(e) shows only four singularities, because out of the eight singularities in Eqs.(2.5) and (2.6), four come together in pairs and annihilate at the large elliptical island leaving four singularities after two periods while conserving the total topological charge throughout the process. The dynamics of the generation and annihilation of singularities in the stretching eigenvector field are shown in an animation that has been provided as Supplemental Material (Supplemental).

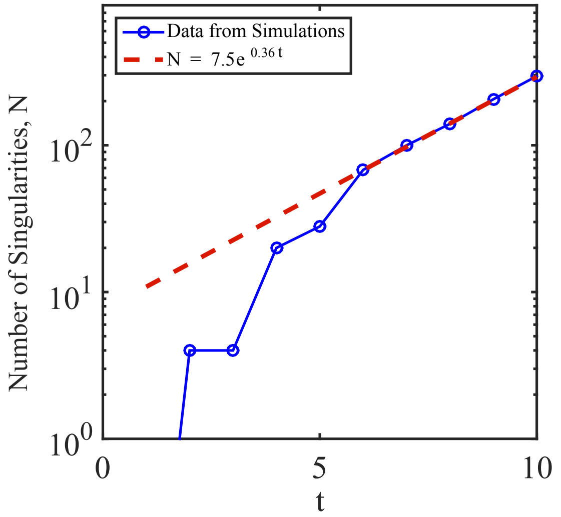

Figure 2.6: Number of singularities N as a function of time. At later times the number of singularities increases exponentially. (Here $K = 2$.)

2.4 Scar lines in passive director orientation fields

The orientation fields of advected directors and stretching eigenvectors become very similar to one another and approach a stationary state in the long time limit, as is evident in Fig. 2.5. In Fig. 2.7 these fields are shown at $t = 10$. In the chaotic regions of the flow, the two fields appear to become almost identical in the long-time limit, reflecting the persistent pattern (Pierrehumbert, 1994; Rothstein et al., 1999) or asymptotic directionality (Giona et al., 1999) that has been observed in other work on time-periodic 2D flows. However, the fields are also diverging in topology since there is an exponentially increasing number of singularities in the field of stretching eigenvectors, θ_e. Since the two fields converge throughout almost the entire chaotic region and yet have completely different topologies, the key coherent structures in these fields are apparently not the topological singularities. Figure 2.3 suggests that instead, the key coherent structures are thin lines across which the fiber orientation rotates by π. Wilkinson et al. (2009) have called these structures scar lines. In the long-time limit the topological singulari-

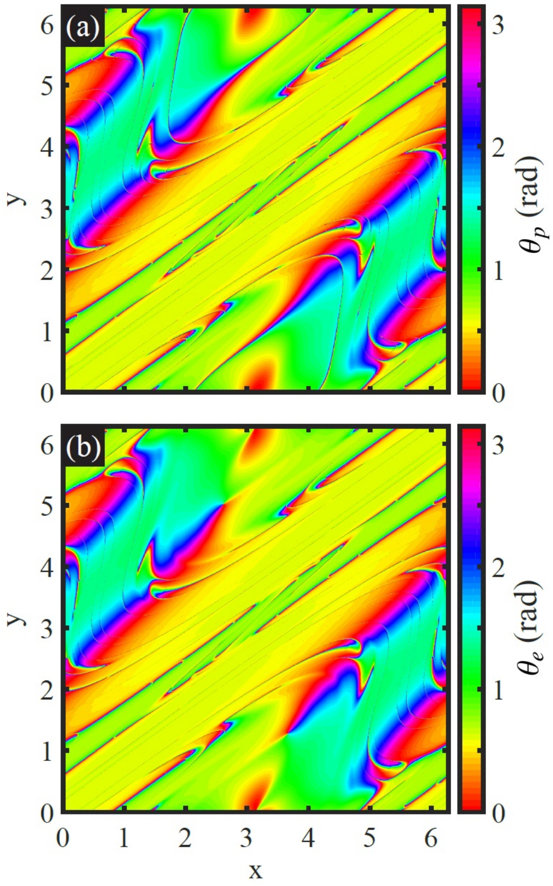

Figure 2.7: Orientation fields at longer times that show the persistent pattern that appears in the chaotic region of both fields. (a) Orientation field of the advected directors θ_p. (b) Orientation field of the stretching eigenvectors θ_e. (Here $K = 2$ and $t = 10$.)

ties only affect an infinitesimally small region of the stretching eigenvector orientation field and are screened by the scar lines that come to be the dominant features of the field.

2.4.1 Type 1 scar lines

Type 1 scar lines form in the advected director field at points where the initial fiber orientation is perpendicular to the direction that the fluid will be stretched. The right

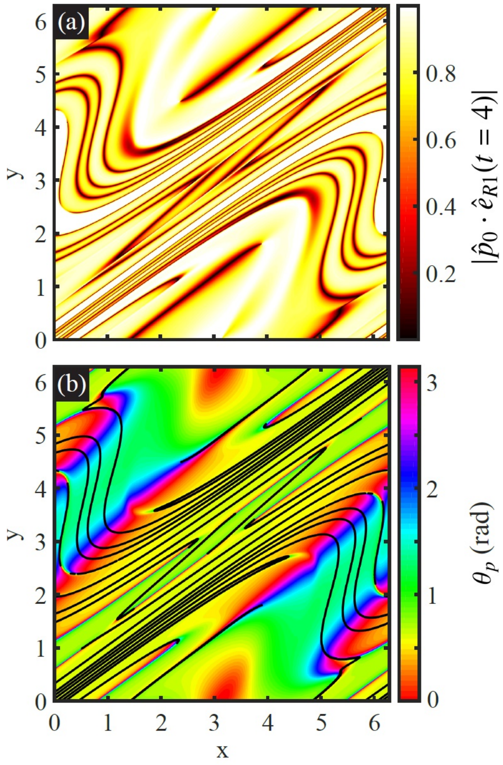

Figure 2.8: Locations of type 1 scar lines where the initial fiber orientation is perpendicular to the direction the fluid will be stretched. (a) Dot product of the initial orientation with the maximum eigenvector of the right CGST $\hat{p}_0 \cdot \hat{e}_{R1}$. (b) Locations where $\hat{p}_0 \cdot \hat{e}_{R1} < 0.03$ superimposed on the stretching eigenvector orientation field. (Here $K = 2$ and $t = 4$.)

Cauchy-Green strain tensor, $\mathbf{C_R} = \mathbf{F^T F}$ (see the Appendix), has eigenvectors that indicate the directions of stretching in initial particle coordinates (Malvern, 1969; Parsa et al., 2011). In Fig. 2.8(a), we show the dot product of initial fiber orientation with $\hat{e}_{R1}$, the extensional eigenvector of the right Cauchy-Green strain tensor. Type 1 scar lines form where this dot product is zero. Figure. 2.8(b) shows the locations where this dot product is less than 0.03 superimposed on the advected director field. The match with the locations of most of the scar lines is very good. Some of the locations with a zero dot product do not initially appear to be scar lines, but at higher resolution it becomes clear that the scar line had simply become too thin to see at the 2000 × 2000 resolution of the plotted orientation field. This healing of type 1 scar lines was identified by Wilkinson et al. (2009), and here we see that in this flow it only takes four periods for many of the type 1 scar lines to become too thin to be observed. There are other points at which scar lines appear, but the zero dot product condition from Fig. 2.8(a) is not met. These will be the topic of Sec. 2.4.2.

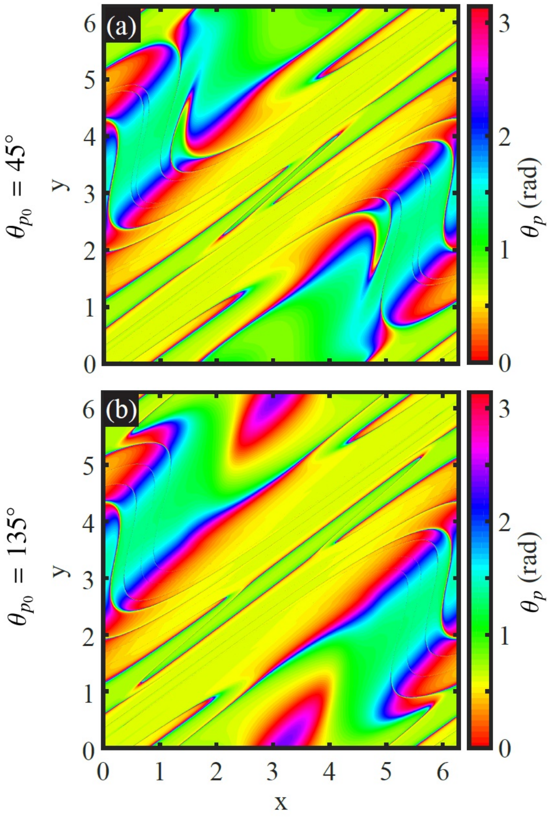

Figure 2.9: Sensitivity of the advected directors and type 1 scar lines to initial orientation. (a) Orientation field θ_p of an initially uniform grid of directors with an angle of +45°. (b) Orientation field θ_p of an initially uniform grid of directors with an angle of +135°. (Here $K = 2$ and $t = 4$.)

Due to their production mechanism, the type 1 scar lines are sensitive to initial orientations of the advected directors. In Fig. 2.9 the orientation field for the advected directors, θ_p, is shown for two different uniform initial orientation angles. It can be seen from this figure that although the two have differences caused by their initial orientations, the structure and topology of the field remains mostly the same and are mainly dominated by another type of scar line that is similar in both fields and independent of initial orientations. We identify these scar lines as emergent scar lines.

2.4.2 Emergent scar lines

In this section we study the mechanism that creates scar lines that are independent of initial conditions and the distant past history of the flow. We find that the dominant structures in the fields of both θ_e and θ_p are emergent scar lines that develop when the recent stretching of a fluid element is orthogonal to the stretching it experienced earlier. We have established that after sufficient time, there is a persistent pattern in the fiber orientation field. This orientation pattern can be thought of as the initial orientation field for the flow over the next time interval. The structures with a large gradient in the fiber orientation field occur where the stretching over the next time interval is orthogonal to the orientation produced by the stretching of the previous time interval. Quantitatively, a scar line will emerge where the stretching over some initial interval, which is defined by $\hat{e}_{L1}$, is perpendicular to the stretching the fluid element will experience in a future interval $\hat{e}_{R1}$. Since we are using a periodic flow, we can calculate these stretching directions at any time and identify the locations where the initial stretching is orthogonal to the later stretching.

Figure 2.10 verifies this mechanism for the formation of emergent scar lines. Figure 2.10(a) shows the dot product of the stretching that the fluid has experienced over three periods $\hat{e}_{L1}(\Delta t = 3)$ with the stretching that the fluid will experience for the one remaining period $\hat{e}_{R1}(\Delta t = 1)$. The dot product of these vectors should be zero at the locations of the emergent scar lines for $\Delta t = 4$, and Fig. 2.10(b) shows this condition, and marks precisely the locations of the scar lines in the stretching eigenvector field in the

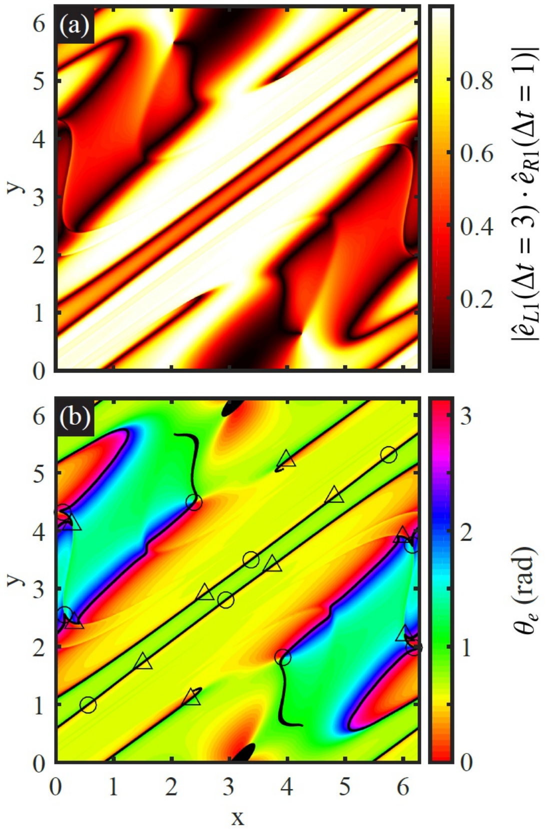

Figure 2.10: Locations of emergent scar lines. (a) Dot product of the maximum eigenvector of the left CGST for three periods and the maximum eigenvector of the right CGST for one period $\hat{e}_{L1}(\Delta t = 3) \cdot \hat{e}_{R1}(\Delta t = 1)$. (b) Locations where $\hat{e}_{L1}(\Delta t = 3) \cdot \hat{e}_{R1}(\Delta t = 1) < 0.03$ superimposed on the stretching eigenvector orientation field. (Here $K = 2$ and $t = 4$.)

chaotic region of the flow at $t = 4$. In the large regular islands, the stretching is small and some spurious points meet the condition of the dot product without developing scar lines.

Figure 2.11 demonstrates the mechanism by which emergent scar lines and singularities are generated in the eigenvector field. This simple schematic flow consists of two steps. First, the initially circular fluid elements experience a non-uniform flow field that stretches and rotates them to the arrangement shown in Fig. 2.11(b). Second, the fluid elements experience a uniform pure strain flow with a horizontal extension direction that results in the shapes in Fig. 2.11(c). In this process there are points where the initial stretching experienced by some fluid elements is exactly canceled by later stretching. These points lie on the emergent scar lines where the direction of the previous stretching is perpendicular to the later stretching. These points that experience no net stretching are the singularities of the stretching eigenvector field. Figure 2.11(d) shows a director representation of the final configuration of the stretching direction with the singularities marked.

2.4.3 Age of emergent scar lines

An emergent scar line forms when earlier stretching is reversed by later stretching. The time that divides earlier from later is different for different scar lines. Here we show how each emergent scar line can be labeled with its age defined as the time since its maximum stretching occurred and reversal of stretching began. Since stretching increases exponentially and scar line thickness decreases exponentially, there is often an age beyond which the emergent scar lines become so thin that they are below the resolution of interest. In experiments, there will be resolution limits and translational diffusion that will remove old scar lines that have become sufficiently thin. The scar lines that are young enough to remain visible at the resolution of interest dominate the passive director orientation field.

In Fig. 2.12 we show a field indicating the time when the maximum stretching occurred for each fluid element. Most of the field is white, indicating that the maximum stretching is at the current time. The thick blue region indicates the points where the maximum stretching occurred one period ago. Purple indicates points whose maximum stretching was two periods ago marking an emergent scar line with an age of two periods. In this field created with an integration over six periods, we observe scar lines with ages up to four periods. (There is a part of the elliptic island that had its maximum stretching five periods ago, but without exponential stretching this does not form a scar line.) Figure 2.12(b) plots the history of the stretching at the five points marked in Fig. 2.12(a). The purple curve marked with a triangle is a topological singularity where the stretching goes to zero at time $t = 6$. It lies on an emergent scar line with age 2, labeled purple, since its maximum stretching was two periods before the present. The other four points are chosen to lie on scar lines with ages of one to four periods.

Once an emergent scar line becomes well defined so that its width is much less than the correlation length of the velocity gradients in the flow, it will be advected by the flow without being removed. Later stretching will rotate the line and decrease its width by compressing the rotation by π to a narrower region. The scar line remains where orientation was perpendicular to the later stretching, and since the scar line has orientations across the full range 0 to π; this is guaranteed to occur in some region within the scar line.

A fluid element can have multiple maxima in its stretching history so that multiple ages can be assigned to it. The age 4 point shown in red in Fig. 2.12(b) has later stretching that has almost surpassed the maximum from four periods ago. Some of these points are simply at the edge of the scar line and at longer times will cease to be part of the scar line. However, some other points have had the recent stretching become larger than the earlier stretching. This creates topological singularities by the process shown in the simple model in Fig. 2.11, and the dynamics of scar lines near these topological singularities is a topic that needs additional study. At long times, the fraction of the chaotic region where the stretching is small enough that recent stretching can overcome earlier stretching becomes very small. So an exponentially increasing number of topological singularities are occurring in a shrinking fraction of the chaotic domain in a way that allows the overall structure of the orientation field to be independent of what happens in these regions near the singularities.

2.5 Conclusions

When fibers are advected in two-dimensional flows with exponential stretching of material elements, the primary coherent structures in the fiber orientation field are scar lines over which the fiber orientation rotates by π over short distances. We have discovered that recently formed scar lines dominate the observed orientation fields. A scar line emerges in regions where the recent stretching is perpendicular to the earlier stretching of that fluid element. These emergent scar lines can be labeled by their age, defined as the time at which their stretching reached a maximum.

It is important to distinguish two different ways to quantify the director orientation field. The orientation can be defined by directors advected from a smooth initial orientation field, or it can be defined by the average orientation of an ensemble of initial orientations that can be quantified by the stretching eigenvectors. The advected director field does not develop new topological singularities, so it will always remain smooth if it starts with a smooth initial condition. However, the stretching eigenvector field does develop new topological singularities; in this chaotic flow, the number of singularities increases exponentially. Despite the very different topology, the two orientation fields converge at long times indicating that the topological singularities are not the key coherent structures in these orientation fields. Instead, emergent scar lines dominate both orientation fields at long times.

The mathematical foundations for the passive director problem are still much less developed than for the passive scalar problem (Aref et al., 2017) or for the detection of Lagrangian coherent structures in velocity fields (Haller, 2015). The close connection between the phenomenological description of passive director fields developed here and work on strange eigenmodes and Lagrangian coherent structures suggests that significant progress on mathematical foundations of the passive director problem may be possible. In particular, recent work that uses the eigenvectors of the Cauchy-Green strain tensors for coherent vortex detection (Karrasch et al., 2014; Serra and Haller, 2017) considers the same topological singularities that we study and should be able to be extended to the passive director problem.

We also hope that future work can extend these insights to the case of turbulent flows that are pervasive in industrial and environmental fiber flows. Emergent scar lines should appear in any flow with chaotic exponential stretching of material line elements. We expect that advected director fields in two-dimensional turbulence will be dominated by scar lines that are similar to the 2D chaotic flow case studied here. The Lagrangian coherent structures determined by fluid deformation in 2D chaotic flows are similar to those found in turbulent flows (Mathur et al., 2007; Twardos et al., 2008). It should be possible to determine the age of emergent scar lines in 2D turbulence and select the age most relevant to observations at a given resolution. In 3D turbulence, the situation is less clear. Methods for detection of Lagrangian coherent structures in 3D turbulence using measures of fluid stretching have shown promise (Green et al., 2007). Analysis of fluid stretching has been shown to be an effective way to understand the alignment of fibers and other non-spherical particles in 3D turbulent flows (Ni et al., 2014; Zhao and Andersson, 2016). Additional work is needed to determine whether the scar lines that dominate director orientation fields in 2D chaotic flow will appear in 3D flows.

2.6 Acknowledgments

This work was supported by NSF Grant No. DMR-1508575, Vetenskapsrådet Grant No. 2013-3992, and the Knut and Alice Wallenberg FoundationGrant No. KAW 2014.0048. We thank Stellan Ostlund, Nicholas Ouellette, and Michael Wilkinson for stimulating discussions.

2.7 Appendix

To quantify fluid deformation, consider a point in the flow that is initially at **X** and is advected after time Δt to **x**. The fluid deformation gradient is defined as $F_{ij} = \frac{\partial x_i}{\partial X_j}$. The deformation gradient includes both rotation and strain, $\mathbf{F} = \mathbf{VR} = \mathbf{RU}$, where **R** is the rotational tensor and **V** and **U** are the left and right stretch tensors respectively (Ni et al., 2014). It is convenient to extract only the strain contribution using the Cauchy-Green strain tensors. The left Cauchy-Green strain tensor, $\mathbf{C}^{(L)} = \mathbf{F}\mathbf{F}^T = \mathbf{V}\mathbf{R}\mathbf{R}^T\mathbf{V}^T = \mathbf{VV}$, has eigenvectors along the principle axes of the ellipse formed after the fluid element is deformed over Δt. The right Cauchy-Green strain tensor, $\mathbf{C}^R = \mathbf{F}^T\mathbf{F} = \mathbf{U}^T\mathbf{R}^T\mathbf{R}\mathbf{U} = \mathbf{UU}$, has eigenvectors along the initial direction that will become the principal axes after deformation. Thus the field formed by the eigenvector of the Left Cauchy-Green strain tensor gives the preferred direction toward which a fiber at that location will have rotated due to the fluid deformation. Both the right and left Cauchy-Green strain tensors have the same eigenvalues, Λ_1 and Λ_2 with Λ_1 traditionally chosen to be the maximum (extensional) eigenvector. The square root of the maximum eigenvalue gives the stretching the fluid element experiences, defined as the ratio of the final major axis of the elliptical fluid element divided by the initial diameter. The finite-time Lyapunov exponents are defined by $\lambda_i = \frac{1}{t} \ln \sqrt{\Lambda_i}$.

An alternative way to express the final preferred orientation is to calculate the eigenvectors of a tensor order parameter. The tensor order parameter that is widely used in the study of liquid crystals is

$$I_{ij} = \frac{1}{2\pi}\int_0^{2\pi} d\theta\, P(\hat{p}(\theta), \mathbf{r}, t)\,(\hat{p}_i\hat{p}_j - \frac{1}{3}\delta_{ij}). \tag{2.7}$$

Wilkinson et al. (2010) used an order parameter without the isotropic term. For initially uniform $P(\hat{p}(\theta), \mathbf{r}, t = 0)$, both of these tensor order parameters have the same eigenvectors as the left Cauchy-Green strain tensor.

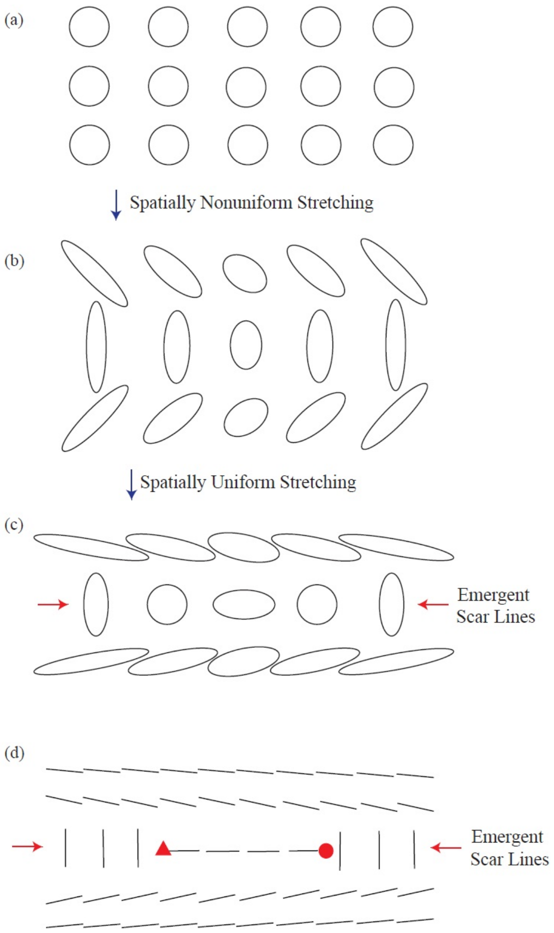

Figure 2.11: Simple schematic flow that generates singularities and emergent scar lines. (a) Uniform circular fluid elements. (b) Fluid elements after deformation by a spatially non-uniform flow field. (c) Fluid elements after a uniform pure strain flow with horizontal extension direction. Emergent scar lines form in the second row of fluid elements where the uniform stretching is orthogonal to the initial non-uniform stretching. (d) Director representation of the stretching eigenvector after the two stretching steps. The circle represents a $+\frac{1}{2}$ singularity and the triangle a $-\frac{1}{2}$ singularity.

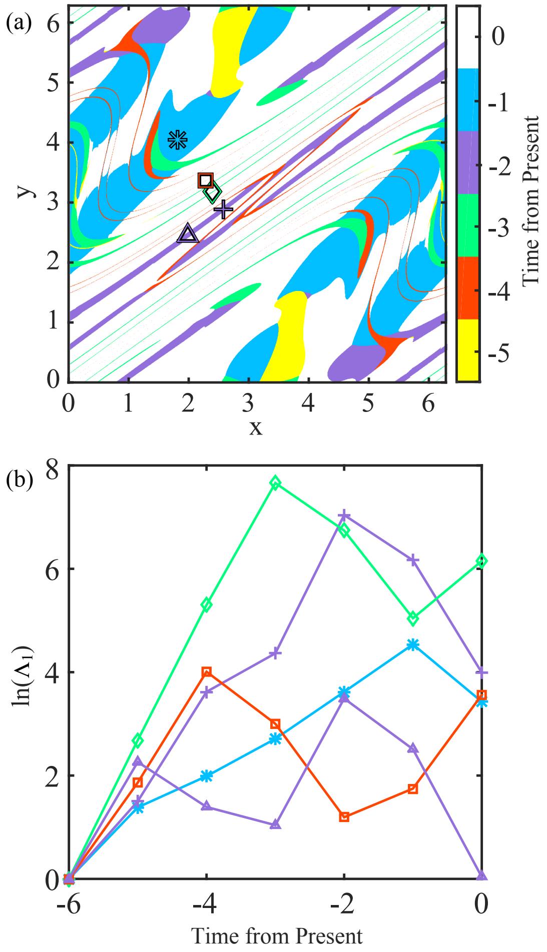

Figure 2.12: Quantifying the age of emergent scar lines. (a) Field showing the time at which each fluid element experienced maximum stretching, which we use to define the age of emergent scar lines. Most of the field is white, indicating that maximum stretching occurs at the current time, but several generations of scar lines appear with maximum stretching before the present time. (b) Stretching as a function of time for points that lie on emergent scar lines of different ages. $*$, age 1 emergent scar line; $+$, age 2; $\diamond$, age 3; $\Box$, age 4; $\triangle$, $-\frac{1}{2}$ singularity on emergent scar line of age 2. (Here $K = 2$ and $t = 6$.)

Chapter 3

Using deformable particles for single particle measurements of velocity gradient tensors

Sections 3.1 to 3.6 of the following chapter are from a manuscript that has been published in *Experiments in Fluids* (Hejazi et al., 2019) where we examine deformable particles in different fluid flows as a new measurement technique for measuring the fluid velocity gradient tensor. The remaining section of this chapter, Sec. 3.7, is related to additional work that we have done since the publication of the manuscript regarding deformable particles in turbulence and our efforts in measuring their deformations.

3.1 Introduction

The deformation of structures by fluid flows plays a central role in many environmental, biological, and engineering situations and so has long been a focus of research (Alben et al., 2002; Ezzeldin et al., 2015; Guo et al., 2017; Marchioli and Vincent, 2019; Qian et al., 2008; Rosti et al., 2019; Stockie and Green, 1998). Recently, the ability to measure and simulate the rotations (Voth and Soldati, 2017) and deformations (Allende et al., 2018; Dotto and Marchioli, 2019; Gay et al., 2018; Rosti et al., 2018) of small particles advected in turbulent flows has provided substantial new insights about particle-turbulence interactions as well as the structure of turbulence itself. But a clear quantification of what features of the flow can be measured from deformations of particles has been lacking.

Fibers have been a primary focus of prior work on deformable particles in turbulence. This is natural since slender fibers are easily deformable and simple to fabricate. However the deformation of fibers is a special case that is somewhat more complex than the deformation of other particles. A flow with a uniform velocity gradient rotates but does not bend straight material lines. Fibers can still deform in uniform velocity gradients if there is a compressive stress that exceeds the buckling threshold. Below this threshold, deformation of fibers is a result of curvature of the velocity field.

Buckling is caused by a compressive viscous drag acting on a fiber. For turbulent velocity gradients characterized by shear rate $\dot{\gamma} = (\sqrt{15}\tau_\eta)^{-1}$, the axial viscous force from slender body theory is proportional to $\mu L^2/[\tau_\eta \log(2\kappa)]$, where L is the fiber length, μ is the dynamic viscosity, τ_η is the Kolmogorov time scale of the flow, and κ is the aspect ratio (L/D) where D is the fiber diameter. Buckling is resisted by the elastic restoring force which scales as EI/L^2, where E is the Young's modulus and I is the second moment of area which is proportional to D^4 for cylindrical fibers. Buckling instabilities occur when the ratio of compressive viscous drag to the elastic restoring force $Z = 2\pi\mu L^4/[\sqrt{15}\tau_\eta EI \log(2\kappa)]$ exceeds a threshold. Several different conventions for the constant in this non-dimensional number exist in the literature, and we have chosen to follow (Becker and Shelley, 2001) who find that for a free fiber in pure strain flows, the buckling instability occurs at $Z \geq 153.2$ (Becker and Shelley, 2001; Young and Shelley, 2007). In turbulent flows, much larger values of Z are necessary to obtain buckling in a significant fraction of particles (Allende et al., 2018). Brouzet et al. (2014) experimentally measured deformations of long fibers in turbulence. For fibers short enough to be in uniform velocity gradients, their approach of quantifying turbulent power produces the same scaling as the buckling instability. In practice it is quite difficult to obtain particles flexible enough and viscous stresses large enough to observe buckling of fibers in turbulence when the fiber length is small enough to experience uniform velocity gradients. For example, the particles we use in this paper have $0.005 < Z < 0.007$, and are still not shorter than the Kolmogorov length.

Initial deformation of a straight fiber at shear rates below the buckling instability comes from curvature of the velocity field. Velocity differences over the length of the fiber due to curvature of the velocity field scale as $L^2/(\tau_\eta \eta)$, where η is the Kolmogorov length scale of the flow, so the viscous drag due to curvature is proportional to $\mu L^3/[\tau_\eta \eta \log(2\kappa)]$. The ratio of the viscous drag and elastic restoring force in this case is then proportional to ZL/η. Thus bending due to curvature is less important than buckling for small fibers with $L/\eta \ll 1$. However, bending does not have a threshold, so small deformations of fibers near the Kolmogorov length could be dominated by curvature rather than buckling in certain conditions. For longer fibers, curvature and buckling both play a role which leads to fascinating dynamics (Ali et al., 2016; Gay et al., 2018; Rosti et al., 2018), but makes it difficult to use deformation as a measurement technique.

However, there exists a simpler regime where particle deformation can be related to local uniform velocity gradients without a buckling threshold. The key is to leave the slender limit since a particle that is spatial extended in more than one direction will deform in a uniform strain. In practice most particles that are not slender fibers are too rigid to deform in the fluid velocity fields typically encountered in turbulence, so this approach may seem impractical. However, a particle made of several connected slender arms will deform in uniform strain and can be made highly flexible. In a uniform velocity gradient, a particle made of flexible cylindrical arms will deform by an angle that scales as $\delta\theta \propto \mu L^4/(\tau_\eta EI) \propto Z$, the same scaling as the buckling transition but without a threshold or directional selectivity. The effects are even greater if a weak link is introduced so that the arm flexibility is larger than that of a straight cylinder. If an arm bends at its weak link with a spring constant k when torque τ is applied, $\tau = k\delta\theta$, then the deformation due to uniform velocity gradients scales as

$$\delta\theta \propto \mu L^3/(k\tau_\eta), \tag{3.1}$$

which is lower order in the aspect ratio of the arm than buckling and bending from curvature in the velocity field. A more detailed derivation of this result is offered in the appendix.

In this paper, we show that particles made of slender arms with weak links near the junction are promising tools for measuring the full velocity gradient tensor in incompressible flow by imaging a single particle trajectory. Such particles can be fabricated using 3D printing of flexible plastics. The rotation of such particles have been measured in previous work (Marcus et al., 2014). If the particle has high enough symmetry and the deformations are small, it rotates just like a sphere (Bretherton, 1962; Harris and Pittman, 1975) and provides a measurement of the vorticity. The deformation of the arms from their equilibrium angles provide a measurement of all elements of the strain rate tensor as long as viscosity dominates inertia so that they stay in the quasi-steady, overdamped regime where the elastic restoring force balances viscous drag from the strain rate.

An advantage of using deformable particles is the ability to extract the velocity gradient with only a single particle. Traditionally, to measure the strain and vorticity of the flow we would need to track several particles in a region of space over which the velocity gradient is uniform, which in complex flows occurs at very small length scales. As a result, a large concentration of tracer particles is required for such measurements. Often these concentrations become so high that it is difficult to image very far from the surface of the flow. Making these measurements with deformable particles could allow access to velocity gradients along particle trajectories in locations where they are currently very difficult to measure.

To test this idea, we have performed two sets of experiments on the deformations of triads formed from three arms in a plane with weak links near the central axis as shown in Fig. 3.2. We first measured the deformation of a triad particle fixed on a low friction axis in a viscous 2D simple shear flow. Here the particle arm deformations are 0.04 radians and we show how to extract the 2D velocity gradient tensor from measured arm deformations. We then performed an experiment with similar triad particles in 3D turbulence in a water tunnel with a grid and active jet array. These triads are larger than the Kolmogorov scale in this flow so they sample a coarse grained velocity gradient. Also, because they are planar they do not respond to all components of the strain rate tensor. But they do allow us to demonstrate that the deformations of 3D printed particles in water can be measured. We show that we can achieve precision on the order of 10^{-4} radians in measured arm orientations which allows us to resolve particle deformations. We also simulated the dynamics of small triads in turbulent velocity gradients from the Johns Hopkins database and found deformations qualitatively similar to those measured.

3.2 Theory

3.2.1 Model of arm deformations due to viscous flow

For small deformations that occur slowly compared with the elastic response time of the particle, the arm deforms until the elastic torque balances the torque applied by the fluid. We will use resistive force theory to determine the fluid torque (Gray and Hancock, 1955). We choose the drag coefficient in the resistive force theory so that the fluid force on a fiber in a uniform flow matches Bachelor's slender body theory (Batchelor, 1970; Roy et al., 2019),

$$\mathbf{F} = 4\pi\mu\mathbf{u}L(\log 2\kappa)^{-1}[(\cos\alpha)\hat{\mathbf{p}} - 2\hat{\mathbf{e}}_{\mathbf{u}}], \tag{3.2}$$

where $\mathbf{u}$, with unit vector $\hat{\mathbf{e}}_{\mathbf{u}}$, is the relative velocity between the fiber and the fluid. The angle between the arm which is defined by the unit vector $\hat{\mathbf{p}}$ and the fluid velocity is α. Using this force, the torque on a differential length of a slender arm, dr, at distance r from the particle center is

$$d\tau = r\hat{\mathbf{p}} \times \frac{8\pi\mu}{\log 2\kappa}\mathbf{u}dr. \tag{3.3}$$

For a particle advected in a flow with uniform velocity gradients, the relative velocity between the fluid and the arm at a point $r\hat{\mathbf{p}}$ from the center is $\mathbf{u} = \mathbf{A}r\hat{\mathbf{p}} - \mathbf{\Omega} \times r\hat{\mathbf{p}}$, where $\mathbf{A}$ is the velocity gradient tensor and $\mathbf{\Omega}$ is the solid body rotation rate of the particle. Using this expression for $\mathbf{u}$, the torque from the fluid is found by integrating Eq. 3.3 along the full length of the arm

$$\tau = \frac{8\pi\mu}{\log 2\kappa}\frac{L^3}{3}[\hat{\mathbf{p}} \times (\mathbf{A}\hat{\mathbf{p}} - \mathbf{\Omega} \times \hat{\mathbf{p}})]. \tag{3.4}$$

This torque from fluid drag is balanced by a restoring elastic torque which acts to bring the triad arm back to its equilibrium position,

$$\frac{8\pi\mu}{\log 2\kappa}\frac{L^3}{3}[\hat{\mathbf{p}} \times (\mathbf{A}\hat{\mathbf{p}} - \mathbf{\Omega} \times \hat{\mathbf{p}})] = k(\hat{\mathbf{p}} \times \Delta\mathbf{p}), \tag{3.5}$$

where k is the torsion coefficient and $\Delta\mathbf{p}$ is the small displacement of the arm from its equilibrium (undeformed) position, $\hat{\mathbf{p}}'$, to its deformed position, $\hat{\mathbf{p}}$.

For a sufficiently small isotropic particle with density equal to the fluid, the particle will rotate with the same rotation rate as the fluid. An example of such an isotropic particle is a tetrad, which is comprised of four cylindrical arms symmetrically oriented with respect to each other so that the particle has an effective ellipsoid which is a sphere. Because the particle rotates with the fluid rotation, the relative velocity between the fluid and an arm of the particle is only due to the strain component of the velocity gradient tensor, reducing the relative velocity to $\mathbf{u} = \mathbf{S}r\hat{\mathbf{p}}$. As such Eq. 3.5 simplifies to

$$\frac{8\pi\mu}{\log 2\kappa}\frac{L^3}{3}(\hat{\mathbf{p}} \times \mathbf{S}\hat{\mathbf{p}}) = k(\hat{\mathbf{p}} \times \Delta\mathbf{p}). \tag{3.6}$$

Now considering a 2D flow, where all arms of the particle are in the plane, the orientation of arm n is $\theta_n + \delta\theta_n$, where θ_n is the angle between the undeformed arm and the x axis (see Fig. 3.1), and $\delta\theta_n = (\hat{\mathbf{p}} \times \Delta\mathbf{p}) \cdot \hat{z}$ is the deformation angle which is assumed to be small. For a simple shear flow with $u_x = \dot{\gamma}y$ and $u_y = 0$, where the particle rotates with the fluid and using Eq. 3.6, the deformations in our 2D flow are

$$\frac{8\pi\mu}{\log 2\kappa}\frac{L^3}{3}\frac{\dot{\gamma}}{2}\cos(2(\theta_n + \delta\theta_n)) = k\delta\theta_n. \tag{3.7}$$

3.2.2 Extracting the strain rate from arm deformations

We want to extract the 8 free parameters in a three-dimensional incompressible velocity gradient tensor from measurements of the rotation and deformation of a particle. If a particle is sufficiently isotropic, it rotates with the fluid vorticity so the measured solid body rotation allows reconstruction of the 3 parameters which are the components of the vorticity vector. From the measured deformation of the arms, we want to extract

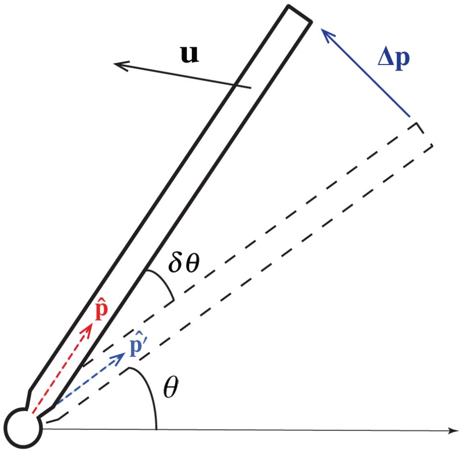

Figure 3.1: A triad arm in its equilibrium position, $\hat{\mathbf{p}}'$, displaced by $\Delta\mathbf{p}$ to its deformed position, $\hat{\mathbf{p}}$, where the perpendicular component of the fluid velocity, $\mathbf{u}$, applies a drag torque on the arm.

the remaining 5 parameters that specify the strain rate tensor. We can measure the two angles that specify the orientation of each of the n arms of a particle providing $2n$ measurements. There are 3 Euler angles needed to specify the orientation of an undeformed particle in space, so the number of arms necessary to determine the 5 remaining parameters is $2n - 3 \geq 5$. Thus we need at least $n = 4$ arms whose deformation from their equilibrium orientation is measured in order to measure the strain rate tensor in a 3D flow. In a symmetric undeformed configuration, these 4 arms would form a tetrad.

In Eq. 3.6, there are three equations for each arm in Cartesian coordinates, and so measurements of the orientations of four arms produces 12 equations with degeneracies. To demonstrate that extracting the strain rate from arm deformations is possible from these equations, we modeled the deformation of a four armed tetrad particle using Eq. 3.6 with a chosen strain rate tensor. The modeled deformation was then input into Eq. 3.6 and we found that singular value decomposition (SVD) returns a unique solution recovering the correct fluid strain rate in 3D flows.

It would appear that by increasing the number of arms of a system we would have an overdetermined system that would provide a more accurate way of determining the strain rate from measured arm deformations with noise. However, a 6 armed particle like a jack is a special case that does not work. Even though a jack is symmetric and rotates with the flow vorticity, it has co-linear arms which in essence turns the arms on the same axis into a single arm. As a result, the jack will effectively have only 3 arms, which is not sufficient to determine the 3D strain rate tensor. Other symmetric configurations of arms that have at least 4 non-co-linear arms would work.

For our experiments in 2D and 3D flows we use triads. The triads have three cylindrical arms in one plane connected to each other at the center of the particle. The arms are separated equally from one another by $2\pi/3$ radians. In a 2D simple shear flow using Eq. 3.7 we are able to find the full velocity gradient tensor using a triad. We chose to use triads in our 3D experiments as an initial step to validate our experimental techniques even though they will not be able to measure the full velocity gradient tensor. The reason for this choice is that they are planar so they are much easier to fabricate on 3D printers, and they can rest on flat surfaces without the highly flexible particles acquiring additional permanent deformations.

3.3 2D experiments

3.3.1 2D experimental setup

Figure 3.2 shows the design for the deformable triads used in our experiments. The deformable triads are 3D printed with a Formlabs printer using their Elastic Resin which has a Shore durometer of 50A. Each triad arm tapers to a smaller diameter at a joint near

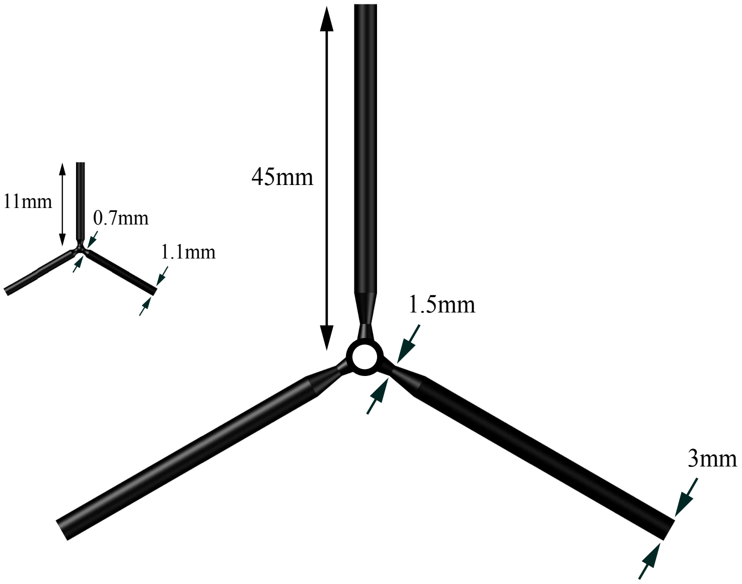

Figure 3.2: The deformable triads used in our experiments. The larger triad with arm length of L = 45 mm and arm diameter of D = 3 mm and joint diameter of 1.5 mm was used in the 2D experiments of simple shear flow. And the smaller triad with arm length of L = 11 mm and arm diameter of D = 1.1 mm and joint diameter of 0.7 mm was used in the 3D turbulence experiments. (The particles are to scale)

the base of the particle. We model the joints as ideal springs, with a linear relationship between torque and arm deformation angle. The joints also have the advantage of localizing particle deformation making image analysis simpler. The triad used in the 2D experiments in a simple shear flow has arms with L = 45 mm and D = 3 mm that go down to either 1.5 mm or 1.0 mm in diameter at the joint.

Simple shear flow is produced by a moving urethane coated polyester belt as shown in Fig. 3.3. The particle is mounted on an air bearing with an axle that extends into the center of the flow. The air bearing allows the particle to freely rotate with the same rate as the fluid vorticity while keeping the particle in a fixed position. As long as the particle is centered where the fluid velocity is zero, fixing its location will not affect its behavior. The fluid used is an aqueous glycerol solution of 90 percent glycerol by

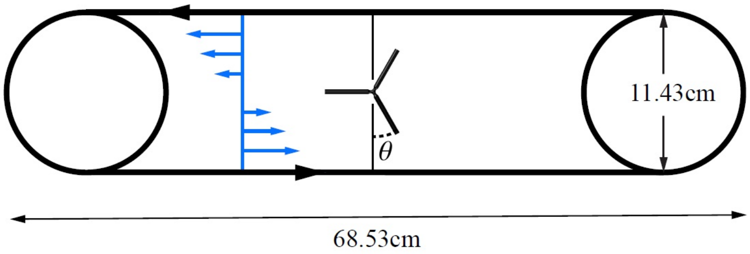

Figure 3.3: Experimental apparatus for the 2D experiments with a simple shear flow created by a moving belt. The particle is suspended in the center of the tank using an air bearing so the particle can rotate at the same rate as the fluid vorticity.

volume, with a measured kinematic viscosity of 193 mm^2/s at a temperature of 19°C. The density of the solution is $1.2 \times 10^3\ \text{kg}/\text{m}^3$ (Segur and Oberstar, 1951; Volk and Kähler, 2018). The belt is driven by an electric motor which allows us to set the strain rate. We use backlighting and a 1 megapixel high speed camera located underneath the glass tank to obtain images like the one shown in Fig. 3.4. The angles of the arms are extracted by performing non-linear fitting of a Gaussian rod model to the measured images (Cole et al., 2016).

We initially examined the deformation of two triads with different joint diameters of 1 mm and 1.5 mm while keeping all the other parameters the same (L = 45 mm and D = 3 mm). The particle rotation rates and deformations were measured for both particle joint diameters at different strain rates of the flow. Figure 3.5a shows the particle rotation rate as a function of fluid strain rate and Fig. 3.5b shows the maximum deformation of the arms as a function of fluid strain rate. The relative deformation between two adjacent arms is sinusoidal in time and here we show the maximum relative deformation calculated by taking half the peak to peak value of the relative arm angles. From Fig. 3.5a we see that at low strain rates both particles experience deformations which are small enough that the particles rotate at the same rate as the fluid. But as the strain rate

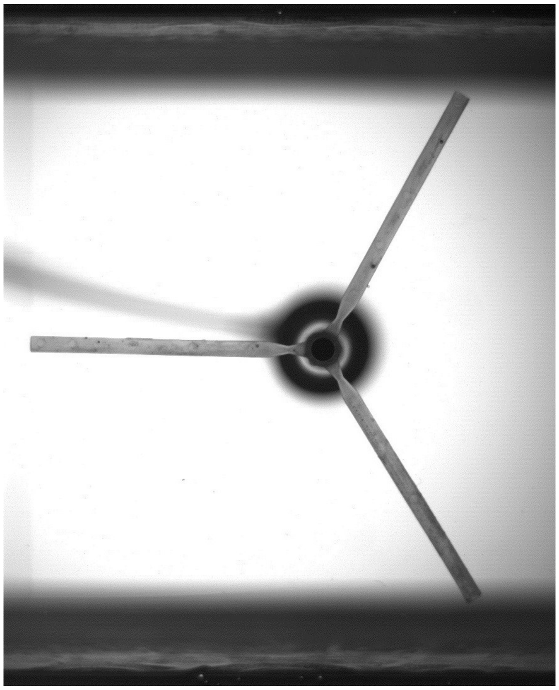

Figure 3.4: Image of a triad in the 2D simple shear flow looking up from the bottom of the flow. The grey areas at the right and left are the belt. The dark center is the shadow of the air bearing and the shaft that holds the particle. The curved grey shadow just above the horizontal arm is the shadow from the air supply tube.

increases and the particles are more deformed, they deviate from being an ideal triad and their effective ellipsoid is no longer a circle. As a result, the particles tumble in Jeffery orbits with an average rotation rate that is smaller than the fluid. The 1.5 mm jointed particle is less deformed than the 1 mm jointed particle at higher strain rates, and so the 1.5 mm jointed particle behaves like an ideal triad for higher strain rates of the flow. Furthermore, Fig. 3.5b shows that the deformation of both particles has a nearly linear relationship with the fluid strain as predicted by Eq. 3.7 up to relative deformations on the order of 0.1 radians. All further experiments in 2D flow were done using the triad with 1.5 mm joints at a strain rate of $\dot{\gamma} = 0.7$ s^{-1} where the maximum relative deformation is about 0.07 radians.

3.3.2 2D results

Figure 3.6 shows the measured angles between pairs of arms as a function of time. Each arm is deformed toward the extensive eigenvectors of the strain rate tensor and away from the compressive eigenvectors, so the there are two maxima and two minima of the relative arm angles for each rotation. The arm separation between arms in an ideal triad is $2\pi/3$ and so the angle differences fluctuate around this value. The angle difference changes by only ± 0.07 radians which means individual arms separated by $2\pi/3$ are deforming by $\pm 0.07/\sqrt{3} = 0.04$ radians indicating the precision required to measure this velocity gradient of $\dot{\gamma}$=0.7 s^{-1} with this particle.

The angle differences between different pairs of arms are slightly different. This is a result of manufacturing non-idealities that make the equilibrium angles and the torsion coefficients of different arms to be slightly different. Figure 3.7 more clearly reveals the differences between different arms by plotting the angle difference as a function of the angle of the trailing arm. Because of these deviations from ideal particles, we calibrate the particle to quantify the variations in equilibrium arm orientation and torsion

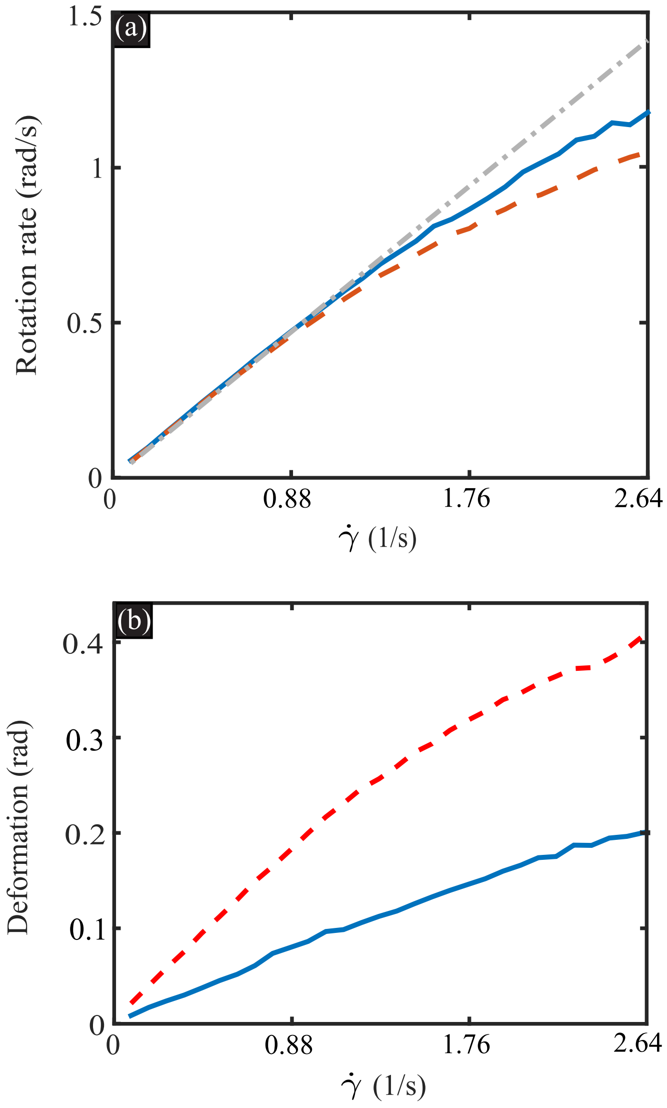

Figure 3.5: (a) The rotation rate and (b) deformation of a triad particle in 2D simple shear flow as a function of fluid strain rate. The red dashed line is for the particle with joint diameter of 1 mm and the blue solid line is for the particle with joint diameter of 1.5 mm. The gray dash-dot line in (a) is the rotation rate for an ideal non deformable particle that always rotates with the same rate as the fluid vorticity. In (b) the deformation is defined as half the peak to peak value of the relative angle between adjacent arms.

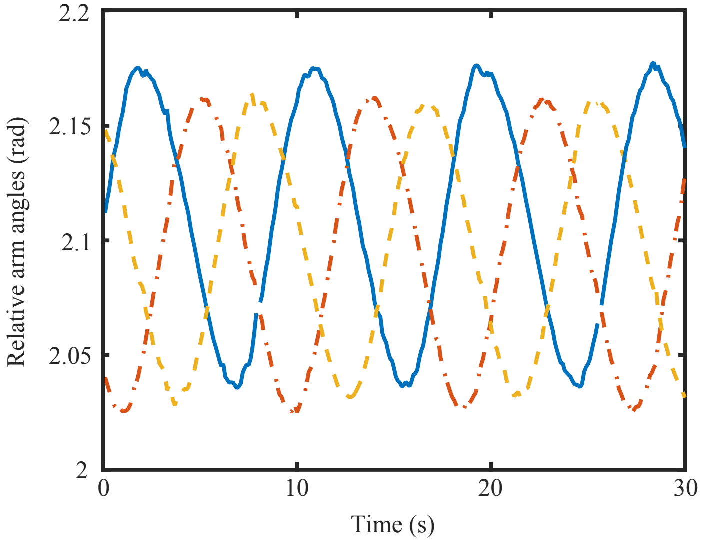

Figure 3.6: Angle between every two neighboring arms as a function of time. For a strain value of $\dot{\gamma} = 0.7$ s^{-1} the angle differences between adjacent arms changes by ±0.07 radians. Each arm experiences a different amount of deformation depending on the particle orientation at a particular time in the flow. Blue solid line is $\Phi_2 - \Phi_1$, red dot-dashed line is $\Phi_3 - \Phi_2$, and yellow dashed line is $\Phi_1 - \Phi_3$.

coefficients.

To calibrate our particle, we extend the theory in Sec. 3.2.1 to include deviations from ideal equilibrium arm orientations, Δ_n, and torsion coefficients, k_n, that are different for each arm. For our non-ideal triad, the instantaneous orientations of the arms indexed by arm number $n = 1, 2, 3$ are

$$\Phi_n = \theta_1 + 2\pi(n-1)/3 + \Delta_n + \delta\theta_n$$

where arm 1 has been chosen as the reference arm so Δ_1 is defined to be zero. Then the expression for the deformation of arm n of a real triad is obtained from Eq. 3.7,

$$\frac{8\pi\mu}{\log 2\kappa}\frac{L^3}{3}\frac{\dot{\gamma}}{2}\cos(2\Phi_n) = k_n\delta\theta_n. \tag{3.8}$$

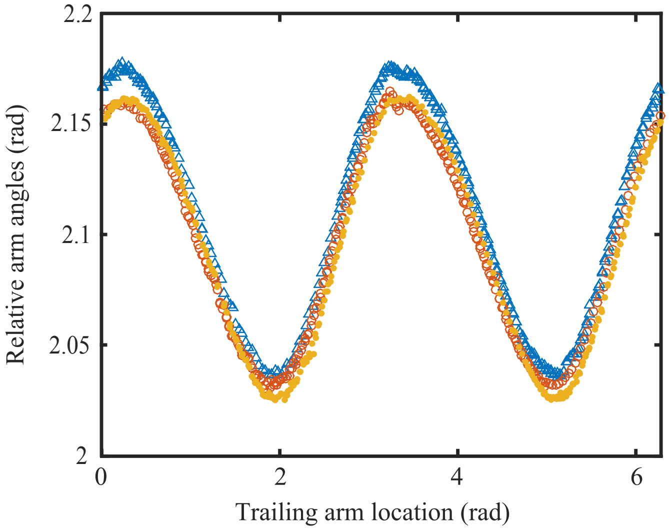

Figure 3.7: The measured angle between a given arm and the arm immediately trailing it as a function of the trailing arms location. Each arm has a unique torsion coefficient that makes the deformation experienced by each arm different. Blue △ shows $\Phi_2 - \Phi_1$, red ○ shows $\Phi_3 - \Phi_2$, and yellow ● shows $\Phi_1 - \Phi_3$.($\dot{\gamma} = 0.7$ s^{-1})

and the angle between arm one and two is

$$\begin{aligned}\Phi_2 - \Phi_1 &= \frac{2\pi}{3} + \Delta_2 \quad ... \\ &+\frac{8\pi\mu}{\log 2\kappa}\frac{L^3}{3}\frac{\dot{\gamma}}{2}\left[\frac{1}{k_2}\cos 2\Phi_2 - \frac{1}{k_1}\cos 2\Phi_1\right]\end{aligned} \tag{3.9}$$

with similar expressions for $\Phi_3 - \Phi_2$ and $\Phi_1 - \Phi_3$.

A non-linear fit of the measured angle differences between all the arms to the model in Eq 3.9 gives best fit parameters $(k_1, k_2, k_3) = (0.27, 0, 25, 0.33) \times 10^{-3}$ N m/rad, and $(\Delta_1, \Delta_2, \Delta_3) = (0, 0.005, 0.002)$ radians. Figure 3.8 shows the fit of the measured arm angle differences between arms 1 and 2. The other angle differences have a similar match to the fit and are not shown. The deviations from an ideal triad are small relative to the total deformation of the particle, but we find that correcting for them is essential to obtain accurate measurements of the instantaneous velocity gradients.

With the particle calibration determined, we are ready to fit for the instantaneous strain rate from measured particle deformations. Here we add an additional parameter ϕ to Eq. 3.9 quantifying the angle of the extensional strain eigenvector with respect to its direction in simple shear. The expression

$$\begin{aligned}\Phi_2 \quad - \quad \Phi_1 = \frac{2\pi}{3} + \Delta_2 \quad ... \\ +\frac{8\pi\mu}{\log 2\kappa}\frac{L^3}{3}\frac{\dot{\gamma}}{2}\left[\frac{1}{k_2}\cos(2\Phi_2 + \phi) - \frac{1}{k_1}\cos(2\Phi_1 + \phi)\right]\end{aligned} \tag{3.10}$$

and the similar expressions for $\Phi_3 - \Phi_2$ and $\Phi_1 - \Phi_3$ can be fit to the instantaneous measurements of Φ_1, Φ_2, and Φ_3 to obtain $\dot{\gamma}$ and ϕ. Figure 3.9(a) shows the measured magnitude of the strain rate deduced from instantaneous particle deformation. The average value matches the actual strain because the particle was calibrated in this flow. The new result here is the demonstration that measurements of the deformation of arms of a particle provides a measurement of the instantaneous strain rate tensor in the flow as long as the particle deformation relaxation time scale is shorter than the time scale

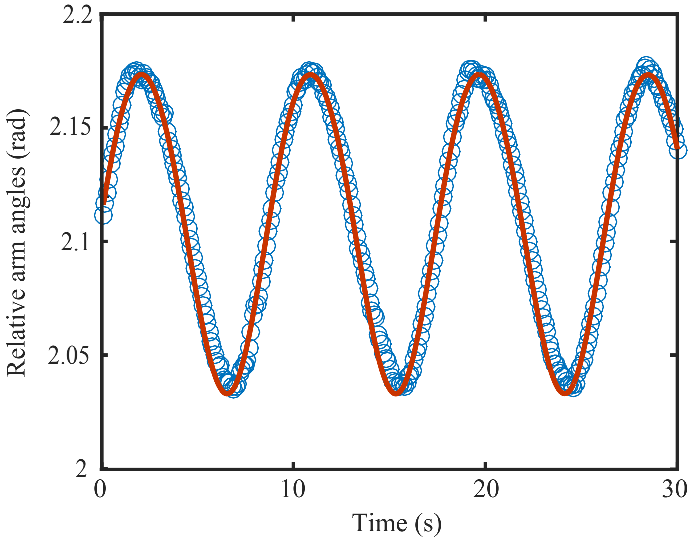

Figure 3.8: Angle between arms 2 and 1, $\Phi_2 - \Phi_1$, as a function of time. The solid red line is the prediction from the model in Eq. 3.9, and the blue circles are measured angles from experiments. ($\dot{\gamma}$ = 0.7 s^{-1})

associated with the velocity gradients. Figure 3.9(b) shows the orientation of the strain rate eigenvectors determined from the particle deformation. The measured orientation is systematically below the expected value of $\pi/4$ by about 0.035 radians or 2.0 degrees, reflecting limitations of alignment of the camera with the simple shear flow. It would be possible to add this as an additional parameter to the particle calibration and potentially improve these measurements.

We also performed an independent but crude calibration of the torsion coefficients of the triad used in the 2D experiments. This was done by hanging weights near the end of an arm and recording the deformation. With this method the torsion coefficient was measured to be $k = 6.4 \times 10^{-4}$ N m/rad. This is a factor of 2 larger than the calibrated values of k_n found from the measured deformation in simple shear flow. This discrepancy is larger than we expected, but may be a consequence of stiffening of the flexible polymer as a result of age and drying. Future use of these methods would likely need to either obtain calibrations in situ or check for changing stiffness of the particles over time.

3.4 3D experiments

3.4.1 3D experimental setup

The 3D experiments on deformable particles were done in a vertical water tunnel with a test section measuring $30 \times 30 \times 150$ cm^3. The vertical water tunnel creates controlled turbulence using a random jet-array that creates approximately homogeneous-isotropic turbulence in the test section. The parameters of the turbulence in our experiments have been interpolated from data obtained from previous measurements of the water tunnel (Kramel, 2018). In these experiments we have a turbulence intensity of $Re_\lambda = 198 \pm 4$ with a mean fluid velocity of 21 ± 3 mm/s, rms fluctuating fluid velocity of 22 mm/s and large-eddy turn over time of 4.5 seconds. The energy dissipation rate of our tunnel for water at room temperature is 108 ± 60 (mm^2/s^3) and the kinematic viscosity is $\nu = 0.91$ mm^2/s. This energy dissipation rate is obtained from the third order Eulerian velocity structure functions. The Kolmogorov length and Kolmogorov time are calculated to be $\eta = 0.28 \pm 0.05$ mm and $\tau_\eta = 0.09$ s. The tunnel is designed so that the through flow counteracts the sedimentation velocity of particles allowing for particles to stay a long time in a fixed detection volume with constant turbulence statistics. The large uncertainty in the energy dissipation rate comes mostly from interpolation because the through flow rate needed to balance the sedimentation of these particles does not match the prior experiments where the energy dissipation rate was measured. Kramel (2018) provides a detailed description of the water tunnel used in these experiments and its working parameters.

The particles used in the 3D experiments are also triads and are shown in Fig. 3.2 with

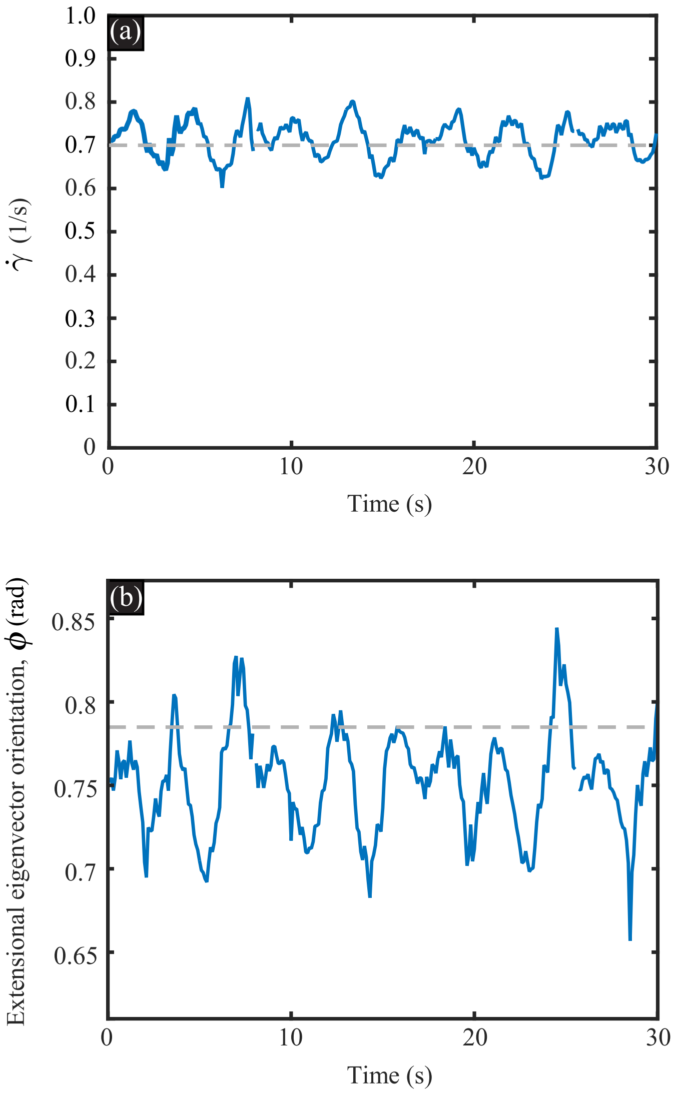

Figure 3.9: (a) Magnitude of the fluid strain where the solid blue line is the calculated value from the model of Eq. 3.7 and the dashed gray line is the known value of $\dot{\gamma} = 0.7\ \mathrm{s}^{-1}$. (b) The orientation of the extensional eigenvector of the fluid strain calculated from Eq. 3.7. We expect the extensional eigenvector to have an orientation of $\pi/4$ in a simple shear flow as shown by the dashed gray line.

$L = 11$ mm and $D = 1.1$ mm which tapers down to a diameter of 0.7 mm at the weak joints. The particles were commercially printed by Rapid Prototype plus Manufacturing LLC (rp+m) using their TangoBlackPlus FLX980 polyjet material. The particle density is approximately 1.12-1.13 g/cm^3 so they settle slowly in water. These triads have a torsion coefficient of $k = 1.3 \times 10^{-5}$ Nm/rad and are made from a polymer with Shore durometer of 26A which converts to a Young's modulus of 0.97 MPa using the relationship derived by Qi et al. (2003). The dimensions of the triads used are limited by the 3D printer resolution and are not as small as the Kolmogorov length scale of our flow, and as a result they could only measure coarse-grained velocity gradients. The bending relaxation time for a thin filament is given by $\tau_b = \mu L^4/EI$ and is 4.5×10^{-4} seconds for our particle (Brouzet et al., 2014; Powers, 2010). The eddy turnover time on the scale of the particle is given by $\tau_{2L} = \sqrt{4/15}\, 2L/u^{\tau}_{2L}$ where $u^{\tau}_{2L} = \sqrt{4/3\, C_2(\varepsilon\, 2L)^{2/3}}$ with $C_2 = 2.0$ (Pope, 2000) is the magnitude of the transverse velocity difference at scale $2L$ of the particle and is 0.52 seconds. Because the bending relaxation time is much less than the time-scales of the turbulence, our particles should always be in the quasi-steady regime where their deformation reflects the instantaneous coarse grained velocity gradient at the particle position.

We track the particles using four high speed Phantom VEO 640S cameras and backlight illumination. Each camera has 72 Gb of RAM and records 1400 frames per second at a resolution of 1600 × 2560 pixels, and so a camera records a total of 12470 frames at full resolution until the internal RAM is filled. After recording, the cameras transfer the recorded data to two data servers for later analysis.

3.4.2 3D results

Using our model of Eq. 3.5 we can calculate expected arm deformations for the experiments done in 3D turbulence. We can estimate the strain rate of the flow from the

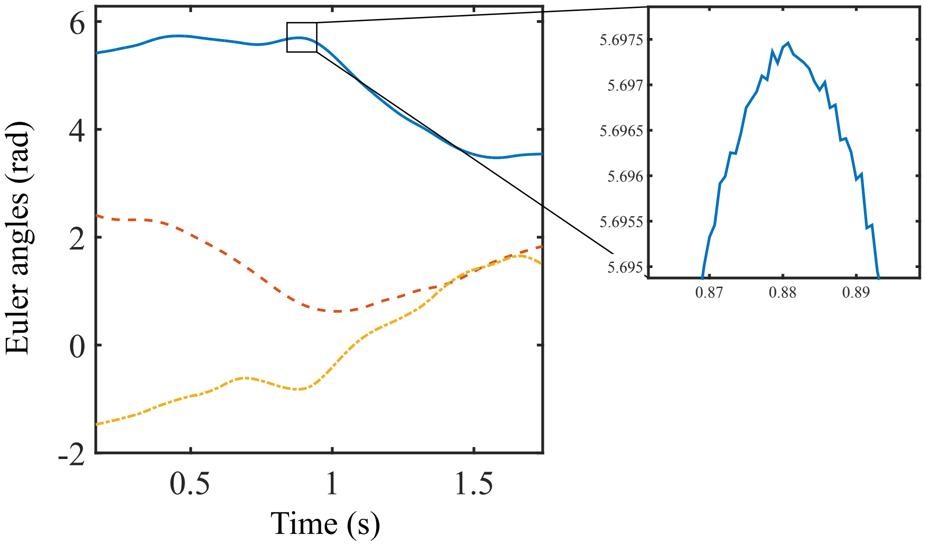

Figure 3.10: The Euler angles giving the particle orientation as a function of time. The expanded view shows the accuracy in obtaining the particle orientations to be on the order of 10^{-4} radians.

energy dissipation rate using $\varepsilon = 15\nu\langle(\partial u/\partial x)^2\rangle$ (Pope, 2000). With these parameters, we calculate that an arm of a triad in velocity gradients at the Kolmogorov scale would deform by approximately 3.5×10^{-4} radians. Since the particles are larger than the Kolmogorov scale, they experience smaller coarse grained velocity gradients and a deformation of 1.2×10^{-4} radians would be expected using the second order velocity structure functions at the scale of the particle.

In order to measure the extremely small deformations experienced by a triad in our flow we require a high level of accuracy in determining the position and orientation of a particle. Fig. 3.10 shows the three Euler angles that determine the orientation of a triad as a function of time. The expanded view of Fig. 3.10 shows the random uncertainty in particle orientations to be on the order of 10^{-4} radians, which is within the same order of magnitude as our predicted deformations. We determine the position and orientation of a triad by using a least squares fitting routine of a modeled triad in three dimensions to the four images of the triad. This high level of accuracy in measuring particle orientations is achieved by creating a model triad that closely resembles the actual triad used in the experiments.

Figure 3.11(a-d) show experimental images of a particle in one frame as seen by all four cameras, with cropping and background subtraction. As we see from the images, the triads used in these experiments are not ideal. The triads are made of soft polymeric materials that naturally have built in strains and imperfections which cause each arm of a particle to have a distinct curvature and shape. Deformation by the fluid still occurs at the weak link, but each arm has a constant equilibrium shape that is not a straight rod. We incorporate the unique curvature and shape of each arm at equilibrium into our model by creating arms that are made up of two separate segments. The overall orientation and shape of each arm is given by 4 angles, 2 of which are associated with the rotation of the whole arm about the base of the particle and 2 are rotations of the second segment of the arm which give an arm its distinct curvature and shape. For this proof of concept experiment, we determined the equilibrium, non-deformed angles for one particle manually. We chose a particle that remained in view for 1.7 seconds and averaged the orientation and shape of each arm through frames selected from the full duration that the particle remained in the detection volume. We then fix the angles that determine the unique shape of a particle in its non-deformed state so we can then accurately measure deformations that occur about this equilibrium state. Fig. 3.11(e-h) show the model particle fitted to the image above it as seen by all four cameras. We could further increase the accuracy of our model by increasing the number of segments that build up an individual arm and thus create a more realistic model, but as is evident by the data and Fig. 3.11, a two segment arm adequately captures the curvature in an arm. This method of determining the non-deformed shape of a single particle may be difficult to extend to experiments where multiple particles are tracked for shorter times.

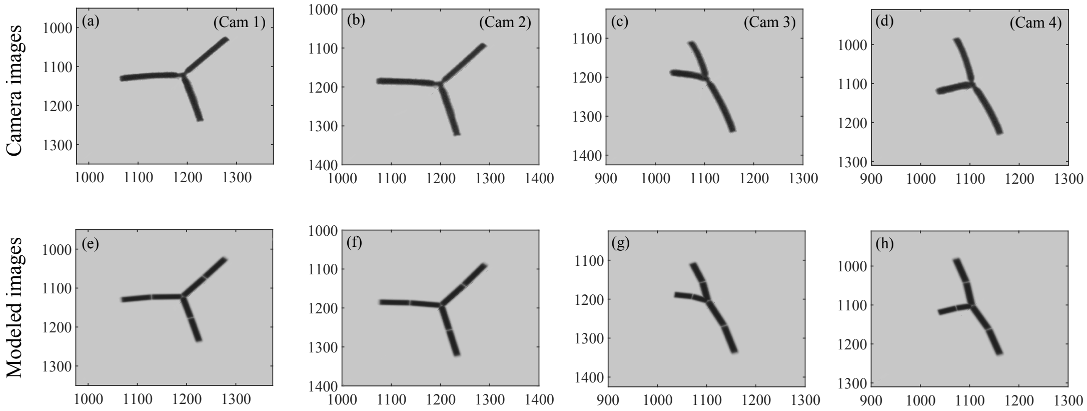

Figure 3.11: Top row: the background subtracted image of a particle in a single frame as seen on all four cameras. Bottom row: the modeled particle fitted to the image at the same instance of time with two segmented arms to capture the natural curvature that exists in the arms of the particle.

In future measurements with this method, we expect that either particles will need to be closer to the ideal symmetric shape or there will need to be ways to identify individual arms of individual particles so the non-deformed shape and torsion coefficients of an individual particle can be used.

Figure 3.12(a) shows the measured deformations for each arm of a triad as a function of time. We can see that each arm is deformed by 0.001-0.002 radians. The measured deformations are close to our predicted value and the orientation measurement accuracy, making it difficult to know if the arms are actually deforming or if the observed deformations are due to noise in our particle orientation measurements. One way to qualitatively evaluate whether the deformations observed in Fig. 3.12(a) are caused by turbulent strain or by measurement errors is to compare with the observed rotation rate of the particle. In turbulence, particle rotation and deformation are both driven by flow structures at the scale of the particle, so we expect turbulence induced deformations to have a correlation time similar to turbulence induced rotations. Fig. 3.12(b) shows the time derivative of $\hat{\mathbf{n}}$ as a function of time, where $\hat{\mathbf{n}}$ is the symmetry axis perpendicular to the plane of the triad. The variations in deformations and rotations have roughly similar time scales. There is shorter time scales in the arm deformation, but a factor of two faster variation in arm deformation than vorticity is possible since strain is a second rank tensor while vorticity is a vector. For example, Fig. 3.7 shows that the deformation has two maxima in each rotation of a particle in simple shear while for typical tumbling motion in 3D turbulence, the components of $\frac{\partial \hat{\mathbf{n}}}{\partial t}$ have only one maximum per period. So we conclude that the measured deformations shown in Fig. 3.12(a) are likely dominated by real deformations caused by the turbulence.

Figure 3.13(a) shows the deformation of the arms of a triad simulated in turbulence from the Johns Hopkins turbulence database (Li et al., 2008; Yu et al., 2012). We simulate the motion of a deformable triad in forced isotropic turbulence on a 1024^3 triply periodic box. The particles are modeled as following a Lagrangian trajectory and rotating and deformaing in response to the velocity gradients along their trajectories. The overall orientation of a triad as it is advected by the flow can be determined using the left Cauchy-Green strain tensor $\mathbf{C}^{(L)}$, which is calculated using the deformation gradient tensor $\mathbf{F}$ (Ni et al., 2014) The eigenvector corresponding to the maximum eigenvalue of $\mathbf{C}^{(L)}$ aligns with the most extensional direction of the fluid stretching, and fibers tend to align themselves with this direction. However, the effective ellipsoid of a triad is a disk and the unit vector along the symmetry axis of a disk aligns with the eigenvector that corresponds to the minimum eigenvalue of $\mathbf{C}^{(L)}$. Thus by calculating the eigenvectors of $\mathbf{C}^{(L)}$ we obtain the orientation of the symmetry axis of a triad at every instance along its trajectory.

We can use $\mathbf{F}$ and $\mathbf{C}^{(L)}$ to solve for the rotation tensor $\mathbf{R}$ which by acting on the triad will account for the rotation of the triad arms in the plane of the triad. With the orientation of the particle and the position of its arms determined, we can now calculate the arm deformations due to fluid strain. We normalize the simulation strains using the eddy

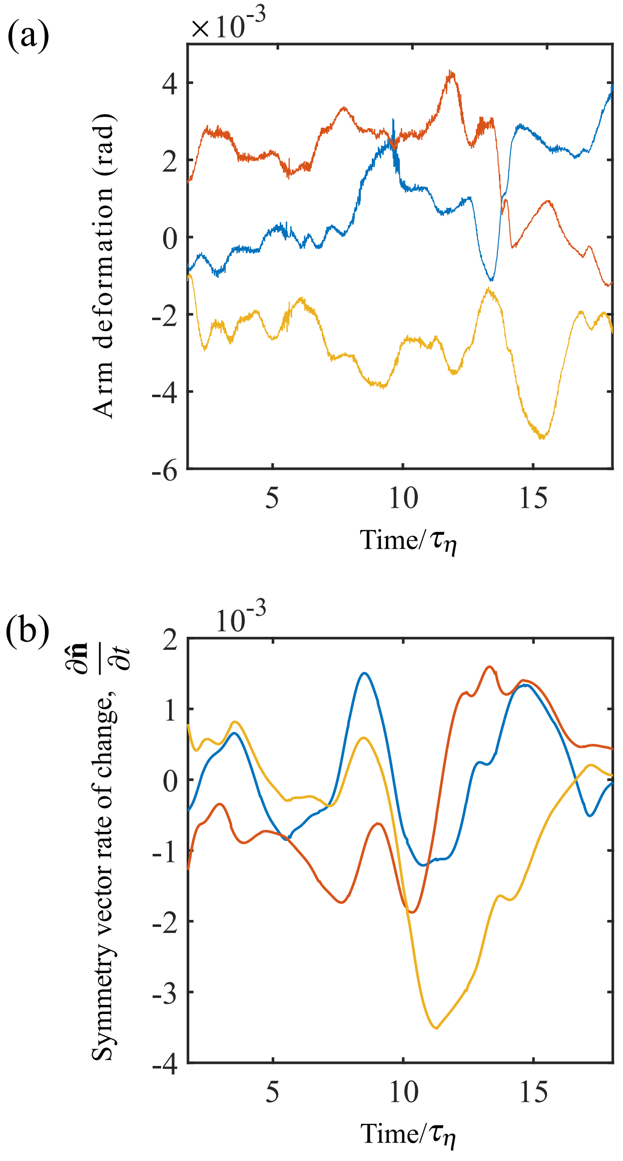

Figure 3.12: (a) Measured deformations for the three arms of a triad as a function of time. Each arm is deformed by 0.001-0.002 radians. (b) x, y, z components of $\partial\hat{\mathbf{n}}/\partial t$ plotted as a function of time for the triad in part (a). $\hat{\mathbf{n}}$ is the unit vector along the symmetry axis perpendicular to the plane of the triad.

turnover time at the scale of the particle τ_L to match our experimental strain values. Since a triad is not an isotropic particle and does not rotate with the same rotation rate as the fluid vorticity, we use the general expression for arm deformations from Eq. 3.5.

Comparing the simulated deformations in Fig. 3.13 with the exprimental deformations in Fig. 3.12, we see that both have the same order of magnitude suggesting that the deformations in Fig 3.12(a) are actual deformation and not measurement noise. The experimental deformations have a somewhat faster time scale which could be simply a feature of this trajectory or it could suggest that some of the measured deformations are non-physical.

The noise that is visible in the simulated data in Fig. 3.13 is due to interpolation difficulties in the database. In those simulations of a 1024^3 periodic box at $R_\lambda = 418$, the grid spacing is 2.19η and so there are often cases where a component of the velocity gradient tensor at neighboring grid points differ by 50% of the rms velocity gradient component. When these velocity gradient fields are interpolated onto Lagrangian trajectories, there are interpolation artifacts of a few percent.

While the 3D turbulence experiments provide evidence of the high level of accuracy that can be achieved in measuring particle position and orientation, we do not observe substantial deformations with the current parameters. Our techniques for measuring velocity gradients from particle deformations are promising, and future work should be able to study more flexible particles in larger strain rates where accurate determination of 3D velocity gradient tensors would be possible.

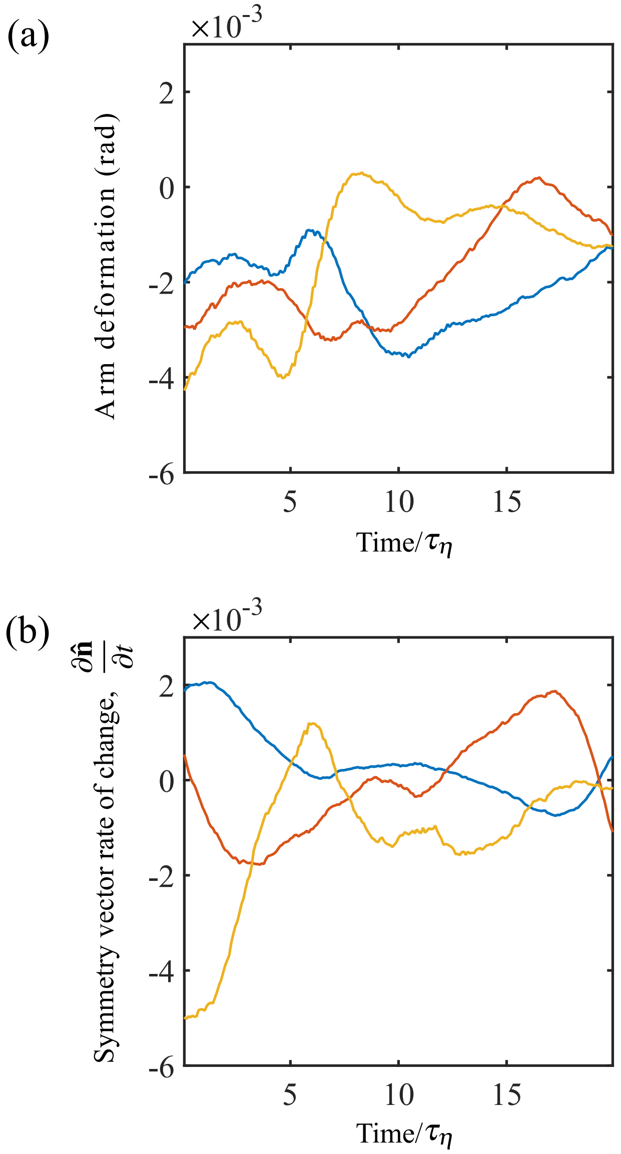

Figure 3.13: (a) Measured deformations for the three arms of a simulated triad in turbulent flow. (b) x, y, z components of $\partial\hat{\mathbf{n}}/\partial t$ plotted as a function of time for the simulated triad in (a).

3.5 Conclusions

Deformable particles exhibit unique responses to the strain and vorticity components of uniform velocity gradient tensors, allowing for the reconstruction of the full velocity gradient tensor from a single particle. Using a triad particle in a 2D simple shear flow, we were able to accurately measure arm deformations and extract the instantaneous velocity gradient tensor from the measurements. Using smaller triad particles in 3D turbulence behind an active jet array, we obtained highly accurate measurements of particle arm orientations on the order of 10^{-4} radians and evidence that we are able to measure arm deformations by the turbulence. We compared our experimental results with simulations of deformable triads which showed similar deformations.

While these measurements are not yet able to measure statistics of particle deformations and velocity gradients in turbulence due to the calibration process required for individual particles, we have demonstrated the potential of this method for future measurements. We anticipate that future work will be able to obtain more flexible particles in the shape of tetrads whose manufacturing variations are minimal. Measurement of such particles in a flow with larger velocity gradients should allow a powerful new way to measure 3D velocity gradient tensors from single particle measurements.

3.6 Appendix

To model the deformation of an arm with a weak link, consider a weak link formed by a short cylindrical segment of the arm of length L_J with $L_J \ll L$ and diameter D_J with $D_J = cD$ and $c < 1$. Our weak links are actually made with more complex shapes as shown in Fig. 3.2 that are simpler to 3D print, but this model is adequate for the scaling argument. If there is negligible bending away from the weak link, the spring constant is determined only by the joint, $k \propto EI_J/L_J \propto ED_J^4/L_J$. Here I_J is the second moment of area of the joint. Using Eq. 3.1 and substituting for k we have

$$\delta\theta \propto \frac{\mu}{E\tau_\eta}\frac{L_J}{c^3 D_J}\frac{L^3}{D^3}. \tag{3.11}$$

So the arm deformation angle is proportional to the third power of the aspect ratio of the arm with a constant of proportionality, $L_J/(c^3 D_J)$ determined by the geometry of the weak link.

For these arms with weak links, the buckling transition is different than for uniform cylinders. However, to demonstrate that we are far from the buckling transition, we simply calculate the diameter of a uniform arm that would have the same spring constant and use the effective diameter to determine the value of Z for our arms. Since our values of Z are more than four orders of magnitude smaller than typical buckling transitions, we know that buckling is not relevant in this case.

3.7 Further experiments in 3D turbulence

3.7.1 Taylor-Couette experiments

In order to achieve larger deformations in our particles we performed experiments in a turbulent conical Taylor-Couette flow. A schematic of the apparatus is shown in Fig. 3.14. We use the same 4 high-speed cameras to obtain full-field imaging of the apparatus through the transparent lid which is a great advantage since we can track particles along their full trajectory. The apparatus is illuminated from below by LED's, allowing for light field imagining. The floor and inner cone of the apparatus rotate and create the Taylor rolls characteristic of Taylor-Couette flows while the outer wall and lid remain stationary.

The advantage of moving to this apparatus is that we can now change the fluid in the apparatus from water to a fluid with a higher dynamic viscosity μ. And from Eq. 3.5

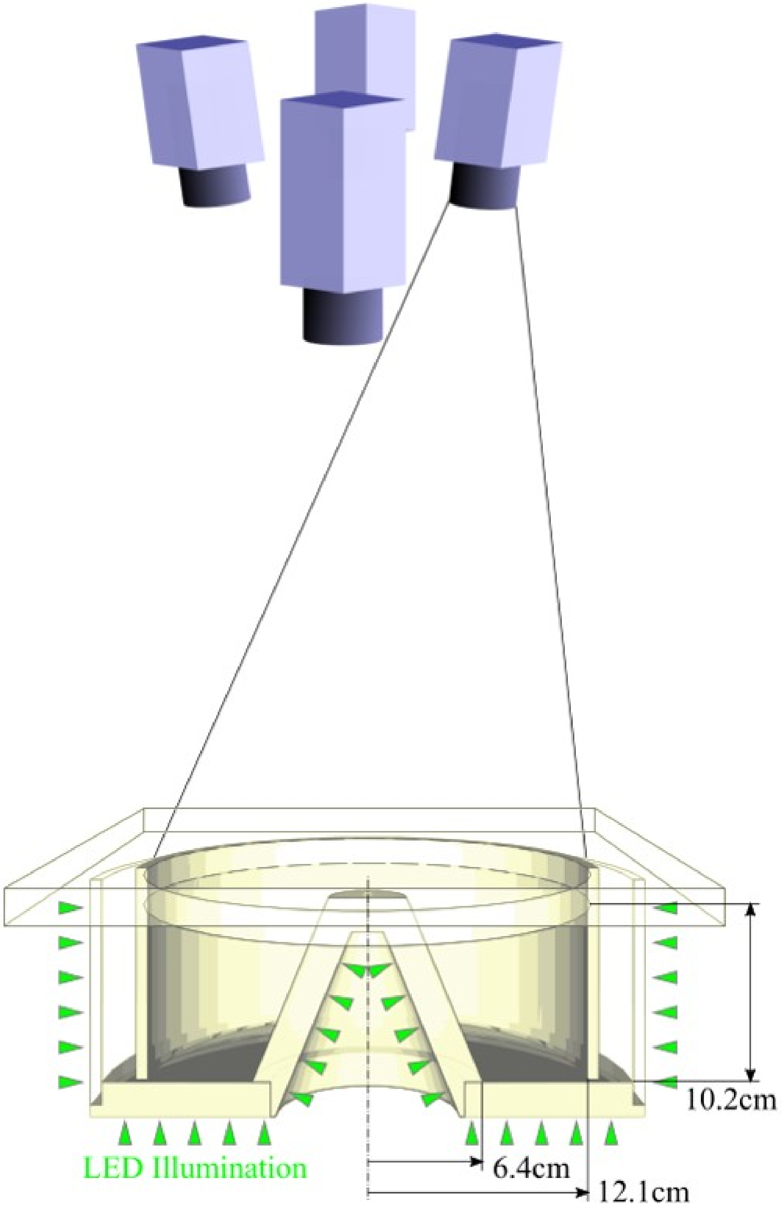

Figure 3.14: Schematic of the cross-section of the conical Taylor-Couette apparatus. The inner cone and floor of the apparatus rotate while the outer wall and transparent lid remain stationary. The apparatus is illuminated from below allowing light-field imaging through the transparent lid. (Figure courtesy of L. Walsh)

we can see that by increasing μ we can increase the torques acting on the arms of the particle which can create larger deformations. The fluid used has been density matched to our particle and is a 69% by weight aqueous glycerol solution at room temperature with kinematic viscosity of $\nu = 15$ mm^2/s and density of $\rho = 1.17 \times 10^3$ kg/m^3.

We use a flexible tetrad shaped particle as pictured in Fig. 3.15. The particle is made of 4 arms that are symmetrically oriented with respect to each other. The arms have an aspect ratio $\kappa = 10$, where the arm length is $L = 10$ mm and arm diameter is $D = 1$ mm with a thinner jointed section near the base of the particle which has a length of 1 mm and diameter of 0.8 mm. The difference between these particles with our previously used flexible triads is that the tetrads are now manufactured using two different polymers with different Shore hardness values as a way to minimize non-idealities. The central blue section is made of a flexible polymer with a Shore hardness value of 26A, while the black arms are made of a rigid polymer keeping the arms straight. The new geometry of the flexible joint section causes the arms to have a lower effective spring constant according to Sec. 3.6. As a result, the new, more flexible particles, along with higher dynamic viscosity fluid, will potentially allow us to achieve higher deformations that are measurable with our system.

We use tracer particles to map the velocity field of the flow. Fig. 3.16 shows the three components of the velocity at 2 Hz rotation rate of the inner wall and floor of the apparatus. The velocity profiles reveal the thin rotating boundary layer at the bottom of the apparatus. Fig. 3.17 also shows an example of a tracer trajectory as it is advected by the flow, demonstrating our ability to track particles for long times.

Figure 3.18 shows the view of the apparatus as seen by the 4 cameras. To minimize optical distortions from oblique viewing through the transparent lid, the cameras are placed close to one-another with small angle separation between them. The small viewing angle between the cameras creates issues in imaging and the ability to precisely locate

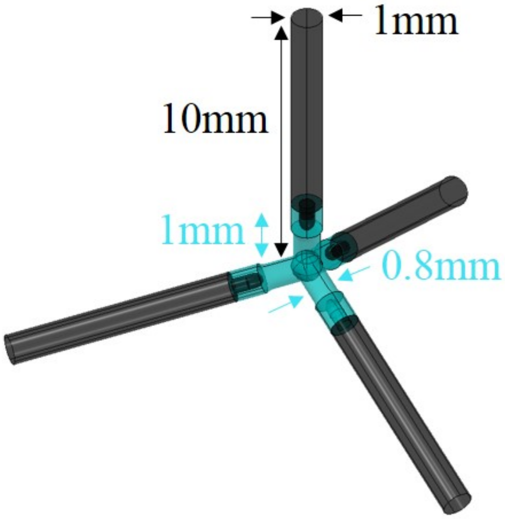

Figure 3.15: The deformable tetrad used in the 3D turbulence experiments with arm length $L = 10$ mm, arm diameter $D = 1$ mm, and thinner jointed section with a length of 1 mm and diameter of 0.8 mm. The tetrad is made up of 2 materials to reduce non-idealities and keep the arms straight. The central blue section is made of a flexible polymer while the black arms are made of a rigid polymer.

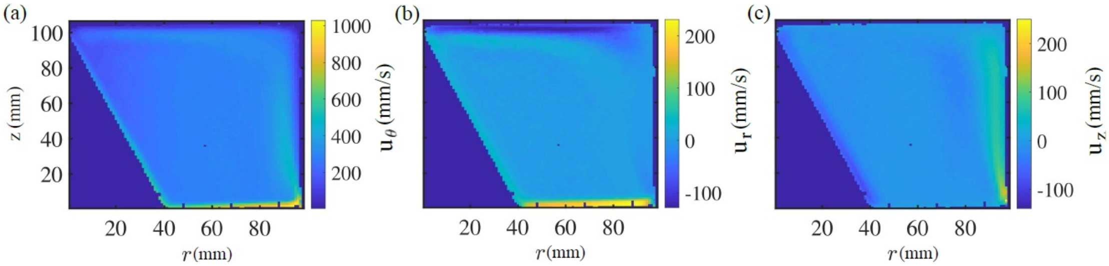

Figure 3.16: Velocity profile of the Taylor-Couette flow at 2 Hz rotation rate of the inner wall and floor of the apparatus. The mean flow is a toroidal roll with large azimuthal and radial velocities in thin boundary layers. (a) The mean azimuthal, (b) mean radial, (c) and mean vertical velocities in a cross section of the flow.

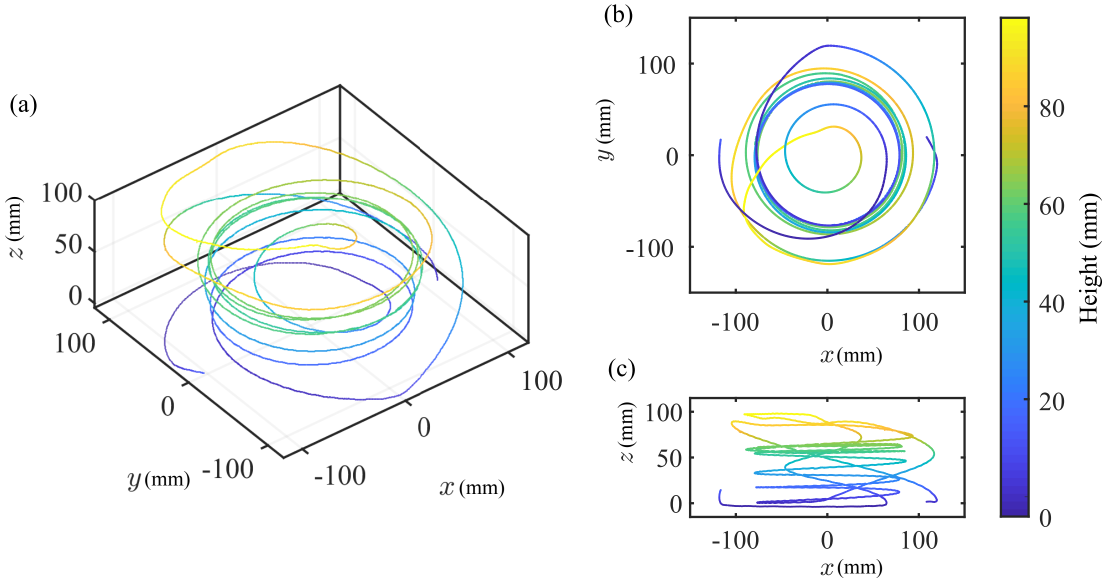

Figure 3.17: One tracer particle trajectory in Taylor-Couette flow shown at three different views. The colorbar indicates the height of the tracer and the trajectory is approximately 18 s long and rotates the apparatus 10 times.

arms that are pointing along the camera axis. If we increase the angle between the cameras by using lower focal length lenses and by lowering the cameras so that we still have full-field imaging of the apparatus, then we introduce optical distortions caused by the increased curvature of the lower focal length lenses and oblique viewing through the plexiglass lid. We implemented higher order distortion terms in our pinhole camera calibration model to correct for these issues but were unable to fully resolve all the effects from distortions. And so we are unable to precisely measure arm positions in this apparatus and are not able to measure the small deformations experienced by the particle. Because of this, we perform additional experiments in the water tunnel with the new more flexible particle at higher turbulence intensities than before to see whether we can observe larger measurable deformations.

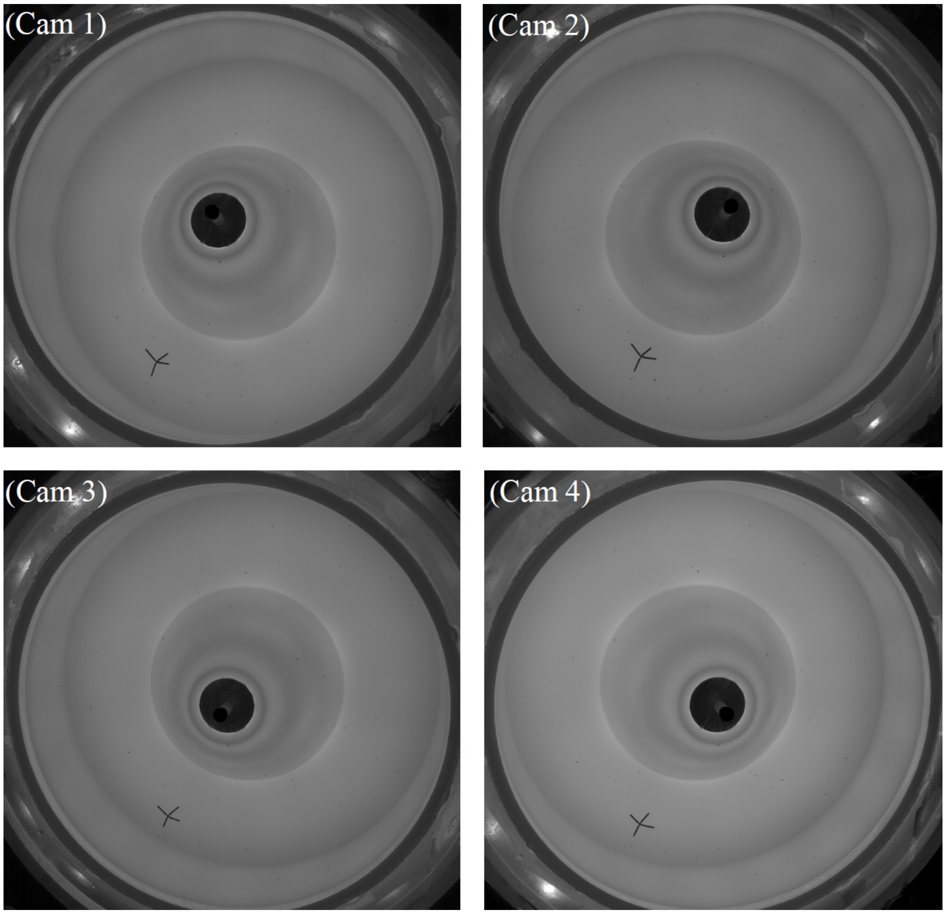

Figure 3.18: Camera view of the Taylor-Couette apparatus as viewed by the 4 cameras showing the full Taylor-Couette flow allowing us to image the tetrad at all times along its trajectory as it is advected by the flow .

3.7.2 Water tunnel experiments

The water tunnel allows for larger viewing angles between the cameras for precise 3D reconstruction of the particle. Additionally, the near perpendicular viewing through the test section significantly reduces optical distortions. Furthermore, we are able to make extremely precise measurements of particle positions and orientations using our refined calibration method which corrects higher order distortion terms in the pinhole camera model.

We perform experiments at two different turbulence intensities in order to compare deformation measurements and be able to determine if the measurements are real or noise from systematic errors. The low turbulence intensity used has the same driving parameters as in Kramel (2018) and has an energy dissipation rate of approximately $\varepsilon = 50\ \mathrm{mm}^2/\mathrm{s}^3$. The high turbulence intensity flow has a higher jet flow than previous experiments and we use tracer particles to determine the energy dissipation rate from calculating the second and third order structure functions. Figure 3.19 shows the energy dissipation rate calculated using the second and third order longitudinal structure functions as a function of tracer separation normalized by the Kolmogorov length, which is approximately $\eta = 0.2$ mm for the high turbulence intensity flow. The second order longitudinal structure function scales as $D_{LL} = C_2\,(\varepsilon r)^{2/3}$ and is valid in the inertial subrange where $C_2 = 2$ (Pope, 2000). The third order longitudinal structure function in the inertial subrange is the Kolmogorov 4/5 law and is given by $D_{LLL} = -4/5\ \varepsilon r$. We use the second order structure function to determine ε since it has less measurement error, as a result $\varepsilon = 480\ \mathrm{mm}^2/\mathrm{s}^3$, indicated by the red dashed line, allowing for a 10% error margin in our measurements.

The inertial subrange, $\eta \ll r \ll L$, for our flow is shown in Fig. 3.20. Here L is the integral lengthscale of the flow. The solid blue line shows the measured value

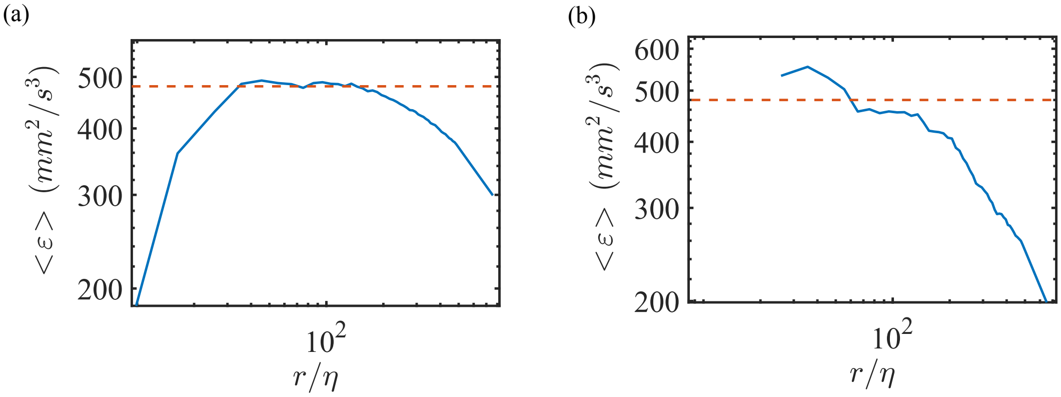

Figure 3.19: (a) Energy dissipation rate calculation using the second order longitudinal structure function, D_{LL} (solid blue line), and (b) energy dissipation rate calculation using the third order longitudinal structure function, D_{LLL} (solid blue line). The dashed red line is for an energy dissipation rate of 480 mm^2/s^3 chosen based off of the energy dissipation calculation using D_{LL} and allowing for 10% error in our measurements.

for D_{LL} at different lengths compared to the theoretical value $D_{LL} = C_2\,(\varepsilon r)^{2/3}$, where $C_2 = 2$ (Pope, 2000) and $\varepsilon = 480$ mm^2/s^3. We can see that for approximately $r = 40\eta$ to 180η our measurements agree with the theoretical value which also corresponds to the plateau of Fig. 3.19 where we chose $\varepsilon = 480$ mm^2/s^3.

We use a similar method to the methods used for finding the position and orientation of deformable triads, as mentioned in Sec. 3.4.2. Fig. 3.21(a-d) show experimental images of a tetrad in one frame as seen by all four cameras, with cropping and background subtraction. Even though the tetrads are made of two different materials to minimize non-idealities, there are still some kinks and bends in the arms where the material transition occurs. Similar to Fig. 3.11 our model has two segmented arms with segments located at the material transition point. Since the rest of the arm is made of a rigid polymer, it is straight and we do not require additional segments along the rest of the arm. In this way we are able to create an extremely precise model of our particle which we can use to fit to our camera images and obtain precise measurements of arm positions.

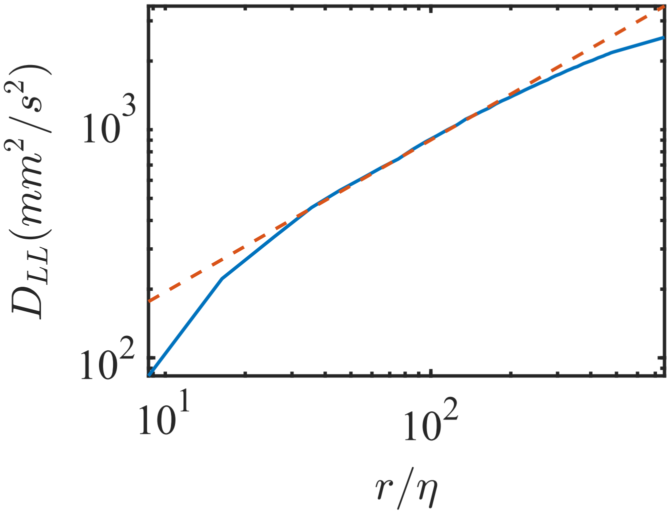

Figure 3.20: Second order longitudinal structure function (solid blue line) compared to the theoretical value for the inertial subrange (dashed red line), $D_{LL} = C_2\,(\varepsilon r)^{2/3}$, where $C_2 = 2$ (Pope, 2000) and ε = 480 mm^2/s^3.

Fig. 3.21(e-h) show the model particle fitted to the image above it as seen by all four cameras and Fig. 3.21(i-l) show the model image subtracted from the camera image to demonstrate the quality of our fitting.

Figure 3.22 shows the relative arm angles between every two neighboring arms of a tetrad as a function of time for low and high turbulence intensities. The energy dissipation rate is proportional to the strain rate of the flow which according to Eq. 3.6 is responsible for deforming the arms of an isotropic particle such as a tetrad. In low turbulence intensity flows we expect less deformation since the energy dissipation rate is low which in turn causes the strains experienced by our particle to be low. But as we see from Fig. 3.22, the measured deformations at low turbulence intensities (ε = 50 mm^2/s^3) and high turbulence intensities (ε = 480 mm^2/s^3) are approximately the same and around 1 to 2 degrees.

These measurements indicate that we are unable to measure the deformations experi-

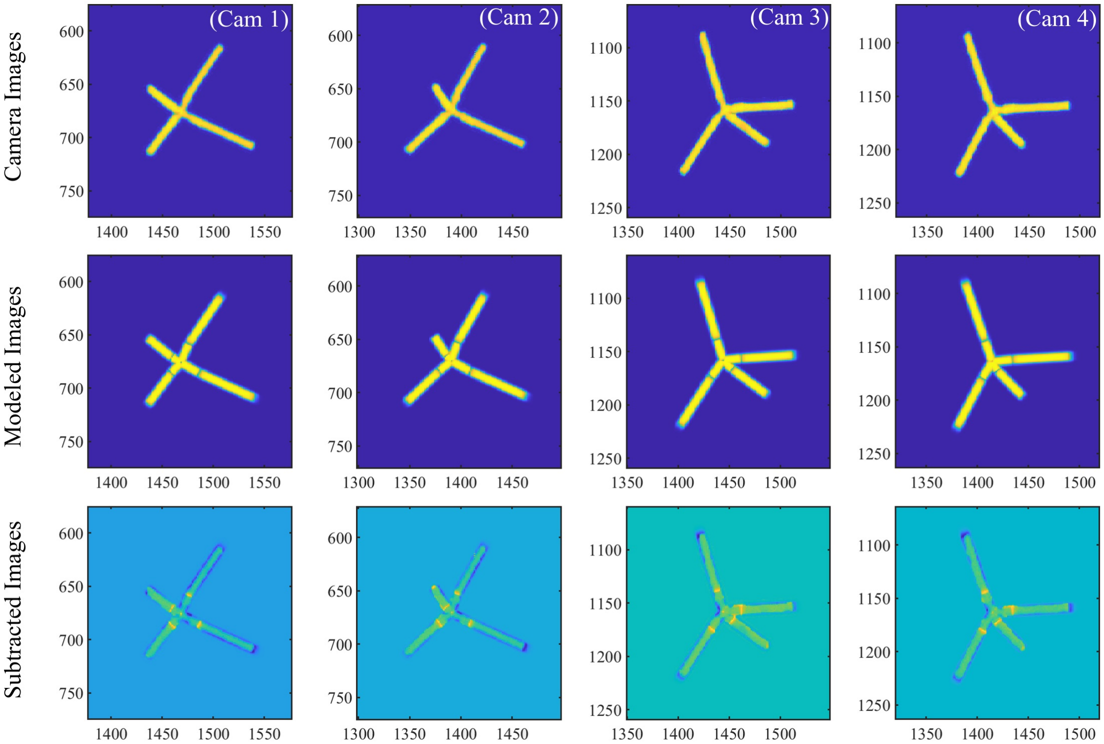

Figure 3.21: (a-d) The background subtracted image of a particle in a single frame as seen on all four cameras. (e-h) The modeled particle fitted to the image at the same instance of time with two segmented arms to capture non-idealities that exists in the particle. (i-l) The model image subtracted from the camera image showing the quality of our fits.

enced by these particle with our current setup and that our measurements are the result of systematic noise. The deformations experienced by the particle are right at the edge of our detection capabilities and future work would require more flexile particles in flows with higher velocity gradients. In the process of precision measurements of particle deformations we have been able to measure particle positions and orientations with high precision which we can use to further study particle dynamics and motion in turbulence. In the next chapter we shall use these measurement techniques to study the angular dynamics of rigid particles in turbulence which are now measurable due to our highly precise experiments.

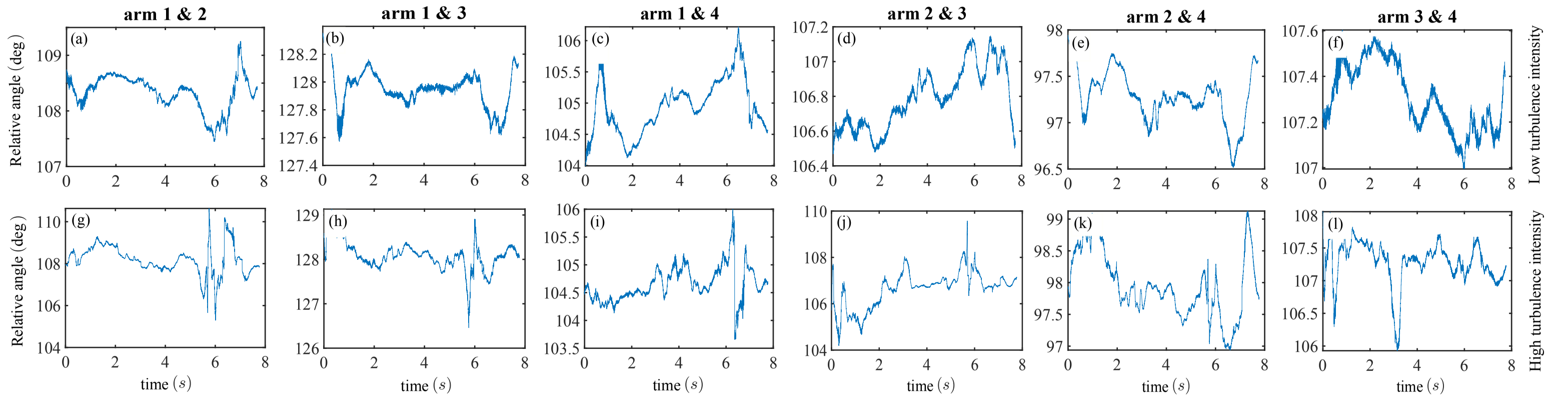

Figure 3.22: Measured deformations for a deformable tetrad. (a-f) The relative arm angles between the four arms of a tetrad for low turbulence intensities of $\varepsilon = 50\text{mm}^2/\text{s}^3$. (g-l) The relative arm angles between the four arms of a tetrad for high turbulence intensities of $\varepsilon = 480\text{mm}^2/\text{s}^3$.

Chapter 4

Angular dynamics of large particles in turbulence

In this chapter we use the experimental techniques we have developed to precisely measure particle positions and orientations to obtain translational and angular velocity and acceleration statistics. We examine the rotational dynamics of large particles in turbulence and how the dynamics depend on particle shape. We also study the alignment of the vectors involved in particle dynamics with one-another under various different conditions.

4.1 Introduction

Particle dynamics and the study of their alignment in fluid flows have long been the focus of fluid dynamics research and is important in a variety of different areas such as the study of plastic transport in the ocean (DiBenedetto et al., 2018). When particles are smaller than the smallest length scales of the flow, the Kolmogorov length η, they behave as tracer particles and are advected with the same velocity as a fluid element and are a useful probe for understanding fluid structures and turbulence statistics. Point-like particle transport and mixing in turbulence have been well studied with measurements of their translational accelerations revealing extreme intermittency of this quantity (La Porta et al., 2001). Tracer particles have also been experimentally used to study vorticity dynamics and its alignments with various quantities in turbulence (Lüthi et al., 2005). More recent work has investigated the irreversibility of turbulence and quantifying it using acceleration measurements of fluid particles (Xu et al., 2014). Xu et al. (2014) show that fluid elements decelerate faster than they accelerate in rare flight-crash events. They quantify this irreversibility using the third moment of the translational power and show that it displays a power law scaling with respect to the Taylor scale Reynolds number.

A natural progression from point-like tracer particles is the study of different shaped particles and their alignment with the flow. The advection and shape dependent alignment of particles is of interest in many flow environments such as ice-crystal dynamics in clouds (Pinsky and Khain, 1998; Saunders et al., 2001; Sherwood et al., 2006) and fiber orientations in the paper-manufacturing industry (Lundell et al., 2011) and the textile industry (Guo et al., 2017) where particle deformations are also important. The rotational dynamics of fibers have been studied in different flows (Marchioli and Soldati, 2013; Parsa et al., 2012; Shin and Koch, 2005) and how they align with the flow (Ni et al., 2014), where it has been shown that fibers tend to align themselves with the extensional and intermediate component of the strain rate tensor, and the most extensional component of the Cauchy-Green strain rate tensor. The rotational dynamics of oblate shaped ellipsoidal particles have also been examined alongside prolate ellipsoids, which have revealed the shape dependence of these dynamics (Gustavsson et al., 2014; Zhao et al., 2015).

It has been shown using DNS results that the particle solid-body rotation rate is almost independent of particle shape for tracer spheroids in Homogeneous isotropic turbulence, while the components of the solid-body rotation rate, tumbling and spinning, are shape dependent (Byron et al., 2015). In contrast, Byron et al. (2015) also show that the rotation rate is shape dependent for tracer spheroids in random flow where there is finite space and time correlations. This shape dependence is a result of differences in the particle tumbling rates while the spinning rates are shape independent. Recent work on the rotational dynamics of large particles have shown that the rotation rate of large fibers scale proportionally to the length of the fiber (Parsa and Voth, 2014). Additionally, work on the dynamics of large inertial particles with aspect ratio close to 1 has shown that the rotation rate of these particles seem to scale with the equivalent diameter of an equal volume sphere (Bordoloi and Variano, 2017; Pujara et al., 2018). Bordoloi and Variano (2017) observe that large low aspect ratio inertial cylinders behave similarly to equal volume spheres in random flow and not like tracer spheroids in turbulence. This suggests that larger particles experience turbulence as a random forcing and do not respond to turbulent structures. Further work by Bounoua et al. (2018) on long fibers in turbulence has shown that a tumbling Stokes number,

$$St_t = \frac{1}{48}\frac{\rho}{\rho_f}\left(\frac{d}{\eta}\right)^{4/3}\left(\frac{d}{L}\right)^{2/3}\left[1+\frac{3}{4}\left(\frac{d}{L}\right)^{2}\right], \tag{4.1}$$

can be used to determine the relevant scaling factors for particle rotation rates. Where ρ and ρ_f are the particle and fluid densities and d and L are the relevant diameter and length of the particle. For small St_t the rotation rate scales proportionally to the length of the fiber $L^{-4/3}$, as shown by Parsa and Voth (2014), and for large St_t inertia effects must be considered and turbulent fluctuations start to be filtered out causing a decrease in particle rotation rates.

With recent advances in Lagrangian particle tracking we are now able to obtain timeresolved measurements of particle orientations allowing us to calculate angular accelerations. The first of such measurements were performed by Zimmermann et al. (2011a,b) where they observe intermittency in the angular acceleration measurements of a large sphere similar to the intermittency observed in the translational acceleration of fluid elements. Mathai et al. (2016) also demonstrate the ability to measure angular accelerations of a large buoyant sphere in turbulence. Despite the large body of work on particle dynamics in turbulence we still do not have a detailed understanding of particle angular accelerations and its relationship with the other various quantities involved in particle dynamics in turbulence.

Here with our recent capabilities in obtaining particle positions and orientations with high precision (Hejazi et al., 2019) we expand upon existing work and study the angular dynamics of large disk-like particles in turbulence and demonstrate capabilities in measuring particle rotation rates and translational and angular accelerations. Similar to previous studies we also see interesting behavior in large particle rotations that are different from the expected tracer spheroids in turbulence result. We show that particle angular acceleration measurements are a key element in understanding particle dynamics. The angular acceleration measurements show that large disks are not randomly aligned in turbulence and that they experience strong alignment with turbulent structures. The particle accelerations are also correlated for a non-zero time that further shows particle dynamics are influenced by turbulent structures at the scale of the particle.

4.2 Experimental setup

We use two different particle shapes in our experiments. The particles are shown in Fig. 4.1 and are planar three-armed particles called triads and four-armed isotropic particles called tetrads. Particles comparable in size to the Kolmogorov scales behave similar to their corresponding ellipsoid where triads behave like disks and tetrads behave like spheres (Bretherton, 1962; Harris and Pittman, 1975), we extend this equivalency to the larger particles used in our experiments. Both particles are made of slender rods with length $l = 10$ mm and diameter $d = 1$ mm which results in a particle diameter of $D = 20$ mm. The particles are commercially printed by Rapid Prototype plus Manufacturing LLC (rp+m) using the Vero Black polyjet material with a density of $\rho = 1.14$ g cm^{-3}. The particle density is close to the density of water and our particles have a tumbling stokes number of approximately $St_t = 0.02$ where particle inertial effects are negligible. Here for our relevant particle dimensions we have taken d to be the particle arm diameter and L to be the particle diameter.

The experiments are performed in a vertical water tunnel with a test section of $30 \times 30 \times 150$ cm^3. The fluid is water at room temperature with kinematic viscosity of $\nu = 0.91$ mm^2/s. We generate controlled turbulence in the tunnel using a random jet-array and have a through flow in the upward $\hat{z}$ direction to oppose the sedimentation velocity of the particles so they are in view of the cameras for longer times with constant turbulence statistics. The cameras image a section that has turbulence intensities with energy dissipation rate $\varepsilon = 480 \pm 10$ mm^{2}s^{-3} and Taylor-scale Reynolds number of approximately $Re_\lambda = 310$, where the Kolmogorov length is $\eta = 0.2$ mm and the Kolmogorov time is $\tau_\eta = 43$ ms. The energy dissipation rate was measured using tracer particle data and the inertial subrange second and third order longitudinal structure functions. The eddy turnover time on the scale of the particle is $\tau_D = L/\sqrt{15 D_{LL}} = 0.29$ s and is calculated using the second order longitudinal structure function at the scale of the particle where the constants are chosen so that τ_D approaches τ_η in the limit $D < \eta$.

We record images using 4 high-speed, high-resolution Phantom VEO 640S cameras recording at 300 frames a second allowing for approximately 55 seconds of continuous recording before the camera RAM is filled and data transfer is initiated. The data reported here consists of 90 recordings of 55 s each that have approximately 5-10 active tracks per frame. The cameras are positioned such that a pair of cameras are viewing the test section at a 90 ° angle from the other pair, allowing particles to be fully visible at all orientations. The particles are made from a black colored polymer and we use LED illumination to backlight the test section for imaging. The lenses used are 100 mm with approximately a $20 \times 20 \times 20$ cm^3 overlapped view of the test section for particle tracking. Particle tracking is then done using a non-liner fitting algorithm to optimize for the particle position and orientation by minimizing the difference between pixel intensities of an ideal image of our particles and the raw camera images (Hejazi et al., 2019).

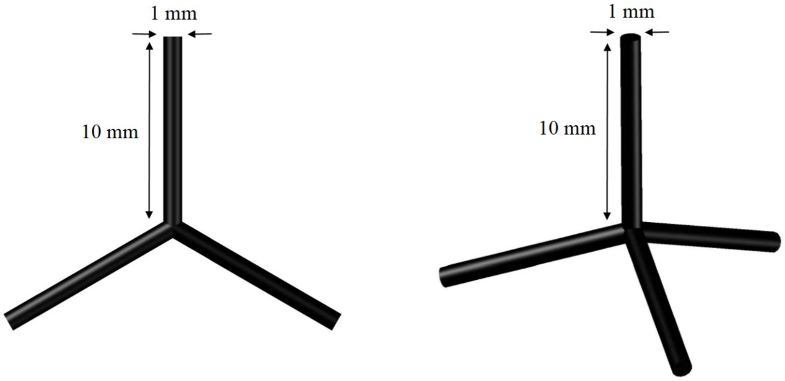

Figure 4.1: The particles used in the experiments are 3 armed triads and 4 armed tetrads. Both particles have arm length $l = 10$ mm and diameter $d = 1$ mm with particle diameter $D = 20$ mm. The triads are planar disk-like particles with arms separated by 120 ° and the tetrads behave like spheres with arms separated by the tetrahedral angle of approximately 109.5 °.

4.3 Results and discussion

4.3.1 Particle velocities and accelerations

We study the angular dynamics of particles by examining the rotation of the particle symmetry axis $\mathbf{p}$. The particle symmetry axis rotates with a solid-body rotation rate $\boldsymbol{\Omega}$ which consists of a tumbling rate, $\dot{\mathbf{p}} = \boldsymbol{\Omega} \times \mathbf{p}$, and spinning rate, $\Omega_p = \boldsymbol{\Omega} \cdot \mathbf{p}$. Fig. 4.2 shows the measured mean square solid body rotation rate $\langle \Omega_i \Omega_i \rangle$ along with its components of mean square tumbling rate $\langle \dot{p}_i \dot{p}_i \rangle$ and spinning rate $\left\langle \Omega_p^2 \right\rangle$ for a triad and tetrad as a function of fit-times normalized by the Kolmogorov time. The solid-body rotation rate of the particles near a plateau at short fit-times, demonstrating our ability in precision measurements of this quantity and its components. At very long fit-times we start to filter out larger rotation rates that occur at shorter time-scales and the mean of the squares start to decrease. From our measurements we are also able to extract the acceleration rate of the symmetry axis. Fig. 4.3 shows the dimensionless mean square translational and angular accelerations as a function of normalized fit-time along with their components along the particle symmetry axis and perpendicular to it. Accelerations are difficult to measure with relatively high measurement noise, as shown for short fit-times where the measurement noise increases the mean square values. The acceleration measurements are less precise than the velocity measurements and an extrapolation method to zero fit-time allows us to determine the accelerations more precisely (Voth et al., 2002b). Table 4.1 shows the measured values of the mean square solid-body rotation rate and its components near the plateau at the shortest fit-time along with the extrapolated values of the mean square accelerations and their components along the particle symmetry axis and perpendicular to it.

Tracer spheroids that are comparable in size to the smallest length-scales of the flow have values of $\langle \Omega_i \Omega_i \rangle$ that is almost shape independent, meaning that disks and spheres

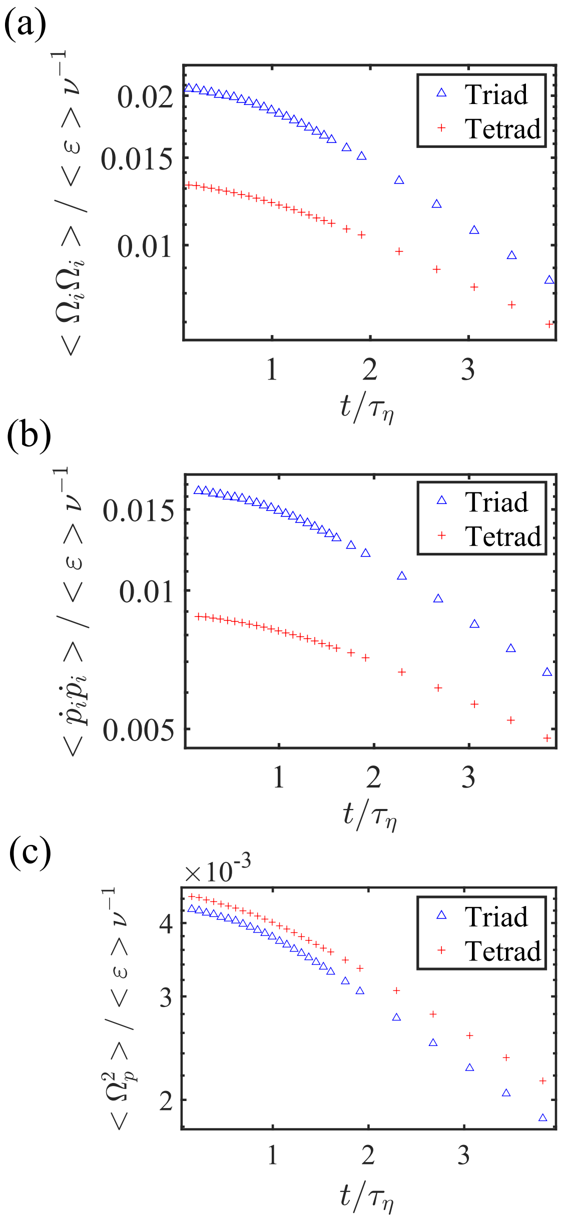

Figure 4.2: (a) Dimensionless mean square particle solid-body rotation rate ($\langle \Omega_i \Omega_i \rangle$), (b) tumbling rate ($\langle \dot{p}_i \dot{p}_i \rangle$), and (c) spinning rate ($\left\langle \Omega_p^2 \right\rangle$) as a function of fit-time in Kolmogorov time units.

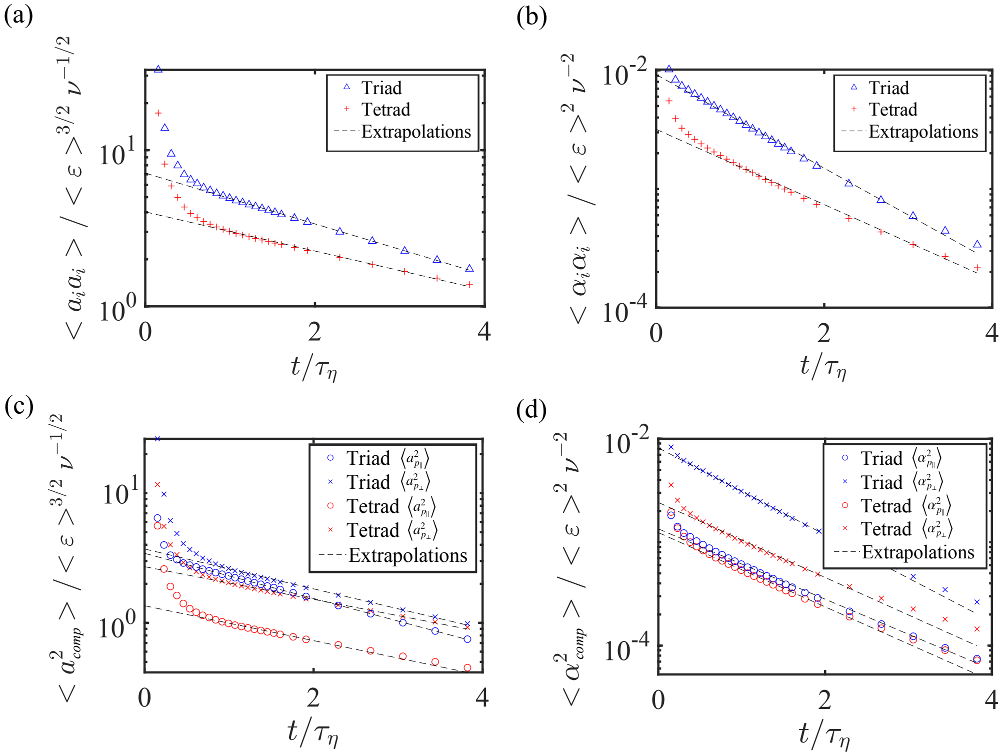

Figure 4.3: Dimensionless mean square particle (a) translational acceleration ($\langle a_i a_i \rangle$) and (b) angular acceleration ($\langle \alpha_i \alpha_i \rangle$) as a function of fit-time in Kolmogorov time units. Dimensionless mean square components of the particle (c) translational acceleration and (d) angular acceleration, along the symmetry axis of the particle and perpendicular to it. We used extrapolations to zero fit-time to obtain a measurement of the mean square accelerations and their components.

Triad

$\langle\Omega_i\Omega_i\rangle$	$\langle\dot{p}_i\dot{p}_i\rangle$	$\left\langle\Omega_p^2\right\rangle$	$\langle a_i a_i\rangle$	$\left\langle a_{p\parallel}^2\right\rangle$	$\left\langle a_{p\perp}^2\right\rangle$	$\langle\alpha_i\alpha_i\rangle$	$\left\langle\alpha_{p\parallel}^2\right\rangle$	$\left\langle\alpha_{p\perp}^2\right\rangle$
0.0208	0.0166	0.0042	7.128	3.435	3.711	0.0092	0.0013	0.0082

Tetrad

$\langle\Omega_i\Omega_i\rangle$	$\langle\dot{p}_i\dot{p}_i\rangle$	$\left\langle\Omega_p^2\right\rangle$	$\langle a_i a_i\rangle$	$\left\langle a_{p\parallel}^2\right\rangle$	$\left\langle a_{p\perp}^2\right\rangle$	$\langle\alpha_i\alpha_i\rangle$	$\left\langle\alpha_{p\parallel}^2\right\rangle$	$\left\langle\alpha_{p\perp}^2\right\rangle$
0.0136	0.0090	0.0045	4.026	1.354	2.710	0.0032	0.0012	0.0024

Table 4.1: The mean square solid-body rotation rate and its components and the translational and angular accelerations with their components along and perpendicular to the particle symmetry axis for large triads and tetrads in turbulence.

experience the same mean square rotation rate (Byron et al., 2015; Voth and Soldati, 2017). From Fig. 4.2 and Table 4.1 we see that the particles studied here do not behave as tracer spheroids in turbulence and the disk-like particles have larger rotation rates. The particles used in our experiments are large and in the inertial subrange. By calculating the second-order longitudinal velocity structure function from data obtained with point-like tracer particles we see that the inertial subrange of our flow is between 40-180η. Our particles have a diameter of $D = 100\eta$ and experience the inertial subrange of the flow.

If we look at the components of $\langle\Omega_i\Omega_i\rangle$ for our large particles, we see that $\left\langle\Omega_p^2\right\rangle$ is almost equal for both particles and appears to be independent of particle shape, while the disk-like particles have a larger tumbling rate. Tracer spheroids randomly oriented in turbulence also show similar behavior where the particle spinning rate is not shape dependent and the tumbling rate is larger for oblate particles. In Fig. 4.4 we show the portion of particle rotation that is due to tumbling (blue), given by $R = \langle\dot{p}_i\dot{p}_i\rangle / \langle\Omega_i\Omega_i\rangle$, and the portion of particle rotation that is due to spinning (red), $R = \left\langle\Omega_p^2\right\rangle / \langle\Omega_i\Omega_i\rangle$. Fig. 4.4 shows the data for our large particles along with the theoretical prediction for tracers in turbulence (Byron et al., 2015) and tracers randomly aligned in turbulence (Parsa and Voth, 2014). Since tetrad and sphere alignments are not influenced by turbulent structures, they have the same contributions to their rotation rate from spinning and tumbling in both turbulent and random flow. On the other hand, triads and disks align with turbulent structures and as a result experience higher relative tumbling rates in turbulence as compared to if randomly oriented. The large triads in our experiments appear to behave as randomly oriented disks with signs of weak alignment.

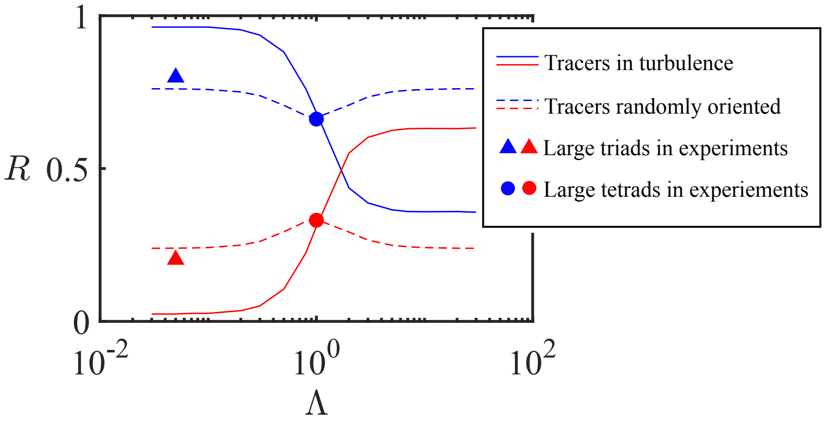

Figure 4.4: The ratio of particle rotation rate components to the total rotation rate as a function of particle aspect ratio Λ for tracer spheroids in turbulence, tracer spheroids randomly oriented in turbulence, and large particles used in our experiments. The color blue represents the portion of particle rotations from tumbling, $R = \langle \dot{p}_i \dot{p}_i \rangle / \langle \Omega_i \Omega_i \rangle$, and the color red represents the portion of particle rotations from spinning, $R = \left\langle \Omega_p^2 \right\rangle / \langle \Omega_i \Omega_i \rangle$.

Bordoloi and Variano (2017) also observe similar behavior in the rotations of large low aspect ratio ($\Lambda = 4$) inertial cylinders. They report that their particle behaves as an equal volume sphere in random flow and not as a prolate particle in turbulence. Their observation that large particles behave as an equal volume sphere is appropriate for particles that have aspect ratio close to 1 where they can be approximated as spheres. The sphere equivalency cannot be made for particles with much higher or lower values of Λ (i.e. $\Lambda >> 1$ or $\Lambda << 1$) where particle dimensions are only a few Kolmogorov lengths. To demonstrate this, we calculate the equivalent sphere volume of the large triads used in our experiments using the volume of a disk with the same dimensions and not by calculating the volume of the plastic arms. The large triads used in our experiments have an equivalent volume sphere diameter of $D_{eq} = 8.4$ mm which results in a ratio of tetrad diameter to equivalent triad diameter of $D_{tetrad}/D_{eq} = 20/8.4 = 2.38$. The equivalent diameter ratio suggests that the different particle shapes are effectively experiencing different flow scales. Alternatively, in the inertial subrange the mean square translational acceleration scales with the particle diameter according to $\langle a_i a_i \rangle \propto D^{-2/3}$ (Volk et al., 2011). We can use the translational acceleration of the two particles to obtain an effective sphere diameter for the large triad. The ratio of $\langle a_i a_i \rangle$ for a tetrad and triad is 0.56 which produces an effective diameter ratio for the particles of $D_{tetrad}/D_{triad} = 0.56^{-3/2} = 2.38$, meaning that with this scaling argument the triad has the dynamics of a spherical particle that has a diameter 2.38 times smaller than the tetrads used in these experiments. The diameter ratio found using the particle translational acceleration scaling is in agreement with the equivalent volume sphere scaling of Bordoloi and Variano (2017).

However the apparent agreement between the two scaling arguments is misleading. The large triads seemingly have their spinning component coupled to smaller scales on the same scale as the arm/disk thickness while the tumbling rate is coupled to larger scales on the scale of the particle diameter. To find the scaling factor between particle rotation rates and their effective diameters we use the eddy-turnover time at the scale of the particle, τ_D, which results in the scaling $\langle \Omega_i \Omega_i \rangle \propto \tau_D^{-2} \propto D^{-4/3}$. Since the particles have the same particle diameter of $D = 20$ mm, they experience the same fluid scales for their tumbling components, and the spinning rate is the component that is scaling with respect to the effective particle diameter. Using the value we found for the ratio of effective diameters, we find that particles with an effective diameter ratio of 2.38

have an almost 1/3 relationship between their spinning rates. But as can be seen in Fig. 4.2(c), the spinning rate is approximately equal for both particles. And thus, the equivalent diameter scaling is not fully capturing the particle dynamics.

As with the solid body rotation we see that the translational and angular accelerations have larger values for the triad as compared to the tetrad. The difference in particle accelerations between the two particle shapes show that the particles do indeed couple differently to the flow. Since a tetrad is isotropic, we expect the velocity and acceleration components along **p** to contribute 1/3 to the total values and the components perpendicular to **p** to contribute to the other 2/3. And as we can see from Table 4.1, the ratio of spinning rate to tumbling rate, and accelerations parallel to and perpendicular to **p** for a tetrad have the expected 0.5 ratio. On the other hand, a triad has values for the angular acceleration components that do not agree with the assumption that particle spinning rates experience smaller scales than the tumbling rate. The triad has a significantly larger contribution from $\left\langle \alpha_{p_\perp}^2 \right\rangle$ that is almost 6 times larger than $\left\langle \alpha_{p_\parallel}^2 \right\rangle$. Whereas, if the spinning rate was experiencing smaller scales we would expect larger contributions from $\left\langle \alpha_{p_\parallel}^2 \right\rangle$. The acceleration components show that large triads experience strong alignment with turbulent structures that intensify their tumbling and have higher spinning rates that are not a result of the particle sampling different scales of the flow. The insight into particle dynamics obtained from angular acceleration measurements highlights the importance of this quantity and how it can help resolve particle dynamics in more detail. The particle angular accelerations reveal information about the preferential alignment of large particles with turbulent structures that cannot be observed by solely studying the particle rotation rates.

Figure 4.5 shows the auto-correlation of the component and magnitude of the various quantities involved in the particle dynamics for both a triad and tetrad. Here the correlation time is normalized by the eddy turn-over time on the scale of the particle τ_D.

From Fig. 4.5(a) we see that the solid-body rotation rate for triads remain correlated for shorter times as compared to tetrads, further suggesting the shape dependence of this quantity. We use the same normalization factor of τ_D as Parsa and Voth (2014) and the auto-correlations for $\dot{\mathbf{p}}$ (Fig. 4.5(b)) become uncorrelated at approximately the same time as the measurements made by Parsa and Voth (2014) for large fibers in turbulence. The observation that triad alignment is influenced by turbulent structures can also be seen by examining the auto-correlation of particle accelerations in Fig. 4.5(c-d). The particle accelerations remain correlated for a non-zero time showing that the particle dynamics are influenced by turbulent structures at the scale of the particle.

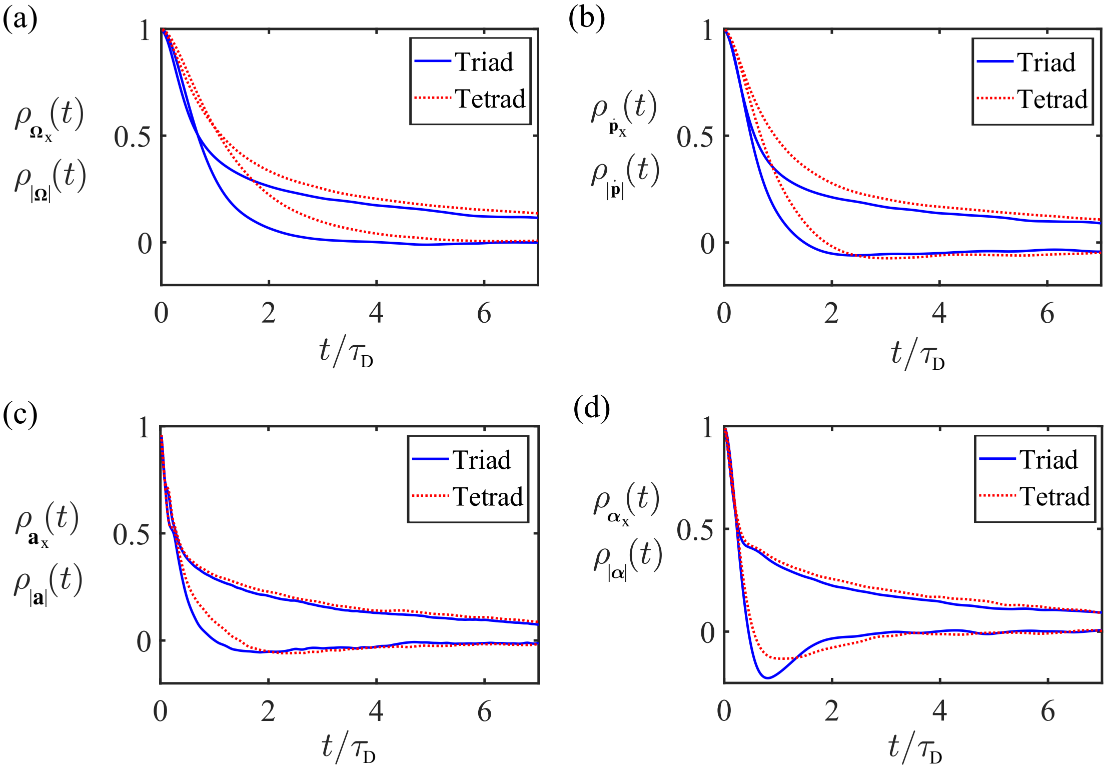

Figure 4.5: The auto-correlation of (a) $\mathbf{\Omega}_x$ and $|\mathbf{\Omega}|$, (b) $\dot{\mathbf{p}}_x$ and $|\dot{\mathbf{p}}|$, (c) $\mathbf{a}_x$ and $|\mathbf{a}|$, (d) $\boldsymbol{\alpha}_x$ and $|\boldsymbol{\alpha}|$. Upper curves are the component auto-correlation and the lower curves are the magnitude auto-correlation.

Measurement error

In order to have reliable measurements of translational and angular velocities and accelerations, we need to identify the noise in our measurements that are introduced in the position and orientation finding stage. Fig. 4.6 shows the dimensionless mean square solid-body rotation rate and acceleration as a function of normalized fit-time for different filters applied to the data of a triad for 10 runs. The filter is applied to the residual of the function that optimizes the rotation matrices used to find the solid-body rotation rate of our particles. Data points that have a residual above the threshold values are filtered out. The residual threshold is fit-time dependent as shown in Fig. 4.6 where three of the applied filters are dependent on the fit-time h. However, the extrapolations to zero fit-time for all thresholds converge to a constant value and the comparison between the extrapolations with different thresholds allows us to see what kind of systematic errors might exist in our measurements. There is an approximate 1.5% difference between the two extreme values for $\langle \Omega_i \Omega_i \rangle$ and 12% for $\langle \alpha_i \alpha_i \rangle$. We choose $3.7h \times 10^{-2}$ as a reasonable threshold for the cuts on the data. We also look at the quality of fits to the positions of a triad used to obtain the translational velocity and acceleration. Fig. 4.7 shows the filters applied to the data in this way and its effect on $\langle a_i a_i \rangle$ of a triad for 10 runs. The mean of this quantity for a fit-time of $t/\tau_\eta = 0.53$ is 1.4×10^{-3} and as we can see from Fig. 4.7, The threshold of 0.01 is close to the mean value and filters out a large portion of the data and reduces the measured value from its true value. And the threshold at 1 is too high and does not adequately filter out the noise in our measurements. We chose 0.1 as a reasonable threshold for this translational fit quality.

4.3.2 Particle alignments

The alignment of the translational and angular vectors with each other and the particle symmetry axis **p** is also of interest and can offer further insight into particle dynamics.

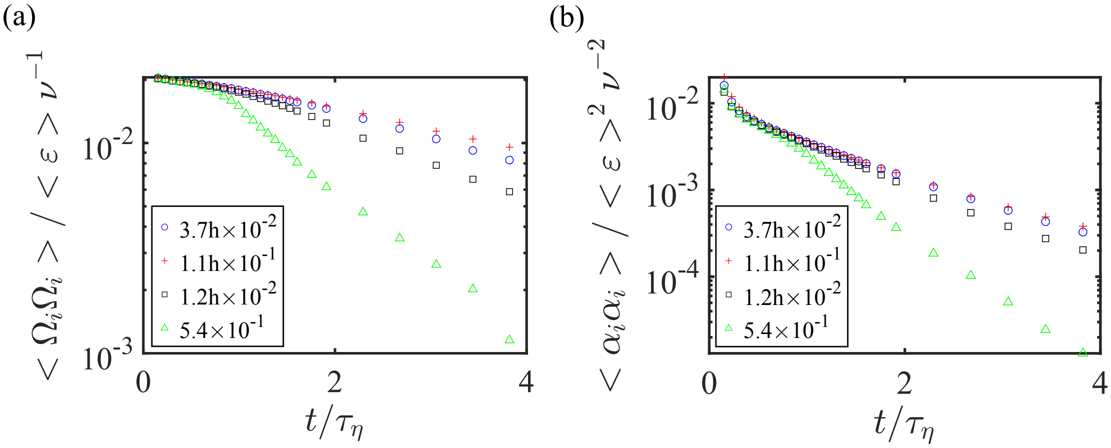

Figure 4.6: Filters on the particle orientation fit quality used to obtain the solid-body rotation rate of a triad and its effect on the dimensionless (a) mean square solid-body rotation rate and (b) mean square angular acceleration as a function of normalized fit-time. The filters are dependent on the fit-time *h* but extrapolate to approximately a constant value.

Fig. 4.8 shows the PDF of the cosine of the angle between the vectors involved in the particle dynamics for both triads and tetrads. Since a tetrad is isotropic, its symmetry axis lies on one of its 4 arms with no preferential alignment, as can be seen by the nearly uniform 0.5 value of the PDF's of a tetrad for the normalized dot product of **p** with the other vectors in Fig. 4.8(a-c). While a triad has strong alignment statistics, where **p** is preferentially perpendicular to $\boldsymbol{\Omega}$ and $\boldsymbol{\alpha}$, demonstrating how a triad predominantly tumbles in turbulent flow. We can also examine the alignment statistics quantitatively by looking at the second moment of the dot product as shown in Table 4.2. The values in Table 4.2 reflect the same behavior as seen in Fig. 4.8 where a value close to 0.3 shows no preferential alignment as is the case for the dot product between **p** and the other vectors for a tetrad. Values less than 0.3 show the preferential perpendicularity of the two vectors and values larger than 0.3 show vectors that are preferentially parallel to each other.

We also examine the alignment of the various quantities of interest in correlation to rare

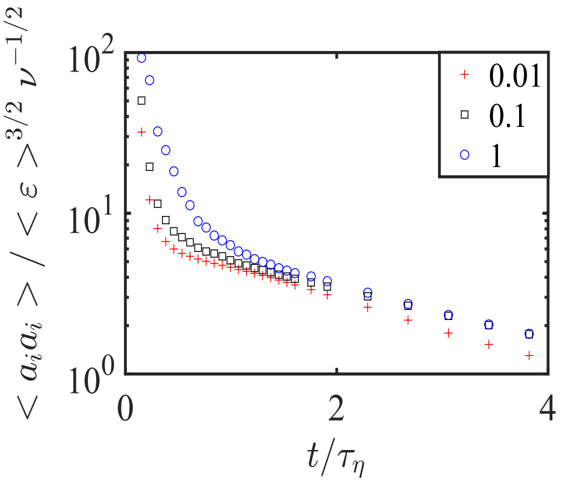

Figure 4.7: Filters on the particle translational fit quality used to obtain the translational velocity and acceleration of a triad and its effect on the dimensionless mean square translational acceleration as a function of normalized fit-time.

events. Table 4.3 shows the alignment value of the vectors at extreme events where we use the relation

$$Al = \frac{\left\langle (\psi \cdot \varphi)^2 \xi^2 \right\rangle}{\left\langle (\psi \cdot \varphi)^2 \right\rangle \left\langle \xi^2 \right\rangle} , \tag{4.2}$$

to obtain information about the alignment of the quantities with one another. Here *Al* is defined by the dot product between the two vectors of interest $\psi \cdot \varphi$ and its correlation

Triad

$\left\langle (\mathbf{p} \cdot \mathbf{\Omega})^2 \right\rangle$	$\left\langle (\mathbf{p} \cdot \mathbf{a})^2 \right\rangle$	$\left\langle (\mathbf{p} \cdot \boldsymbol{\alpha})^2 \right\rangle$	$\left\langle (\mathbf{a} \cdot \mathbf{\Omega})^2 \right\rangle$	$\left\langle (\boldsymbol{\alpha} \cdot \mathbf{\Omega})^2 \right\rangle$	$\left\langle (\mathbf{a} \cdot \boldsymbol{\alpha})^2 \right\rangle$
0.242 ± 0.0010	0.415 ± 0.0005	0.212 ± 0.0005	0.275 ± 0.0005	0.365 ± 0.0011	0.294 ± 0.0003

Tetrad

$\left\langle (\mathbf{p} \cdot \mathbf{\Omega})^2 \right\rangle$	$\left\langle (\mathbf{p} \cdot \mathbf{a})^2 \right\rangle$	$\left\langle (\mathbf{p} \cdot \boldsymbol{\alpha})^2 \right\rangle$	$\left\langle (\mathbf{a} \cdot \mathbf{\Omega})^2 \right\rangle$	$\left\langle (\boldsymbol{\alpha} \cdot \mathbf{\Omega})^2 \right\rangle$	$\left\langle (\mathbf{a} \cdot \boldsymbol{\alpha})^2 \right\rangle$
0.333 ± 0.0022	0.329 ± 0.0016	0.342 ± 0.0008	0.297 ± 0.0013	0.347 ± 0.0005	0.312 ± 0.0005

Table 4.2: The mean square dot product between the vectors involved in particle dynamics for triads and tetrads.

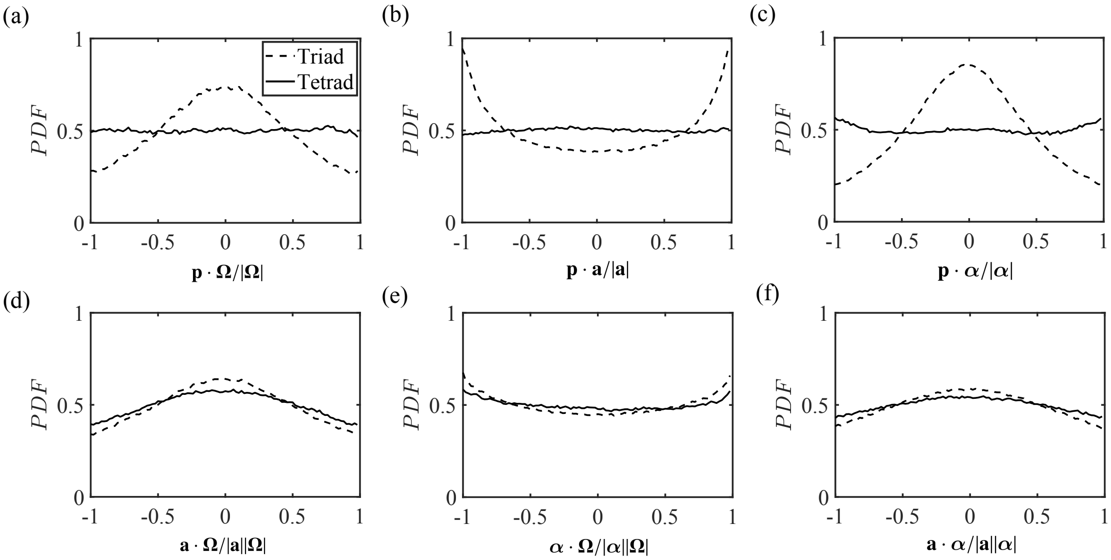

Figure 4.8: PDF of the cosine of the angle between the vectors involved in particle dynamics for a triad (dashed line) and tetrad (solid line)

to the quantity $\boldsymbol{\xi}$. To obtain standard errors for the calculations we divide the data into 8 sub-samples and calculate the second moment of the dot products and Al values for each sub-sample.

The alignment value $Al = 1$ when the alignment between two vectors does not change during events $\boldsymbol{\xi}$. For example, since the symmetry axis of a tetrad has no preferential orientation, this random alignment does not change during rare events and $Al \sim 1$ for $\mathbf{p}$ and the other vectors for all $\boldsymbol{\xi}$. If $Al > 1$, the alignment between two vectors increases during rare events, as can be seen for when under high rotational power conditions P_{rot}, $\boldsymbol{\alpha}$ and $\boldsymbol{\Omega}$ become more aligned for both particle shapes. And if $Al < 1$, then the alignment between two vectors decreases during rare events and they become more perpendicular. This is observed for a triad and how its tumbling increases during rare events where $Al < 1$ for $\mathbf{p}$ and $\boldsymbol{\Omega}$ for all $\boldsymbol{\xi}$. We can visually demonstrate the decrease in alignment between $\mathbf{p}$ and $\boldsymbol{\Omega}$ with Fig. 4.9(a) where the PDF of $\mathbf{p} \cdot \boldsymbol{\Omega}/|\boldsymbol{\Omega}|$ is shown for when the triad experiences high rotational power gain and loss. We see an increase in the perpendicularity of the two vectors during such events, however, there is no significant difference between extreme power gain and loss events. Fig. 4.9(b) shows the same statistics for $\mathbf{p} \cdot \boldsymbol{\alpha}/|\boldsymbol{\alpha}|$ where the PDF is large around zero, demonstrating the preferential perpendicularity of $\boldsymbol{\alpha}$ with the triad symmetry axis. This alignment can also be observed in the larger contributions of $\left\langle \alpha_{p_\perp}^2 \right\rangle$ to the overall angular acceleration $\langle \alpha_i \alpha_i \rangle$ in Fig 4.3(d) and Table 4.1.

An interesting observation is the unique behavior of the angular acceleration $\boldsymbol{\alpha}$ in the dynamics of a triad, since $\mathbf{p} \cdot \boldsymbol{\alpha}$ is the only dot product in Table 4.2 that has Al values both greater and less than 1, depending on the correlation factor $\boldsymbol{\xi}$. From Fig. 4.8(c) we see that for a triad $\mathbf{p}$ and $\boldsymbol{\alpha}$ are strongly perpendicular and we expect that Al would reflect this behavior by having $Al < 1$ for correlations of $\mathbf{p} \cdot \boldsymbol{\alpha}$ with events $\boldsymbol{\xi}$. But for rare $\boldsymbol{\Omega}$, $\mathbf{a}$, and P_{tr} events $Al > 1$, showing that the alignment increase between $\mathbf{p}$ and $\boldsymbol{\alpha}$ during such events. While during intense $\boldsymbol{\alpha}$ and P_{rot} events, the behavior is as expected and $Al < 0$.

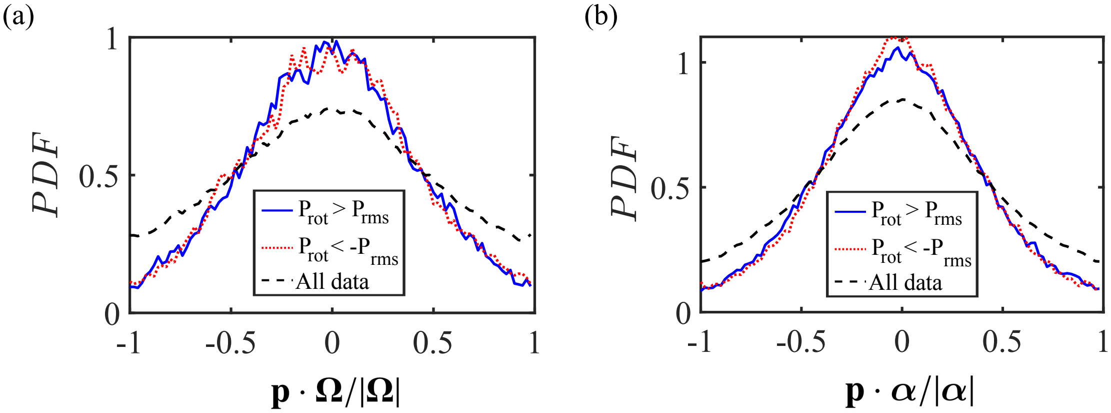

Figure 4.9: Cosine of the angle between (a) $\mathbf{p}$ and $\boldsymbol{\Omega}$ and (b) $\mathbf{p}$ and $\boldsymbol{\alpha}$ for a triad. The cosine is calculated for all the data (dashed line) showing the preferential perpendicularity of the two vectors. Also shown is the cosine for when a triad experiences high rotational power gain and loss, for when $P_{rot} > P_{rms}$ (blue solid line) and $P_{rot} < -P_{rms}$ (red dotted line), where we see an increase in the perpendicularity of the two vectors under these conditions.

Triad

ξ $\psi \cdot \varphi$	$\mathbf{\Omega}$	$\mathbf{a}$	$\boldsymbol{\alpha}$	P_{tr}	P_{rot}
$\mathbf{p} \cdot \mathbf{\Omega}$	0.831 ± 0.005	0.951 ± 0.008	0.969 ± 0.005	0.934 ± 0.021	0.713 ± 0.018
$\mathbf{p} \cdot \mathbf{a}$	1.081 ± 0.003	1.038 ± 0.005	1.070 ± 0.004	0.973 ± 0.014	1.077 ± 0.009
$\mathbf{p} \cdot \boldsymbol{\alpha}$	1.028 ± 0.005	1.130 ± 0.015	0.761 ± 0.004	1.205 ± 0.029	0.780 ± 0.014
$\mathbf{a} \cdot \mathbf{\Omega}$	0.891 ± 0.004	0.885 ± 0.006	0.978 ± 0.002	0.925 ± 0.011	0.872 ± 0.016
$\boldsymbol{\alpha} \cdot \mathbf{\Omega}$	1.017 ± 0.003	1.049 ± 0.005	1.046 ± 0.004	1.028 ± 0.016	1.792 ± 0.011
$\mathbf{a} \cdot \boldsymbol{\alpha}$	0.976 ± 0.003	0.880 ± 0.008	0.917 ± 0.002	0.942 ± 0.036	0.826 ± 0.014

Tetrad

ξ $\psi \cdot \varphi$	$\mathbf{\Omega}$	$\mathbf{a}$	$\boldsymbol{\alpha}$	P_{tr}	P_{rot}
$\mathbf{p} \cdot \mathbf{\Omega}$	0.996 ± 0.008	0.994 ± 0.008	0.994 ± 0.006	0.994 ± 0.020	1.000 ± 0.029
$\mathbf{p} \cdot \mathbf{a}$	1.003 ± 0.006	0.989 ± 0.014	0.989 ± 0.004	1.009 ± 0.030	0.976 ± 0.026
$\mathbf{p} \cdot \boldsymbol{\alpha}$	0.989 ± 0.002	0.997 ± 0.007	1.011 ± 0.003	0.994 ± 0.014	1.002 ± 0.016
$\mathbf{a} \cdot \mathbf{\Omega}$	0.907 ± 0.005	0.897 ± 0.008	0.985 ± 0.006	0.927 ± 0.023	0.866 ± 0.027
$\boldsymbol{\alpha} \cdot \mathbf{\Omega}$	0.990 ± 0.004	1.038 ± 0.013	1.037 ± 0.006	1.020 ± 0.026	1.824 ± 0.019
$\mathbf{a} \cdot \boldsymbol{\alpha}$	1.004 ± 0.003	0.882 ± 0.009	0.934 ± 0.002	0.919 ± 0.016	0.856 ± 0.032

Table 4.3: The alignment of the various quantities involved in the dynamics of triads and tetrads defined by the dot product $\psi \cdot \varphi$ and its correlation to the variable ξ. P_{tr} is the translational power and P_{rot} is the rotational power.

We further investigate particle alignments by examining the cosine of the angle between **a** and **Ω** for both particles as shown in Fig. 4.10. The two vectors **a** and **Ω** are mostly perpendicular to each-other as is shown by the cosine of the angle between them being 0 for all the data. The triad shows stronger signs of perpendicularity with the PDF being sharper around 0. We also condition this dot product for strong P_{rot} gain and loss to see how extreme rotation events influence the particle dynamics. The perpendicularity of the two vectors increases during extreme rotation and vorticity events, showing that in such instances the rotating particle experiences centrifugal accelerations that are perpendicular to **Ω**. The observation that particles experience centrifugal acceleration due to fluid vorticity can also be seen by looking at the tumbling motion of a triad where Fig. 4.8(b) shows the preferentially parallel behavior between **p** and **a** which indicates that a triad that predominantly tumbles in turbulent flow also experiences centrifugal accelerations perpendicular to its plane of symmetry.

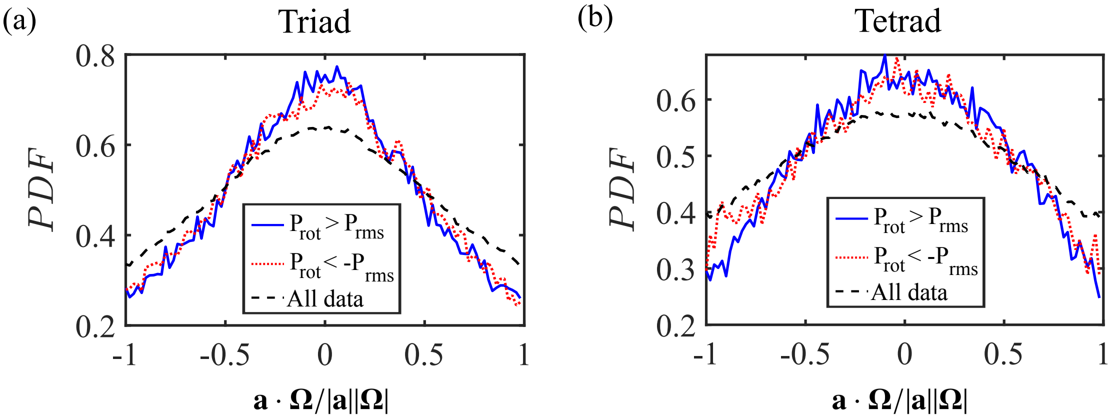

Figure 4.10: Cosine of the angle between **a** and **Ω** for (a) triads and (b) tetrads. The two vectors are preferentially perpendicular with the triads showing stronger signs of perpendicularity in its dynamics. The cosine is also shown for when the particles experience high rotational power gain and loss, for when $P_{rot} > P_{rms}$ (blue solid line) and $P_{rot} < -P_{rms}$ (red dotted line).

4.3.3 Translational and rotational power

Extreme translational and rotational power events influence particle alignments where there appears to be no significant difference between gain and loss events, as shown in Figs. 4.9, 4.10. Fig. 4.11 shows the PDFs of the translational, $P_{tr} = \mathbf{u} \cdot \mathbf{a}$, and rotational power, $P_{rot} = \mathbf{\Omega} \cdot \boldsymbol{\alpha}$, for triads and tetrads, where the PDFs for tetrads have been multiplied by 100 to distinguish between the two particles. The translational power is normalized by $D\tau_D^{-2}u_{rms}$, where $D\tau_D^{-2}$ is the normalization factor for the particle translational acceleration, at the scale of the particle, and u_{rms} is the tracer rms velocity used to normalize the particle translational velocity. The rotational power is normalized by τ_D^{-3}. From Fig. 4.11 we see that triads experience larger translational and rotational powers as compared to tetrads. Additionally, we do not observe any significant signs of imbalance from the PDFs, and both power gain ($P > 0$) and power loss ($P < 0$) events are equally likely to occur for the large particles.

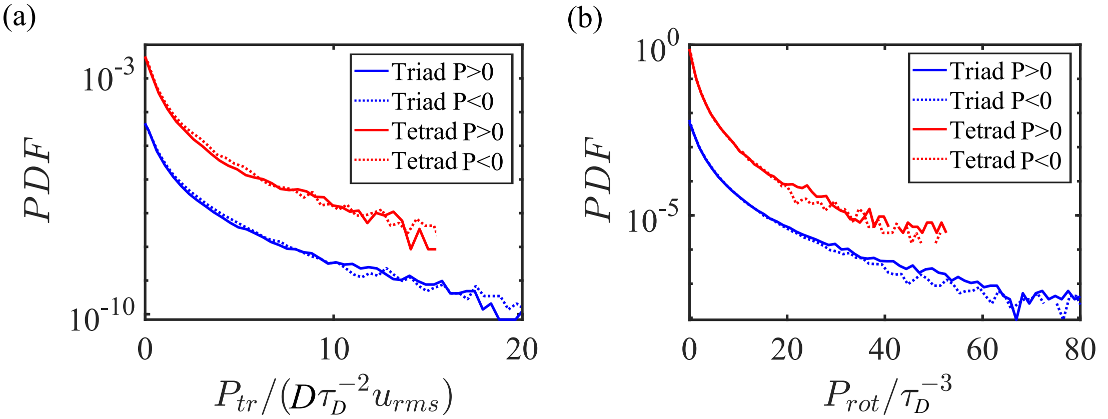

Figure 4.11: PDFs of the normalized (a) translational and (b) rotational power in the turbulent flow of the water tunnel at Reynolds number $Re_\lambda = 310$ for both triads and tetrads. The solid lines show positive power and dotted lines show negative power reflected around the vertical axis for visualization. The PDFs for tetrads have been multiplied by 100 to distinguish between the two particles.

We also examine the PDF of translational power gain and loss of the flow using tracer particles. Fig. 4.12 shows the power gain and loss for tracers in the flow of the vertical water tunnel where we observe similar results to Xu et al. (2014) where events with large power loss are more likely to occur, showing the irreversibility of turbulent systems. Xu et al. (2014) define an irreversibility value as the third moment of the dimensionless power, where the normalization is the energy dissipation rate of the flow. We measure this value to be 2×10^5 in our flow which is approximately an order magnitude higher than the expected value at $Re_\lambda = 310$ given by Xu et al. (2014) . This suggests that the irreversibility value is dependent on initial and boundary conditions of the flow. Additionally, we would need to perform experiments at different Reynolds numbers to obtain the Re_λ^2 scaling factor of the irreversibility value reported by Xu et al. (2014).

Here, we define a different normalization factor for the third moment of the translational power since the translational velocity and acceleration are different scale quantities. We define Ir as

$$Ir = -\left\langle P^3 \right\rangle / \left(\varepsilon^{3/4} \nu^{-1/4} U_{rms}\right)^3 \tag{4.3}$$

where $\varepsilon^{3/4}\nu^{-1/4}$ is the normalization factor for the translational acceleration, which is a small scale quantity, and U_{rms} is the normalization for the translational velocity. In our flow we measure this irreversibility value to be $IR = 100$, clearly showing the irreversibility of turbulent flows.

4.4 Conclusions

Here we have demonstrated advances in experimental measurements of particle translational and angular velocities and accelerations. Using these measurements of the quantities involved in particle dynamics we can gain insight about their alignment with

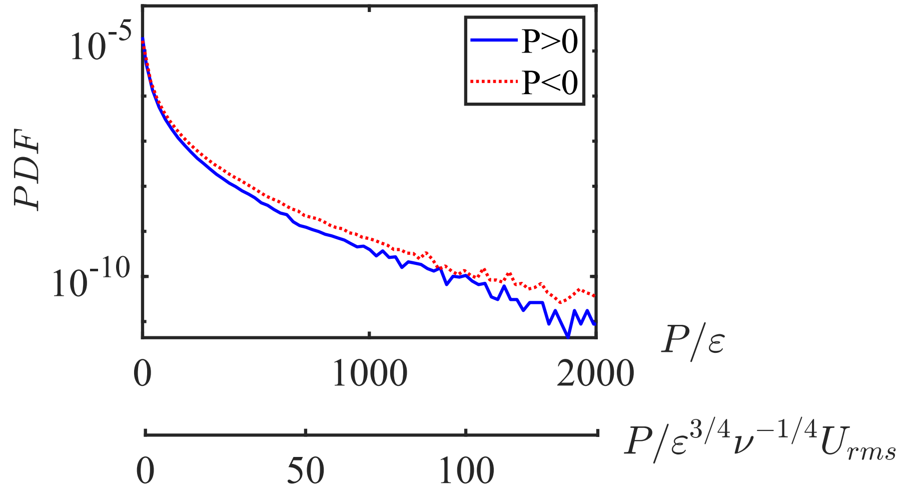

Figure 4.12: PDF of the normalized translational power in the turbulent flow of the water tunnel at Reynolds number $Re_\lambda = 310$, using two different normalization factors. The solid blue line shows positive power and the dotted red line is negative power reflected around the vertical axis for visualization. The fluid elements are more likely to experience extreme power loss events than power gain, indicating the irreversibility that exists in turbulent flows.

one-another and how particle dynamics are affected by the flow. We show our ability in precisely measuring particle solid-body rotation rates and its components, the tumbling and spinning rates. The two particle shapes we study are disk-like triads and spherical tetrads that have the same particle diameter of 100η. Large particles exhibit unusual behavior from what is expected from tracer spheroids in turbulence. We see that the rotation rate of large particles is shape dependent, in contrast to tracer spheroids in turbulence that have almost equal solid-body rotation rates for particles with different aspect ratio. We are also able to measure the particle translational and angular accelerations, these quantities are difficult to measure experimentally and extrapolations are necessary to obtain precise measurements. The triad angular accelerations show strong signs of particle alignment with turbulent structures on the scale of the particle diameter. Our experiments have shown that large particles in turbulence have shape dependent dynamics that are not captured by tracer particle results and a new approach is required where the particle angular accelerations are also considered in order to develop a complete picture of particle dynamics in turbulence.

The translational and rotational power of triads and tetrads are also examined to study the irreversibility of turbulent flows. The PDFs of power gain and loss do not show significant signs of asymmetry and the power gain ($P > 0$) and power loss ($P < 0$) events are both equally likely. However, the PDF of translational power for the flow show signs of irreversibility in turbulence in that the likelihood of extreme power loss events are higher than power gain. The irreversibility factor defined as the dimensionless third moment of the power for fluid particles further show that turbulence is irreversible as observed by Xu et al. (2014).

Future work would need to explore the size dependence of the solid-body rotation rate and examine at what ratio of particle diameter to fluid scales the transition from the expected tracer behavior occurs. The study of turbulent structure and large particle dynamics alongside each-other is extremely useful in the attempt to precisely answer the question of whether large particles are aligned and influenced by fluid structures on the same scale as the particle. Further work also needs to be done on the translational and rotational power calculations to see if the power-law scaling observed by Xu et al. (2014) is also observed for complex shaped particles and their rotational power. We would also need to explore whether Ir scales as Re_{λ}^{2} in different flow environments by doing experiments at different Reynolds numbers.

Chapter 5

Appendix

5.1 Data documentation

The work in this thesis has been archived on our group NAS system with parts of the data and codes used for analysis also available on our group Google Drive.

Work located on NAS2 (data) can be found under the *bhejazi* folder and contains the following:
1. MATLAB codes used for data analysis
2. Analyzed data from experiments on deformable particles in Taylor-Couette flow and the vertical water tunnel, and the angular dynamics of large particle in the vertical water tunnel
3. MATLAB .fig files of the figures in the dissertation

The MATLAB codes and figures are also available on the group Google Drive. The group Google Drive also contains the history of composed papers.

The raw video files and camera calibration images can be found on the two Servers. The first 90 runs of the September 26 data-set of large particle angular dynamics have been analyzed and stored in the analyzed data section of the archive.

5.2 Server system documentation

The servers are connected to a UPS system. In the case of power failure the UPS will safely shut down the Servers so that hard-drives are not damaged. The UPS went online on 01/10/2020 and will need battery replacement every 3 years, which means that the next battery change will need to occur on 01/10/2023.

All login and related information for the servers, UPS, and 10Gb Switch can be found in a physical folder and lab notebook located in the server rack on top of the UPS.

5.3 Data analysis

The data analysis codes for finding particle orientations and deformations can be found in *Codes→codes_tracking→orientation_finding*.

To find particle deformations we first find particle centers using the clustering codes which can then be used by the C code to obtain individual particle tracks. The tracked particles can now be used to find the equilibrium configuration of the deformable particles using the *find_eq* scripts. Once the equilibrium configuration is obtained we are ready to measure particle deformations using the *find_orientation_deformable* codes. All related functions called by these codes are also located in this folder.

Similarly we find the orientations and positions of rigid particles after obtaining particle tracks by using the *bh_find_orientation_stiffparticle* codes.

After obtaining particle positions and orientations we can use the codes in the *rotation-rate* and *velocity* folders to measure particle velocities and accelerations.

Bibliography

S. Alben, M. Shelley, and J. Zhang. Drag reduction through self-similar bending of a flexible body. *Nature*, 420(6915):479–481, 2002.

A. Ali, E. L. C. Plan, S. S. Ray, and D. Vincenzi. Semiflexible particles in isotropic turbulence. *Physical Review Fluids*, 1:082402, Dec 2016.

S. Allende, C. Henry, and J. Bec. Stretching and buckling of small elastic fibers in turbulence. *Physical Review Letters*, 121:154501, Oct 2018.

H. Aref. Stirring by chaotic advection. *Journal of Fluid Mechanics*, 143:1–21, June 1984.

H. Aref, J. R. Blake, M. Budišić, S. S. S. Cardoso, J. H. E. Cartwright, H. J. H. Clercx, K. El Omari, R. Feudel, U.and Golestanian, E. Gouillart, G. F. van Heijst, T. S. Krasnopolskaya, Y. Le Guer, R. S. MacKay, V. V. Meleshko, G. Metcalfe, I. Mezić, A. P. S. de Moura, O. Piro, M. F. M. Speetjens, R. Sturman, J. Thiffeault, and I. Tuval. Frontiers of chaotic advection. *Review of Modern Physics*, 89:025007, Jun 2017.

G. K. Batchelor. Slender-body theory for particles of arbitrary cross-section in stokes flow. *Journal of Fluid Mechanics*, 44(3):419–440, 1970.

Leif E. Becker and Michael J. Shelley. Instability of elastic filaments in shear flow yields first-normal-stress differences. *Physical Review Letters*, 87:198301, Oct 2001.

V. Bezuglyy, B. Mehlig, and M. Wilkinson. Poincare indices of rheoscopic visualizations. *EPL*, 89(3):34003, 2010.

A. D. Bordoloi and E. Variano. Rotational kinematics of large cylindrical particles in turbulence. *Journal of Fluid Mechanics*, 815:199:222, 2017.

S. Bounoua, G. Bouchet, and G. Verhille. Tumbling of inertial fibers in turbulence. *Physical Review Letters*, 121:124502, Sep 2018.

F. P. Bretherton. The motion of rigid particles in a shear flow at low reynolds number. *Journal of Fluid Mechanics*, 14(2):284–304, 1962.

C. Brouzet, G. Verhille, and P. Le Gal. Flexible fiber in a turbulent flow: A macroscopic polymer. *Physical Review Letters*, 112:074501, Feb 2014.

M. Byron, J. Einarsson, K. Gustavsson, G. Voth, B. Mehlig, and E. Variano. Shape-dependence of particle rotation in isotropic turbulence. *Physics of Fluids*, 27(3): 035101, 2015.

B. Chakrabarti, Y. Liu, J. LaGrone, R. Cortez, L. Fauci, O. du Roure, D. Saintillan, and A. Lindner. Flexible filaments buckle into helicoidal shapes in strong compressional flows. *Nature Physics*, 16(6):689–694, 2020.

B. C. Cole, G. G. Marcus, S. Parsa, S. Kramel, R. Ni, and G. A. Voth. Methods for measuring the orientation and rotation rate of 3d-printed particles in turbulence. *JoVE*, 112:e53599, 2016.

M. C. Cross and Hohenberg, P. C. Pattern formation outside of equilibrium. *Review of Modern Physics*, 65(3):851–1112, 1993.

P. G. de Gennes and J. Prost. *The physics of liquid crystals*. Oxford University Press, 1995.

M. R. Dennis. Polarization singularity anisotropy: determining monstardom. *Optics Letters*, 33(22):2572, November 2008.

M. H. DiBenedetto, N. T. Ouellette, and J. R. Koseff. Transport of anisotropic particles under waves. *Journal of Fluid Mechanics*, 837, 2018.

C. D. Dimitropoulos, Y. Dubief, E. S. G. Shaqfeh, P. Moin, and S. K. Lele. Direct numerical simulation of polymer-induced drag reduction in turbulent boundary layer flow. *Physics of Fluids*, 17(1):011705, 2005.

D. Dotto and C. Marchioli. Orientation, distribution, and deformation of inertial flexible fibers in turbulent channel flow. *Acta Mechanica*, 230(2):597–621, Feb 2019.

I. T. Drummond and W. Münch. Distortion of line and surface elements in model turbulent flows. *Journal of Fluid Mechanics*, 225:529–543, 1991.

O. du Roure, A. Lindner, E. N. Nazockdast, and M. J. Shelley. Dynamics of flexible fibers in viscous flows and fluids. *Annual Review of Fluid Mechanics*, 51(1):539–572, 2019.

G. Duclos, C. Erlenkämper, J. Joanny, and P. Silberzan. Topological defects in confined populations of spindle-shaped cells. *Nature Physics*, 13(1):58–62, 2017.

D. A Egolf, I. V. Melnikov, and E. Bodenschatz. Importance of Local Pattern Properties in Spiral Defect Chaos. *Physical Review Letters*, 80(15):3228–3231, April 1998.

H. M. Ezzeldin, M. D. de Tullio, M. Vanella, S. D. Solares, and E. Balaras. A strain-based model for mechanical hemolysis based on a coarse-grained red blood cell model. *Annals of Biomedical Engineering*, 43(6):1398–1409, Jun 2015.

F. Flossmann, K. O'Holleran, M. R Dennis, and M. J Padgett. Polarization Singularities in D-2 and D-3 Speckle Fields. *Physical Review Letters*, 100(20):203902, 2008.

A. Gay, B. Favier, and G. Verhille. Characterisation of flexible fibre deformations in turbulence. *EPL (Europhysics Letters)*, 123(2):24001, 2018.

L. Giomi. Geometry and Topology of Turbulence in Active Nematics. *Physical Review X*, 5:031003, July 2015.

M. Giona, A. Adrover, F. J. Muzzio, S. Cerbelli, and M. M. Alvarez. The geometry of mixing in time-periodic chaotic flows. i. asymptotic directionality in physically realizable flows and global invariant properties. *Physica D: Nonlinear Phenomena*, 132(3):298 – 324, 1999.

J. Gray and G. J. Hancock. The propulsion of sea-urchin spermatozoa. *Journal of Experimental Biology*, 32(4):802–814, 1955.

M. A. Green, C. W. Rowley, and G. Haller. Detection of Lagrangian coherent structures in three-dimensional turbulence. *Journal of Fluid Mechanics*, 572:111–120, 2007.

E. Guazzelli and J. Hinch. Fluctuations and Instability in Sedimentation. *Annual Review of Fluid Mechanics*, 43:97–116, 2011.

H. F. Guo, N. Y. K. Lam, C. Yang, and L. Li. Simulating three-dimensional dynamics of flexible fibers in a ring spinning triangle: chitosan and cotton fibers. *Textile Research Journal*, 87(11):1403–1410, 2017.

K. Gustavsson, J. Einarsson, and B. Mehlig. Tumbling of small axisymmetric particles in random and turbulent flows. *Physical Review Letters*, 112:014501, Jan 2014.

G. Haller. Lagrangian Coherent Structures. *Annual Review of Fluid Mechanics*, 47(1): 137–162, 2015.

J.B Harris and J.F.T Pittman. Equivalent ellipsoidal axis ratios of slender rod-like particles. *Journal of Colloid and Interface Science*, 50(2):280 – 282, 1975.

B. Hejazi, B. Mehlig, and G. A. Voth. Emergent scar lines in chaotic advection of passive directors. *Phys. Rev. Fluids*, 2:124501, Dec 2017. doi: 10.1103/PhysRevFluids.2.124501. URL `https://link.aps.org/doi/10.1103/PhysRevFluids.2.124501`.

B. Hejazi, M.l Krellenstein, and G. A. Voth. Using deformable particles for single-particle measurements of velocity gradient tensors. *Experiments in Fluids*, 60(10):153, 2019. doi: 10.1007/s00348-019-2796-0. URL `https://doi.org/10.1007/s00348-019-2796-0`.

B. Herzhaft, E. Guazzelli, M. B Mackaplow, and E. S G Shaqfeh. Experimental Investigation of the Sedimentation of a Dilute Fiber Suspension. *Physical Review Letters*, 77(2):290–293, July 1996.

G. B. Jeffery. The Motion of Ellipsoidal Particles Immersed in a Viscous Fluid. *Proc. R. Soc. Lond. A*, 102(715):161–179, November 1922.

D. Karrasch, F. Huhn, and G. Haller. Automated detection of coherent Lagrangian vortices in two-dimensional unsteady flows. *Proc. R. Soc. Lond. A*, 471(2173):20140639–20140639, November 2014.

K. Kawaguchi, R. Kageyama, and M. Sano. Topological defects control collective dynamics in neural progenitor cell cultures. *Nature*, 545(7654):327–331, 2017.

F. C. Keber, E. Loiseau, T. Sanchez, S. J. DeCamp, L. Giomi, M. J. Bowick, M. C. Marchetti, Z. Dogic, and A. R. Bausch. Topology and dynamics of active nematic vesicles. *Science*, 345(6201):1135–1139, 2014.

D. L. Koch and E. S. G. Shaqfeh. The instability of a dispersion of sedimenting spheroids. *Journal of Fluid Mechanics*, 209:521–542, December 1989.

S. Kramel. *Non-Spherical Particle Dynamics in Turbulence*. PhD thesis, Wesleyan University, May 2018.

A. La Porta, G. A. Voth, A. M. Crawford, J. Alexander, and E. Bodenschatz. Fluid particle accelerations in fully developed turbulence. *Nature*, 409(6823):1017–1019, 2001.

Y. Li, E. Perlman, M. Wan, Y. Yang, C. Meneveau, R. Burns, S. Chen, A. Szalay, and G. Eyink. A public turbulence database cluster and applications to study lagrangian evolution of velocity increments in turbulence. *Journal of Turbulence*, 9:N31, 2008.

A. J. Lichtenberg and M. A. Lieberman. *Regular and Chaotic Dynamics*, volume 38 of *Applied Mathematical Sciences*. Springer-Verlag New York, 2 edition, 1992.

M. Liu and F. J. Muzzio. The curvature of material lines in chaotic cavity flows. *Physics of Fluids*, 8(1):75–83, 1996.

F. Lundell, L. D. Söderberg, and P. H. Alfredsson. Fluid mechanics of papermaking. *Annual Review of Fluid Mechanics*, 43(1):195–217, 2011.

Beat Lüthi, Arkady Tsinober, and Wolfgang Kinzelbach. Lagrangian measurement of vorticity dynamics in turbulent flow. *Journal of Fluid Mechanics*, 528:87–118, 2005.

L. E. Malvern. *Introduction to Continuum Mechanics*. Prentice Hall Inc., 1969.

C. Marchioli and A. Soldati. Rotation statistics of fibers in wall shear turbulence. *Acta Mechanica*, 224(10):2311–2329, 2013.

C. Marchioli and S. Vincent. Special issue on finite-size particles, drops and bubbles in fluid flows: advances in modelling and simulations. *Acta Mechanica*, 230(2): 381–386, Feb 2019.

G. G Marcus, S. Parsa, S. Kramel, R. Ni, and G. A Voth. Measurements of the solid-body rotation of anisotropic particles in 3d turbulence. *New Journal of Physics*, 16 (10):102001, oct 2014.

V. Mathai, M. W. M. Neut, E. P. van der Poel, and C. Sun. Translational and rotational dynamics of a large buoyant sphere in turbulence. *Experiments in Fluids*, 57(4):51, 2016.

M. Mathur, G. Haller, T. Peacock, J. E. Ruppert-Felsot, and H. L. Swinney. Uncovering the Lagrangian Skeleton of Turbulence. *Physical Review Letters*, 98(14):144502, April 2007.

A. S. Monin and A. M. Yaglom. *Statistical Fluid Mechanics: Mechanics of Turbulence*. Dover New York, 1975.

R. Ni, N. T Ouellette, and G. A Voth. Alignment of vorticity and rods with Lagrangian fluid stretching in turbulence. *Jornal of Fluid Mechanics*, 743:R3–12, March 2014.

J. A. Olson and R. J. Kerekes. The motion of fibres in turbulent flow. *Journal of Fluid Mechanics*, 377:47–64, December 1998.

E. Ott. *Chaos in Dynamical Systems*. Cambridge University Press, 2 edition, 2002.

J. M. Ottino. Mixing, Chaotic Advection, and Turbulence. *Annual Review of Fluid Mechanics*, 22:207–253, 1990.

S. Parsa and G. A. Voth. Inertial range scaling in rotations of long rods in turbulence. *Physical Review Letters*, 112:024501, Jan 2014.

S. Parsa, J. S. Guasto, M. Kishore, N. T. Ouellette, J. P. Gollub, and G. A. Voth. Rotation and alignment of rods in two-dimensional chaotic flow. *Physics of Fluids*, 23(4): 043302, 2011.

S. Parsa, E. Calzavarini, F. Toschi, and G. A. Voth. Rotation Rate of Rods in Turbulent Fluid Flow. *Physical Review Letters*, 109:134501, September 2012.

J. S. Paschkewitz, Y. Dubief, and E. S. G. Shaqfeh. The dynamic mechanism for turbulent drag reduction using rigid fibers based on Lagrangian conditional statistics. *Physics of Fluids*, 17(6):063102, 2005.

R. T. Pierrehumbert. Tracer microstructure in the large-eddy dominated regime. *Chaos, Solitons & Fractals*, 4(6):1091–1110, 1994.

M. B. Pinsky and A. P. Khain. Some effects of cloud turbulence on water–ice and ice–ice collisions. *Atmospheric Research*, 47:69–86, 1998.

S. B. Pope. The evolution of surfaces in turbulence. *International Journal of Engineering Science*, 26:445–469, 1988.

S. B. Pope. *Turbulent Flows*. Cambridge University Press, 2000.

S. B. Pope, P. K. Yeung, and S. S. Girimaji. The curvature of material surfaces in isotropic turbulence. *Physics of Fluids A: Fluid Dynamics*, 1(12):2010–2018, 1989.

T. R. Powers. Dynamics of filaments and membranes in a viscous fluid. *Review of Modern Physics*, 82:1607–1631, May 2010.

N. Pujara, T. B. Oehmke, A. D. Bordoloi, and E. A. Variano. Rotations of large inertial cubes, cuboids, cones, and cylinders in turbulence. *Physical Review Fluids*, 3: 054605, May 2018.

H. J. Qi, K. Joyce, and M. C. Boyce. Durometer hardness and the stress-strain behavior of elastomeric materials. *Rubber Chemistry and Technology*, 76(2):419–435, 2003.

B. Qian, T. R. Powers, and K. S. Breuer. Shape transition and propulsive force of an elastic rod rotating in a viscous fluid. *Physical Review Letters*, 100:078101, Feb 2008.

M. E. Rosti, A. A. Banaei, L. Brandt, and A. Mazzino. Flexible fiber reveals the two-point statistical properties of turbulence. *Physical Review Letters*, 121:044501, Jul 2018.

M. E. Rosti, F. De Vita, and L. Brandt. Numerical simulations of emulsions in shear flows. *Acta Mechanica*, 230(2):667–682, Feb 2019.

D. Rothstein, E. Henry, and J. P. Gollub. Persistent patterns in transient chaotic fluid mixing. *Nature*, 401(6755):770–772, October 1999.

A. Roy, R. J. Hamati, T. Lydia, D. L. Koch, and G. A. Voth. Inertial torques and a symmetry breaking orientational transition in the sedimentation of slender fibers. *Journal of Fluid Mechanics*, 2019.

C. P. R. Saunders. Thunderstorm electrification laboratory experiments and charging mechanisms. *Journal of Geophysical Research: Atmospheres*, 99(D5):10773–10779, 1994.

C. P. R. Saunders, S. L. Peck, G. G. A. Varela, E. E. Avila, and N. E. Castellano. A laboratory study of the influence of water vapour and mixing on the charge transfer process during collisions between ice crystals and graupel. *Atmospheric Research*, 58(3):187–203, 2001.

T. B. Saw, A. Doostmohammadi, V. Nier, L. Kocgozlu, S. Thampi, Y. Toyama, P. Marcq, C. T. Lim, J. M Yeomans, and B. Ladoux. Topological defects in epithelia govern cell death and extrusion. *Nature*, 544(7649):212–216, 2017.

J. B. Segur and Helen E. Oberstar. Viscosity of glycerol and its aqueous solutions. *Industrial & Engineering Chemistry*, 43(9):2117–2120, 1951.

M. Serra and G. Haller. Efficient computation of null geodesics with applications to coherent vortex detection. *Proc. R. Soc. Lond. A*, 473(2199):20160807–18, March 2017.

Steven C Sherwood, Vaughan T J Phillips, and J S Wettlaufer. Small ice crystals and the climatology of lightning. *Geophysical Research Letters*, 33(5):L05804, 2006.

M. Shin and D. L. Koch. Rotational and translational dispersion of fibres in isotropic turbulent flows. *Journal of Fluid Mechanics*, 540:143–173, 2005.

John M. Stockie and Sheldon I. Green. Simulating the motion of flexible pulp fibres using the immersed boundary method. *Journal of Computational Physics*, 147(1): 147 – 165, 1998.

Supplemental. See supplemental material at the link below for animations of passive scalars, advected directors, and stretching eigenvectors in the flow of the standard map. Link to PhysRevFluids.

A. J. Szeri. Pattern-Formation in recirculating-flows of suspensions of orientable particles. *Phil. Trans Royal Soc. London Series*, 345(1677):477–506, December 1993.

A. J. Szeri and L. G. Leal. Microstructure suspended in 3-Dimensional flows. *Journal of Fluid Mechanics*, 250:143–167, 1993.

A. J. Szeri and L. G. Leal. Orientation Dynamics and Stretching of Particles in Unsteady, Three-dimensional Fluid Flows. *Chaos, Solitons & Fractals*, 4(6):913–927, 1994.

A. J. Szeri, S. Wiggins, and L. G. Leal. On the dynamics of suspended microstructure in unsteady, spatially inhomogeneous, two-dimensional fluid flows. *Journal of Fluid Mechanics*, 228:207–241, July 1991.

A. J. Szeri, W. J. Milliken, and L. G. Leal. Rigid particles suspended in time-dependent flows: irregular versus regular motion, disorder versus order. *Journal of Fluid Mechanics*, 237:33–56, 1992.

J. Thiffeault. Stretching and curvature of material lines in chaotic flows. *Physica D: Nonlinear Phenomena*, 198(3):169 – 181, 2004.

M. J. Twardos, P. E. Arratia, M. K. Rivera, G. A. Voth, J. P. Gollub, and R. E. Ecke. Stretching fields and mixing near the transition to nonperiodic two-dimensional flow. *Physical Review E*, 77(5):056315, May 2008.

A. Volk and C. J. Kähler. Density model for aqueous glycerol solutions. *Experiments in Fluids*, 59(5):75, Apr 2018. ISSN 1432-1114.

R. Volk, E. Calzavarini, E. Leveque, and J.F. Pinton. Dynamics of inertial particles in a turbulent von karman flow. *Journal of Fluid Mechanics*, 668:223–235, 2011.

G. A. Voth and A. Soldati. Anisotropic Particles in Turbulence. *Annual Review of Fluid Mechanics*, 49:249–276, 2017.

G. A Voth, G. Haller, and J. P. Gollub. Experimental Measurements of Stretching Fields in Fluid Mixing. *Physical Review Letters*, 88:254501, June 2002a.

G. A. Voth, A. La Porta, A. M. Crawford, J. Alexander, and E. Bodenschatz. Measurement of particle accelerations in fully developed turbulence. *Journal of Fluid Mechanics*, 469:121–160, 2002b.

Z. Warhaft. Passive Scalars in Turbulent Flows. *Annual Review of Fluid Mechanics*, 32 (1):203–240, 2000.

M. Wilkinson, V. Bezuglyy, and B. Mehlig. Fingerprints of random flows? *Physics of Fluids*, 21:043304, 2009.

M. Wilkinson, V. Bezuglyy, and B. Mehlig. Emergent order in rheoscopic swirls. *Journal of Fluid Mechanics*, 667:158–187, November 2010.

H. Xu, A. Pumir, G. Falkovich, E. Bodenschatz, M. Shats, H. Xia, N. Francois, and G. Boffetta. Flight–crash events in turbulence. *Proceedings of the National Academy of Sciences*, 2014.

Y.-N. Young and M. J. Shelley. Stretch-coil transition and transport of fibers in cellular flows. *Physical Review Letters*, 99:058303, Aug 2007.

H. Yu, K. Kanov, E. Perlman, J. Graham, E. Frederix, R. Burns, A. Szalay, G. Eyink, and C. Meneveau. Studying lagrangian dynamics of turbulence using on-demand fluid particle tracking in a public turbulence database. *Journal of Turbulence*, 13: N12, 2012.

L. Zhao and H. I. Andersson. Why spheroids orient preferentially in near-wall turbulence. *Journal of Fluid Mechanics*, 807:221–234, November 2016.

Lihao Zhao, Niranjan Reddy Challabotla, Helge I. Andersson, and Evan A. Variano. Rotation of nonspherical particles in turbulent channel flow. *Physical Review Letters*, 115:244501, Dec 2015.

R. Zimmermann, Y. Gasteuil, M. Bourgoin, R. Volk, A. Pumir, and J. Pinton. Rotational intermittency and turbulence induced lift experienced by large particles in a turbulent flow. *Physical Review Letters*, 106:154501, Apr 2011a.

R. Zimmermann, Y. Gasteuil, M. Bourgoin, R. Volk, A. Pumir, and J. Pinton. Tracking the dynamics of translation and absolute orientation of a sphere in a turbulent flow. *Review of Scientific Instruments*, 82(3):033906, 2011b.